Investigating the low energy enhancement of ^{44}Sc, ^{50,51}V and ^{64}Zn with large-scale shell model calculations

Jon Kristian Dahl

Thesis submitted for the degree of
Master of Science
60 credits

Department of Physics
Faculty of Mathematics and Natural Sciences

UNIVERSITY OF OSLO

Autumn 2022

Investigating the low energy enhancement of ^{44}Sc, ^{50,51}V and ^{64}Zn with large-scale shell model calculations

Jon Kristian Dahl

Investigating the low energy enhancement of ^{44}Sc, ^{50,51}V and ^{64}Zn with large-scale shell model calculations

http://www.duo.uio.no/

Printed: Reprosentralen, University of Oslo

Abstract

In this thesis, the gamma strength functions (GSF) of ^{44}Sc, ^{50,51}V, and ^{64}Zn have been studied using numerical shell model calculations with the software KSHELL. The scandium and vanadium calculations were compared to existing experimental Oslo method data. This work has a focus on the different contributions of $E1$ and $M1$ transitions to the GSFs with a particular emphasis on the low energy enhancement (LEE) part of the GSFs. The applicability of the generalised Brink-Axel (gBA) hypothesis has been studied for all of the nuclei, supplemented by a statistical analysis of the reduced transition probabilities (B values) from the calculations. The shell model and KSHELL have been pushed to the limit of what is computationally feasible to produce as high quality calculations as possible.

In all cases, the shell model calculations of this work show that the LEE is caused by $M1$ transitions, not $E1$ transitions. The calculated GSFs fit well with the experimental data in the entire gamma energy range of $E_\gamma = [0, 10]$ MeV, and the inclusion of $E1$ transitions is generally necessary for a good fit. The GSFs of all nuclei seem to be approximately independent of angular momentum, supporting the validity of the gBA hypothesis for these calculations. The distribution of B values from different selections of excitation energies closely match the Porter-Thomas ($\chi^2_{\nu=1}$) distribution for all nuclei, while in some cases the B distributions from selections of angular momenta show systematic deviations from the Porter-Thomas distribution, particularly for the $E1$ transitions. Using a sufficient amount of levels (and hence B values) per j^π in the shell model calculations is important for the quality of the resulting GSFs, particularly at the highest gamma energies. A correspondence between where fluctuations in the GSF starts and where the accompanying level density stops rising exponentially is seen. The GSFs of ^{50,51}V and ^{64}Zn have to our knowledge for the first time been calculated with $E1$ and $M1$ transitions in the same framework.

Acknowledgements

First of all, a huge thanks to my supervisors Ann-Cecilie Larsen, Noritaka Shimizu, and Sunniva Siem! Ann-Cecilie, you found a way to combine my love for computers and interest in physics, and for that I am very thankful. We've had so many interesting discussions about shell model calculations, gamma strength functions, the Brink-Axel hypothesis, the Porter-Thomas distribution and much more! I really hope to continue working with you after my master's. Thanks for always being helpful and positive! Positiveness really is contagious!

Shimizu-san, without KSHELL the work in this thesis would not be possible. Thank you for creating the great software that KSHELL is and thank you for helping me understand technical aspects of KSHELL and the nuclear shell model. It was great to finally get to meet you in real life in Tsukuba after almost two years of biweekly Zoom meetings! I am excited to follow the future development of KSHELL and shell model calculations.

Sunniva, I want to thank you for making it possible for us to travel abroad to attend experiments and conferences. Of course, my entire master's has been during the COVID-19 pandemic which has greatly limited the social interactions and travels, but I luckily got to attend an experiment in Orsay in France and the CNS summer school in Japan (plus the trip to Tsukuba). The France and Japan trips have both been such good experiences. I've gotten to know my fellow nuclear students and researchers in ways which only happen outside of the safe comfort zones of everyday life. It is sad that the pandemic has limited these possibilities, but I am grateful for the opportunities you have given us!

I want to give a huge thanks to Marcin Krotkiewski at NRIS for giving me fantastic help in debugging and running huge calculations on Betzy! Your help has been invaluable! I also want to thank Jenny Amundsen at NRIS for giving quick and informative help with regards to CPU hours on Betzy. Thank you both!

To my fellow master's students, thanks for making our office a fun and engaging place to be! We all have good chemistry, be it in the office, a party, in France or Japan. I extend this thanks to the entire nuclear physics group at the university of Oslo. You are all a great bunch of people whom I am happy to call my friends.

Takk til Hilde som aldri blir overrasket (men blir veldig glad!) når jeg får en god karakter fordi det har hun alltid visst at jeg får til og takk til Ingeborg fordi hun er jenta mi.

Contents

Chapter 1

Introduction

You, me and almost everything we can see, touch and feel are made up of *atoms*. Atoms are tiny particles of matter which were initially thought to be indivisible, an idea which originates from the natural philosophy of *atomism* dating back to ancient Greece and India. The idea of the atom was initially a purely philosophical one, and it wasn't until the early 1800s that the English chemist John Dalton gave what we today call an atom its name. The name atom comes from the Greek word *atomos* which roughly translates to *indivisible*, and it was initially thought that the atoms were indeed indivisible fundamental building blocks of nature. The indivisibility of the atom was discarded after the discovery of the electron in 1897 by J. J. Thomson and the discovery of the atomic nucleus in 1909 with the famous gold foil experiment by Hans Geiger, Ernest Marsden, and Ernest Rutherford. The neutron was discovered by James Chadwick in 1932, and at this point it was known that the atom is built up by a nucleus of positively charged protons and neutral neutrons surrounded by a cloud of negatively charged electrons. The protons and neutrons (collectively *nucleons*) are held together by the nuclear force, while the electrons are attracted to the nucleus by the electromagnetic force.

Models for the atomic nucleus were quickly developed after the discovery of the neutron, and one such model is the highly successful *nuclear shell model* – developed by Maria Goeppert Mayer, Eugene Paul Wigner and J. Hans D. Jensen in 1949 – which borrows many concepts from the also highly successful electron shell model. The nuclear shell model uses the Pauli exclusion principle to describe the structure of the nucleus. Since protons (and neutrons) are fermions, two or more are not allowed by nature to occupy the same quantum state. When, for example, two protons and two neutrons combine to form ^{4}He[1] the nuclear force pulls the nucleons together, but the exclusion principle forces the two protons to occupy different quantum states (and the two neutrons separately). As more nucleons are added to the nucleus they occupy distinct quantum states and a pattern emerges. The pattern – which is based on quantum properties like angular momentum and parity – is exactly what we have named *shell structure* in the nuclear shell model.

[1] Pronounced *helium four* and alternatively written *helium-4*.

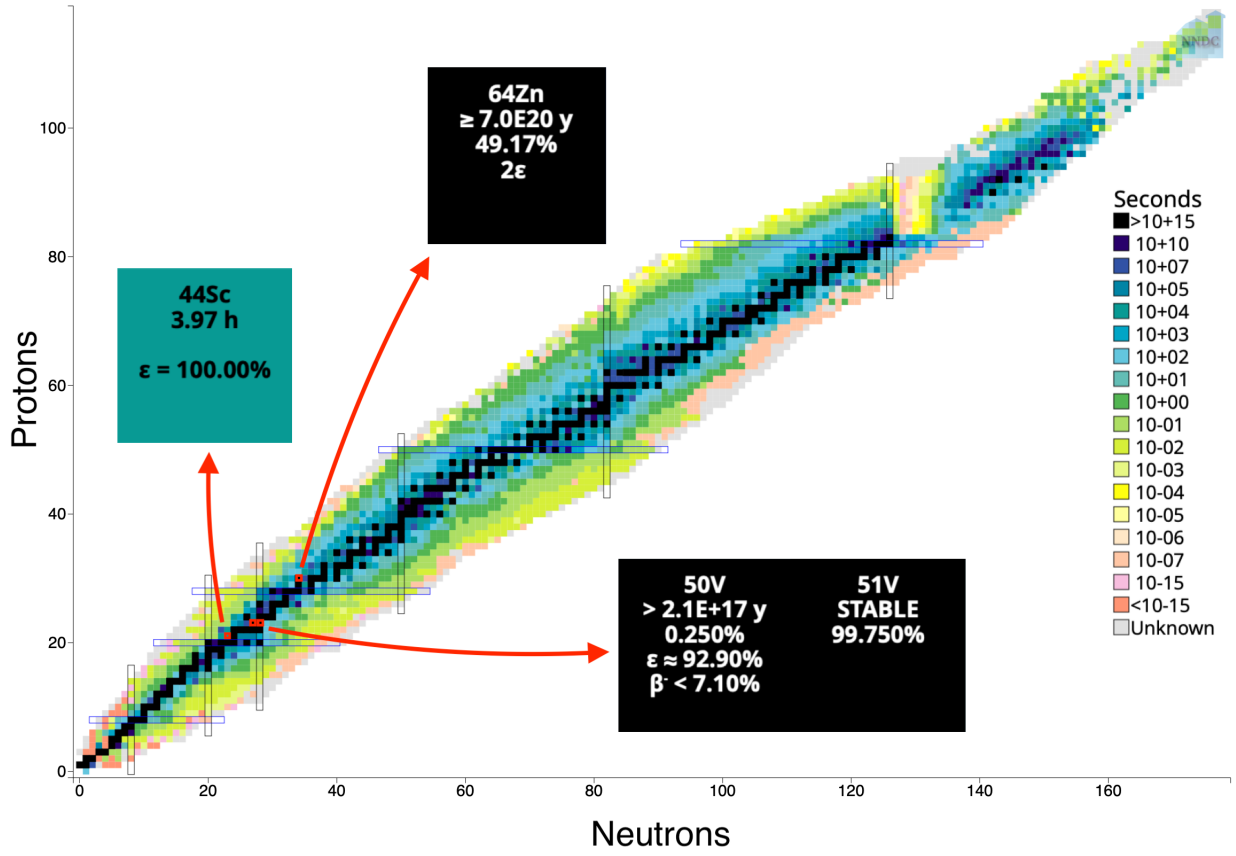

Figure 1.1: Chart of the nuclides. The nuclei used in this thesis are highlighted. Colours indicate half-lives. Figure from NuDat: nndc.bnl.gov/nudat3/.

Understanding the behaviour of the nucleus is important to a breadth of scientific fields, including medicine, astrophysics, material science, and nuclear energy. Today we have particle accelerators which let us create all sorts of nuclei, as well as letting us inject energy into nuclei placing them in *excited states*. A nucleus being in an excited state means that the nucleus contains an excess amount of energy which it wants to get rid of. Most nuclei usually gets rid of the excess energy by emitting electromagnetic radiation, a process which is called *gamma decay*. An excited nucleus might get rid of all the excess energy by a single large energy gamma decay or by several smaller energy gamma decays which sum up to the total excess energy. We study the preferred ways of gamma decay for an excited nucleus with the *gamma strength function* (GSF), a quantity which is essential to this thesis. Different nuclei have different preferred ways of gamma decay, and understanding the different preferences are of vital importance to the mentioned scientific fields. A particular feature of the GSF, called the low energy enhancement (LEE), reveals that some nuclei have an enhanced probability of decaying by low energy gamma decay. This thesis will have a particular focus on the LEE. The behaviour of an excited nucleus might affect how a nuclear reactor works,

what types of nuclei we can use for cancer treatment, and the reaction rates for stellar nucleosynthesis.

In all disciplines of science, it is of great importance to develop models which describe what we see experimentally, and nuclear physics is no exception. The nuclear shell model has proven to be very successful in predicting the energy, angular momentum and parity of excited nuclei, but there is a problem. The nucleus is a complicated many-particle system and the number of particles (nucleons) often makes calculations with the shell model computationally very heavy. Take ^{44}Sc as an example; it has 21 protons and 23 neutrons in its nucleus, and these 44 nucleons can occupy an enormous amount of different quantum states. Letting all of the nucleons do as they please is not computationally feasible for any computer in existence today so we must set some limitations. We approximate the nucleus by locking some of the nucleons in an *inert core* which is surrounded by a set of *valence nucleons* free to move about and interact with each other. By fixing the core and letting only a limited number of valence nucleons be excitable, we can drastically reduce the computational cost. We also limit the number of possible quantum states which the valence nucleons are allowed to occupy. The set of allowed quantum states is called the *model space* of the shell model calculations.

In this thesis I will perform shell model calculations with the nuclear shell model solver code KSHELL [1] to study the GSFs of the nuclei scandium-44, vanadium-50, vanadium-51, and zinc-64 with a particular focus on the LEE. The goal of this work is to numerically reproduce the LEE which has been seen experimentally in the scandium and vanadium isotopes [2, 3] to find out which parts of the GSF is causing the LEE. The goal of this work is also to push the limits of what is computationally possible to do with the shell model by calculating for ^{64}Zn which is one of the heaviest shell model calculations performed to this date, and also by using large model spaces for the other nuclei of this work. This is made possible by the supercomputer Betzy and the software KSHELL.

Setting limitations on shell model calculations is absolutely necessary for all calculations in this thesis even when using Betzy which is the most powerful supercomputer in Norway[2]. In fig. 1.1 we see the chart of the nuclides where the nuclei used in this thesis are highlighted. Even though these nuclei – ^{44}Sc, ^{50,51}V, and ^{64}Zn – have fewer nucleons than most of the other nuclei in the chart, they still have to be limited for any computer today to be able to compute them with the shell model. This thesis presents some of the largest shell model calculations ever performed to date, and in particular, presents calculations where the electric and magnetic dipole ($E1$ and $M1$) contributions to the GSF are calculated within the same framework which is important in the study of the LEE. As of today, there is no standard model in nuclear physics as there is in particle physics. Models of the nucleus must be developed and compared to empirical data to further develop our understanding of nuclear physics, and the work of this thesis will hopefully help to further this cause!

[2] documentation.sigma2.no/hpc_machines/betzy.html

In this thesis I start with presenting the theoretical concepts in chapter 2. I present theoretical concepts which are strictly necessary for understanding the results. Those concepts are the nuclear level density, the gamma strength function, the generalised Brink-Axel hypothesis, the low energy enhancement, and the nuclear shell model. The theory chapter also includes additional information which gives a greater depth to the theoretical understanding as a whole, though not strictly necessary for understanding the results. This includes quantum mechanical concepts like what quantum *spin* really is, why (quantum) total angular momentum, orbital angular momentum, and spin can be regarded as vector quantities even though they are represented by operators, why we use the magnitude of the angular momentum vector together with its z component, and what *parity* is. We will also visit electromagnetism to figure out what the *multipolarity* of electromagnetic radiation really means and how it relates to electromagnetic transition selection rules. In chapter 3 the software and hardware setup will be presented, including KSHELL, kshell-utilities, and Betzy. The results will be presented and discussed in chapter 4, and the thesis will be concluded in chapter 5 with conclusions and future outlook. All code used to produce the figures of this work is available at www.github.com/GaffaSnobb/master-tasks.

Chapter 2

Theory

2.1 Formalism

In this thesis I will use j for the *total* angular momentum, l for the *orbital* angular momentum, and s for the *spin* angular momentum. The term spin refers to the quantum mechanical intrinsic angular momentum, if not stated otherwise. Lower case l refers to the orbital angular momentum quantum number while upper case with a hat $\hat{L}_i, i \in \{x, y, z\}$ refers to operators. **Bold face** indicates vector quantities. The elements of a vector might be operators, and in that case we have for example the momentum operator

$$\mathbf{p} = -\mathrm{i}\hbar\nabla = -\mathrm{i}\hbar\left(\frac{\partial}{\partial x}, \frac{\partial}{\partial y}, \frac{\partial}{\partial z}\right) = (\hat{p}_x, \hat{p}_y, \hat{p}_z), \tag{2.1}$$

which makes $\mathbf{p}$ both a vector and an operator.

2.2 Basic quantum mechanical concepts

2.2.1 What is quantum mechanical spin?

Spin is one of the fundamental quantities in quantum physics and it is one of the first quantum mechanical concepts introduced to students of quantum physics. Yet, a simple explanation on what it actually is does not seem to exist! Quantum mechanics is well known for its many analogies, which without, we would have a terrible intuition on the quantum world. One of these analogies is revealed by the name *spin*. A reason for why we like to think that quantum mechanical spin is similar to classical spin is because it is easy to imagine a spinning ball. In classical physics, a ball might have two types of angular momentum. If the entire ball is rotating about some point in space, we call it *orbital angular momentum*. If the ball is rotating about its centre of mass, we call it *spin*. Actually, classical spin is nothing but a special case of orbital angular momentum where the constituents of the ball are all rotating about their collective centre of mass, meaning that the distinction is due to convenience and not due to a fundamental difference between the two.

However, in quantum physics there is an actual fundamental difference between orbital angular momentum and spin. Consider the electron which is

believed to be an elementary point particle. A point particle has no spatial size, which means it has no constituents which can collectively move about their centre of mass. In addition, it is impossible to change the magnitude of the spin of a particle. What crazy type of ball keeps spinning at the exact same rate no matter what you do to it? The classical analogy cannot be pushed too far, but it has its merits. For example, through *spin-orbit coupling*, angular momentum can be transferred between spin and orbital angular momentum. A particle with quantum mechanical spin can have a magnetic moment just like a rotating electrically charged body in classical electrodynamics. On a more technical note, the fundamental commutation relations of angular momentum

$$[\hat{L}_i, \hat{L}_j] = \mathrm{i}\hbar\epsilon_{ijk}\hat{L}_k, \tag{2.2}$$

is the same as the commutation relation for spin

$$[\hat{S}_i, \hat{S}_j] = \mathrm{i}\hbar\epsilon_{ijk}\hat{S}_k, \tag{2.3}$$

where ϵ is the Levi-Civita symbol. We know that the orbital angular momentum operators $\hat{L}_i, i \in \{x, y, z\}$ describe rotations in space, and since the two commutation relations are the same, it is tempting to use the analogy of quantum mechanical spin to a classically spinning object. As you might see, the quantum and classical similarities are many, but there are also stark differences. I believe this quote, of unknown origin, sums it all up quite beautifully:

> *Electron spin explained: Imagine a spinning ball. Except it is not spinning and it is not a ball.*

To summarise: Quantum mechanical spin is an intrinsic property of matter, just like mass and charge. It is in units of $\hbar$ and it is a type of angular momentum, meaning that angular momentum can be transferred between spin and orbital angular momentum. It is tempting to imagine quantum mechanical spin as a rotating ball, but this analogy must not be pushed too far since quantum and classical spin are fundamentally two different properties, which happen to have several similarities, both physically and mathematically.

I'll end this section with some food for thought. When Wolfgang Pauli theorised the electron spin for the first time in the 1920's, he did not call it spin, but rather *two-valuedness not describable classically* [4]. Maybe using the name *spin* was not such a good idea? Though it does roll better off the tongue!

2.2.2 Operators and commutators

In classical physics, the orbital angular momentum of a particle is given by

$$\mathbf{l} = \mathbf{r} \times \mathbf{p}, \tag{2.4}$$

where $\mathbf{r}$ is the position of the particle and $\mathbf{p}$ is the momentum. Getting to the quantum orbital angular momentum is easy; we just need to use the position and momentum quantum operators in place of the classical counterparts,

$$\begin{aligned} \mathbf{r} &= (\hat{x}, \hat{y}, \hat{z}), \\ \mathbf{p} &= -\mathrm{i}\hbar\nabla. \end{aligned} \tag{2.5}$$

Note that $\mathbf{p}$ and $\mathbf{r}$ are considered to be vectors in the classical definition and both vectors and operators in the quantum definition.

Now, take the orbital angular momentum operator $\mathbf{L} = (\hat{L}_x, \hat{L}_y, \hat{L}_z)$ as an example. Let ψ be an eigenfunction of the $\hat{L}^2$ operator. We extract the orbital angular momentum by

$$\begin{aligned} \hat{L}^2 &= \hat{L}_x^2 + \hat{L}_y^2 + \hat{L}_z^2, \\ \hat{L}^2\psi &= \hbar^2 l(l+1)\psi. \end{aligned} \tag{2.6}$$

The eigenvalue $\hbar^2 l(l+1)$ can be thought of as the squared magnitude of the orbital angular momentum vector, but it is common to refer to l as the orbital angular momentum of the system represented by ψ[1]. A fundamental part of the theory of quantum angular momentum is that the operator $\hat{L}^2$ *commutes* with the operators $\hat{L}_x$, $\hat{L}_y$ and $\hat{L}_z$, or in other words

$$[\hat{L}^2, \mathbf{L}] = 0. \tag{2.7}$$

This means that $\hat{L}^2$ and $\hat{L}_i, i \in \{x, y, z\}$ are *compatible* observables. Compatible observables means that both operators in each pair represent observable quantities and that they can be measured at the same time with arbitrary precision. This is seen from the generalised uncertainty principle, which for these pairs of operators is

$$\sigma_{\hat{L}^2}^2 \sigma_{\hat{L}_i}^2 \geq \left| \frac{1}{2\mathrm{i}} \langle [\hat{L}^2, \hat{L}_i] \rangle \right| = 0. \tag{2.8}$$

Equation (2.8) tells us that the expectation values of $\hat{L}^2$ and $\hat{L}_i$ can both have a standard deviation of zero at the same time, which in turn says that the magnitude and the z component of the orbital angular momentum can be precisely measured at the same time. On the other hand, the components of $\mathbf{L}$ do not commute with each other. In fact [5]

$$\begin{aligned} [\hat{L}_x, \hat{L}_y] &= \mathrm{i}\hbar\hat{L}_z, \\ [\hat{L}_y, \hat{L}_z] &= \mathrm{i}\hbar\hat{L}_x, \\ [\hat{L}_z, \hat{L}_x] &= \mathrm{i}\hbar\hat{L}_y, \end{aligned} \tag{2.9}$$

meaning that we cannot hope to measure any pair of these values without uncertainty in at least one of them, making them *incompatible* observables.

Due to the limitations which the aforementioned commutation relations impose on us, it is normal to measure (or calculate) l from the eigenvalue

[1] l is also called the angular momentum quantum number and the azimuthal quantum number.

produced by the $\hat{L}^2$ operator and the eigenvalue from one of the components of $\mathbf{L}$. The choice of axis really is arbitrary, but it is common to pick the $\hat{L}_z$ operator. The eigenvalue equation reads

$$\hat{L}_z\psi = \hbar l_z \psi, \tag{2.10}$$

where l_z can be thought of as the z component of l [2].

In the next section we will see that it is indeed fruitful and mathematically correct to think of quantum mechanical angular momentum as vector quantities. Note that the commutation relations of the total angular momentum operators $\mathbf{J}$, and the spin operators $\mathbf{S}$ follow the exact same rules as described here for the orbital angular momentum operators $\mathbf{L}$. The squared of the operator commutes with each of the components, while the components themselves do not commute with each other [5].

2.2.3 Coupling of angular momentum vectors

In classical physics, spin $\mathbf{s} = (s_x, s_y, s_z)$ and orbital angular momentum $\mathbf{l} = (l_x, l_y, l_z)$ are represented by real vectors in three dimensional space: $\mathbf{s}, \mathbf{l} \in \mathbb{R}^3$ [3]. They also hold the same unit and can therefore easily be added together, without much thought, to create a total angular momentum vector

$$\mathbf{j} = \mathbf{l} + \mathbf{s}. \tag{2.11}$$

This simply means that the components of $\mathbf{j}$ are the sum of the components of $\mathbf{l}$ and $\mathbf{s}$, namely

$$\mathbf{j} = (l_x + s_x, l_y + s_y, l_z + s_z). \tag{2.12}$$

Squaring the vector is an easy process where we use the normal rules for the vector dot product and distributive multiplication

$$\begin{aligned} j^2 &= (\mathbf{l} + \mathbf{s})(\mathbf{l} + \mathbf{s}) \\ &= l^2 + 2\mathbf{l} \cdot \mathbf{s} + s^2. \end{aligned} \tag{2.13}$$

Can we do the same thing in the quantum case? Let us look at the quantum total angular momentum $\mathbf{J}$. Remember, it is the squared operator we want since it commutes with any of the component operators. It is tempting to do just as in eq. (2.13), but we must be careful; remember that the components of $\mathbf{S}$ and $\mathbf{L}$ are operators. What does it mean to add together vectors whose elements are operators, and different types of operators at that? Let us start by looking at $\hat{J}_z$, which in the classical case would just be the sum of $\hat{S}_z$ and $\hat{L}_z$. The operators $\hat{S}_z$ and $\hat{L}_z$ are actually working on different Hilbert spaces which means that we add them as

$$\hat{J}_z = \hat{L}_z \otimes \mathbb{1}_S + \mathbb{1}_L \otimes \hat{S}_z. \tag{2.14}$$

[2] The value l_z is normally denoted m_l or just m and is sometimes referred to as the magnetic quantum number.

[3] I'm using lower case letters just to make sure we do not confuse them with the QM "vector operators" $\mathbf{S} = (\hat{S}_x, \hat{S}_y, \hat{S}_z)$, $\mathbf{L} = (\hat{L}_x, \hat{L}_y, \hat{L}_z)$ and $\mathbf{J} = (\hat{J}_x, \hat{J}_y, \hat{J}_z)$.

$\mathbb{1}_S$ and $\mathbb{1}_L$ are the identity operators for spin and orbital angular momentum respectively, while $\otimes$ denotes the tensor product. Remember that we want $\hat{J}^2 = \hat{J}_x^2 + \hat{J}_y^2 + \hat{J}_z^2$ so we need to square each component. Squaring $\hat{J}_z$ gives

$$\begin{aligned}\hat{J}_z^2 &= (\hat{L}_z \otimes \mathbb{1}_S)(\hat{L}_z \otimes \mathbb{1}_S) + (\hat{L}_z \otimes \mathbb{1}_S)(\mathbb{1}_L \otimes \hat{S}_z) \\ &+ (\mathbb{1}_L \otimes \hat{S}_z)(\hat{L}_z \otimes \mathbb{1}_S) + (\mathbb{1}_L \otimes \hat{S}_z)(\mathbb{1}_L \otimes \hat{S}_z) \\ &= \hat{L}_z\hat{L}_z \otimes \mathbb{1}_S\mathbb{1}_S + \hat{L}_z\mathbb{1}_L \otimes \mathbb{1}_S\hat{S}_z \\ &+ \mathbb{1}_L\hat{L}_z \otimes \hat{S}_z\mathbb{1}_S + \mathbb{1}_L\mathbb{1}_L \otimes \hat{S}_z\hat{S}_z \\ &= \hat{L}_z^2 \otimes \mathbb{1}_S + 2\hat{L}_z \otimes \hat{S}_z + \mathbb{1}_L \otimes \hat{S}_z^2.\end{aligned} \tag{2.15}$$

The x and y components are analogous to eq. (2.15) (just swap the labels). We now add the squared components

$$\begin{aligned}\hat{J}^2 &= \sum_{i=x,y,z} (\hat{L}_i^2 \otimes \mathbb{1}_S + 2\hat{L}_i \otimes \hat{S}_i + \mathbb{1}_L \otimes \hat{S}_i^2) \\ &= \hat{L}_x^2 \otimes \mathbb{1}_S + \hat{L}_y^2 \otimes \mathbb{1}_S + \hat{L}_z^2 \otimes \mathbb{1}_S \\ &+ 2(\hat{L}_x \otimes \hat{S}_x + \hat{L}_y \otimes \hat{S}_y + \hat{L}_z \otimes \hat{S}_z) \\ &+ \mathbb{1}_L \otimes \hat{S}_x^2 + \mathbb{1}_L \otimes \hat{S}_y^2 + \mathbb{1}_L \otimes \hat{S}_z^2 \\ &= \hat{L}^2 \otimes \mathbb{1}_S + 2(\hat{L}_x \otimes \hat{S}_x + \hat{L}_y \otimes \hat{S}_y + \hat{L}_z \otimes \hat{S}_z) + \mathbb{1}_L \otimes \hat{S}^2.\end{aligned} \tag{2.16}$$

This final equality has similarities to eq. (2.13). We have two squared terms and a cross term, thus we might be tempted to write eq. (2.16) in shorthand as

$$\hat{J}^2 = \hat{L}^2 + 2\mathbf{L} \cdot \mathbf{S} + \hat{S}^2. \tag{2.17}$$

Neat! The "classical approach" in eq. (2.13) actually gets us to the correct answer for the quantum case, if we are a bit liberal with the notation![4] We can now meaningfully combine the spin and orbital angular momentum of a quantum system to create a (squared) total angular momentum operator. And what's more, we are able to treat the different forms of quantum angular momentum as vector quantities, which greatly simplifies the maths[5].

We cannot talk about the theory of angular momentum without taking special care of the famous z component. From section 2.2.2 we saw that $[\hat{J}^2, \hat{J}_z] = 0$, which means that we can decide both the magnitude and the z component of an angular momentum vector at the same time (remember that this holds for $\hat{L}^2$ and $\hat{S}^2$ too). We have seen that the eigenvalue of $\hat{J}_z$ is the z component of the vector, namely $\hbar j_z$ ($\hbar$ is often omitted for brevity). The magnitude of the z component is of course constrained by the magnitude of j, and in particular, j_z can take values of integer steps from $-j$ to j. Figure 2.1 shows the possible j_z values for a system of $j = 2$. Since j_x and j_y are undefined when j_z is defined, the magnitude of j is represented

[4] By liberal I of course mean sloppy!

[5] It is not obvious that it is correct to treat quantum angular momentum as vector quantities since the vector operator quantities $\mathbf{S}, \mathbf{L}, \mathbf{J}$ have component operators which do not commute. How can we define angular momentum vectors if only one component can be precisely given at any time? Turns out that maths is on our side this time!

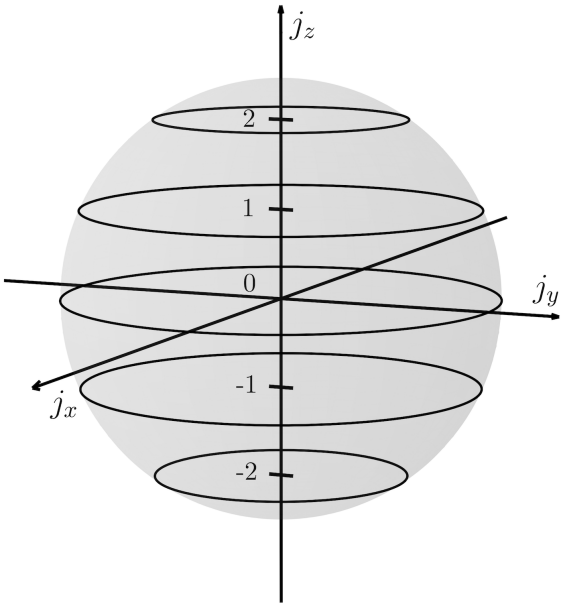

Figure 2.1: The possible j_z values of a system of $j = 2$. The radius of the sphere is $\hbar\sqrt{j(j+1)}$; the magnitude of the angular momentum vector. The circles at each j_z value indicate the indeterminacy of j_x and j_y when j_z is defined. The axes are in units of $\hbar$.

as circles for each j_z. Of particular interest is the fact that the radius of the sphere, $\hbar\sqrt{j(j+1)}$, is greater than the maximum j_z value. This saves us from the situation where the entire angular momentum vector is contained in the z component, which cannot possibly be, because then $j_x = j_y = 0$ and we would know all the components to perfect precision which is in direct conflict with the uncertainty principle. Since $j_z \leq j < \sqrt{j(j+1)}$, we see that the entire length of the angular momentum vector will never be contained in j_z, leaving some possibility of uncertainty for j_x and j_y.

Let us now look at an example on how j, l, and s couple. Assume a particle of total angular momentum j_1, orbital angular momentum l_1, and spin s_1. Its total angular momentum is a combination of its orbital angular momentum and spin, but how do they combine? Remember that angular momentum can be treated as a vector quantity. The orbital angular momentum points in some direction and the spin points in some direction, meaning that they might be parallel ($j_1 = l_1 + s_1$), antiparallel ($j_1 = l_1 - s_1$), or something in between. The very essence of quantum physics is that many fundamental properties come in discrete values, and the coupling of angular momentum and spin is no exception. The total angular momentum can be any of the values in the range

$$j_1 = l_1 + s_1, l_1 + s_1 - 1, ..., |l_1 - s_1| \tag{2.18}$$

of integer steps, and if we assume spin $1/2$ particles we see that

$$j_1 = l_1 + 1/2, |l_1 - 1/2|. \tag{2.19}$$

Angular momentum coupling does not only apply to orbital angular momentum and spin, but also the total angular momenta of several particles. Assume now a second particle of total angular momentum j_2. We can combine the angular momenta of particles 1 and 2 to create a total angular momentum of the system of particles by

$$j = j_1 + j_2, j_1 + j_2 - 1, ..., |j_1 - j_2|. \tag{2.20}$$

2.2.4 Parity

To explain parity, it is fruitful to start with understanding what a *parity transformation* is. A parity transformation is a space reflection about the origin of the coordinate system. It is represented by a hermitian and unitary operator $\hat{\pi}$ which is defined by its action

$$\hat{\pi}\psi(\mathbf{r}) = \psi(-\mathbf{r}), \tag{2.21}$$

an action which flips the sign of all the spatial coordinates of ψ. The hermiticity and unitarity of $\hat{\pi}$ implies that it's eigenvalues are $\lambda = \pm 1$ [6]. The *parity* of a quantum mechanical system is the eigenvalue of the parity operator when operating on the wave function of said system. The parity can thus either be positive $(+1)$ or negative (-1).

One apparent problem is that ψ is not necessarily an eigenfunction of the parity operator, in which case the parity is not a well defined quantum number. For us to use parity as a tool we therefore need to consider operators which share eigenfunctions with the parity operator. We know that commuting observable operators share complete sets of eigenfunctions, and in particular

$$\hat{\pi}\mathbf{L}\hat{\pi}^\dagger = \hat{\pi}\mathbf{x}\hat{\pi}^\dagger \times \hat{\pi}\mathbf{p}\hat{\pi}^\dagger = -\mathbf{x} \times -\mathbf{p} = \mathbf{L}, \tag{2.22}$$

which tells us that $\hat{\pi}$ and $\mathbf{L}$ commute and consequently that we can find wave functions which are eigenfunctions of both angular momentum and parity.

2.3 Electromagnetic transitions

In nuclear physics there are three main types of radiation: alpha and beta radiation are two types of particle radiation while gamma radiation is electromagnetic radiation. Gamma radiation is at the heart of nuclear physics because each and every isotope have a unique electromagnetic signature which reveals the identity and the underlying structure of the nucleus. Gamma radiation is mediated by the photon which is the electromagnetic force carrier. The photon has a spin of 1 and a parity of -1, which makes gamma radiation subject to certain rules. To make sense of these rules, we classify gamma radiation by a *multipolarity*, which is defined by the angular momentum of the emitted photon and the parity of the radiation. In this section we will have a closer look at what exactly multipolarity means and the selection rules that emerge.

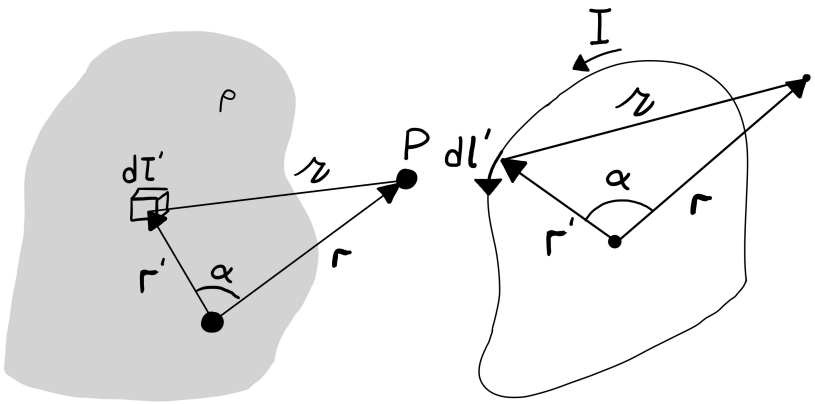

Figure 2.2: Left: An arbitrary charge distribution. $d\tau'$ is an infinitesimal volume element whose position is $\mathbf{r}'$, $\mathbf{r}$ is the position of a point P outside of the charge distribution, ρ is the charge density, $\mathscr{r} = |\mathbf{r} - \mathbf{r}'|$ and α is the angle between $\mathbf{r}$ and $\mathbf{r}'$. Right: A current loop of current I. $d\mathbf{l}'$ is an infinitesimal line element of the current loop.

2.3.1 Multipole expansion

From electromagnetic theory we know that a distribution of charges and currents may exert electric and magnetic fields which we categorise by their multipolarities. Now, what does multipolarity mean? Let us start the investigation by looking at the potential of the electric field produced by an arbitrary static charge distribution, which is given by [7]

$$\begin{aligned} \mathbf{E} &= -\nabla V \\ V(\mathbf{r}) &= \frac{1}{4\pi\epsilon_0}\int \frac{1}{\mathscr{r}}\rho(\mathbf{r}')d\tau', \end{aligned} \tag{2.23}$$

where ϵ_0 is the vacuum permittivity. See fig. 2.2 for a description of the variables. The distance $\mathscr{r}$ can be re-written using the law of cosines

$$\begin{aligned} \mathscr{r}^{\,2} &= r^2 + r'^2 - 2rr'\cos\alpha \\ &= r^2\left(1 + \left(\frac{r'}{r}\right)^2 - 2\left(\frac{r'}{r}\right)\cos\alpha\right) \\ &= r^2\left(1 + \left(\frac{r'}{r}\right)\left(\frac{r'}{r} - 2\cos\alpha\right)\right) \\ &\overset{\text{def}}{=} r^2\left(1+\epsilon\right). \end{aligned} \tag{2.24}$$

Since $\lim_{r\to\infty}\epsilon = 0$ we can choose points P outside of the charge distribution so that $\epsilon < 1$ which enables us to expand $1/\mathscr{r}$ as a binomial series, giving

$$\begin{aligned} \frac{1}{\mathscr{r}} &= \frac{1}{r}(1+\epsilon)^{-1/2} \\ &= \frac{1}{r}\left(1 - \frac{1}{2}\epsilon + \frac{3}{8}\epsilon^2 - \frac{5}{16}\epsilon^3 + ...\right). \end{aligned} \tag{2.25}$$

If we now substitute ϵ with its original definition and factor and collect equal powers of r'/r we get

$$\begin{aligned}\frac{1}{\mathscr{r}} &= \frac{1}{r}\left(1 + \left(\frac{r'}{r}\right)\cos\alpha + \left(\frac{r'}{r}\right)^2\left(\frac{3\cos^2\alpha - 1}{2}\right)\right. \\ &\quad \left. + \left(\frac{r'}{r}\right)^3\left(\frac{5\cos^3\alpha - 3\cos\alpha}{2} + ...\right)\right) \\ &= \frac{1}{r}\sum_{n=0}^{\infty}\left(\frac{r'}{r}\right)^n P_n(\cos\alpha).\end{aligned} \tag{2.26}$$

Notice that the coefficients in eq. (2.26) are the Legendre polynomials! Substituting eq. (2.26) into eq. (2.23) gives the final result:

$$V(\mathbf{r}) = \frac{1}{4\pi\epsilon_0}\sum_{n=0}^{\infty}\frac{1}{r^{n+1}}\int (r')^n P_n(\cos\alpha)\rho(\mathbf{r}')d\tau'. \tag{2.27}$$

Equation (2.27) is the *multipole expansion* of the electric potential V. The multipole expansion gives us important information on the components that build up V, much like what the Fourier Series provides in harmonic analysis. The first few terms ($n \in \{0, 1, 2, 3\}$ respectively) of the multipole expansion are

$$\begin{aligned}V_{\text{mono}}(\mathbf{r}) &= \frac{1}{4\pi\epsilon_0}r^{-1}\int \rho(\mathbf{r}')d\tau' \\ V_{\text{di}}(\mathbf{r}) &= \frac{1}{4\pi\epsilon_0}r^{-2}\int r'\cos\alpha\rho(\mathbf{r}')d\tau' \\ V_{\text{quad}}(\mathbf{r}) &= \frac{1}{4\pi\epsilon_0}r^{-3}\int (r')^2\frac{1}{2}(3\cos^2\alpha - 1)\rho(\mathbf{r}')d\tau' \\ V_{\text{octu}}(\mathbf{r}) &= \frac{1}{4\pi\epsilon_0}r^{-4}\int (r')^3\frac{1}{2}(5\cos^3\alpha - 3\cos\alpha)\rho(\mathbf{r}')d\tau',\end{aligned} \tag{2.28}$$

which are named monopole, dipole, quadrupole, and octupole respectively. The different terms in the expansion are in particular characterised by their dependence on r where we see that $V_{n=i}(\mathbf{r}) \propto r^{-(i+1)}$ which means that, as a function of the distance to the charge distribution, the higher order terms vanish faster than the lower order terms. The implication of this is that only the first few terms in the expansion are important when describing the potential at large r. The second important characterisation is the integral's dependence on the Legendre polynomials, and in turn the potential's dependence on the angle α. In fig. 2.3 we see a plot of the first four Legendre polynomials, which illustrates that the different multipolarities have different angular dependencies.

We now give the same treatment for the magnetic case. The magnetic field $\mathbf{B}$ can be expressed in terms of a magnetic vector potential $\mathbf{A}$, namely

$$\mathbf{B} = \nabla \times \mathbf{A}. \tag{2.29}$$

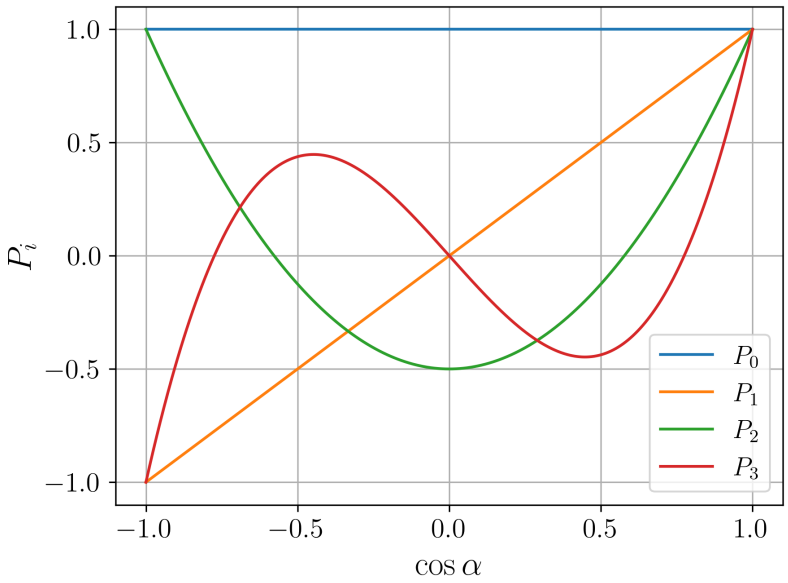

Figure 2.3: Legendre polynomials for $n \in \{0, 1, 2, 3\}$ as a function of the cosine of α. See fig. 2.2 for a description of α.

The magnetic vector potential for a current loop is given by

$$\mathbf{A}(\mathbf{r}) = \frac{\mu_0 I}{4\pi} \oint \frac{1}{\mathscr{r}} d\mathbf{l}' \tag{2.30}$$

and can be expanded as a power series in the same manner as V to produce the Legendre polynomials as the coefficients [7]

$$\mathbf{A}(\mathbf{r}) = \frac{\mu_0 I}{4\pi} \sum_{n=0}^{\infty} \frac{1}{r^{n+1}} \oint (r')^n P_n(\cos\alpha) d\mathbf{l}'. \tag{2.31}$$

μ_0 is the vacuum permeability and the rest of the variables are visualised in fig. 2.2. The first four terms in the expansion are

$$\begin{aligned}
\mathbf{A}_{\text{mono}}(\mathbf{r}) &= \mathbf{0} \\
\mathbf{A}_{\text{di}}(\mathbf{r}) &= \frac{\mu_0 I}{4\pi} r^{-2} \oint r' \cos\alpha d\mathbf{l}' \\
\mathbf{A}_{\text{quad}}(\mathbf{r}) &= \frac{\mu_0 I}{4\pi} r^{-3} \oint (r')^2 \frac{1}{2}(3\cos^2\alpha - 1) d\mathbf{l}' \\
\mathbf{A}_{\text{octu}}(\mathbf{r}) &= \frac{\mu_0 I}{4\pi} r^{-4} \oint (r')^3 \frac{1}{2}(5\cos^3\alpha - 3\cos\alpha) d\mathbf{l}'
\end{aligned} \tag{2.32}$$

where we see the same r dependence as with V, as well as the same dependence of the Legendre polynomials, except for the magnetic monopole term which is zero[6]. As with the multipole expansion of V, the multipolarity refers to a specific term in the expansion of eq. (2.31).

[6]This comes from one of the base assumptions of electromagnetism that $\nabla \cdot \mathbf{B} = 0$. This is Gauss' law for magnetism, one of Maxwell's equations.

To summarise, when we talk about monopole, dipole, etc. of electromagnetic radiation we refer to specific terms in the multipole expansion of the electric scalar potential V and the magnetic vector potential $\mathbf{A}$. The terms in the expansion are characterised by their dependence on the distance to the source and by their angular dependence which is given by the Legendre polynomials. In addition to the multipolarity of radiation, we assign it an electric (E) or magnetic (M) label. This simply means that radiation labelled, for example, $E1$ (electric dipole) is identical to radiation from an electric dipole antenna. Radiation labelled $M2$ is identical to the radiation from a magnetic quadrupole antenna, etc. Note that the expansions shown in this section take basis in *static* electric and magnetic fields. Using static fields in the derivations do not tell the complete story since electromagnetic radiation inherently is dynamic. However, the maths is greatly simplified by using static fields, and the point of this section is to explain what we mean by multipolarity which I believe has now been clearly explained. Any reader keen on exploring multipole expansion of dynamic fields may take a look at for example Ring and Schuck Appendix B [8].

2.3.2 Selection rules

When an excited nucleus decays from an initial state ψ_i to a final state ψ_f a photon is emitted[7]. The initial and final total angular momenta and parities j_i, π_i, j_f, π_f decide the characteristics of the emitted photon. For instance, the photon will carry a total angular momentum j_γ defined by its spin of $s_\gamma = 1$, along with j_i, j_f, and the rules of angular momentum coupling. The "leftover" angular momentum from the transition between the initial and final state is carried away as spin and orbital angular momentum of the emitted photon. The emitted photon will have a total angular momentum of

$$j_\gamma = j_i + j_f, j_i + j_f - 1, ..., |j_i - j_f|, \tag{2.33}$$

with a minimum of $j_\gamma = 1$ due to $s_\gamma = 1$. This means that $E0$ gamma radiation is impossible which in particular makes $0^\pm \rightarrow 0^\pm$ transitions impossible by gamma radiation, though possible by internal conversion. $M0$ transitions are of course not possible due to the absence of magnetic monopoles.

In addition to conservation of angular momentum, parity must also be conserved in an electromagnetic transition. A photon of multipolarity Ej_γ and a photon of multipolarity Mj_γ have parities of

$$\begin{aligned} \pi_{\gamma,E} &= (-1)^{j_\gamma}, \\ \pi_{\gamma,M} &= (-1)^{(j_\gamma+1)}, \end{aligned} \tag{2.34}$$

respectively. Remember that parity is a conserved multiplicative quantity; the parity of a system before a transition must be equal to the parity of the

[7]Except for the case of $0^+ \rightarrow 0^+ E0$ transitions where an atomic electron is ejected by the process of internal conversion.

system after the transition, and the individual parities of the particles in the system are multiplied to give the total parity. In other words, if we start with an initial state of parity π_i and end in a state of π_f, then

$$\pi_i = \pi_f \pi_\gamma. \tag{2.35}$$

We see from eq. (2.35) that

$$\begin{aligned} \pi_i \neq \pi_f, \pi_\gamma = -1 \\ \pi_i = \pi_f, \pi_\gamma = +1 \end{aligned} \tag{2.36}$$

and subsequently from eq. (2.34) that if there is a change in parity in a transition ($\pi_i \neq \pi_f$), the multipolarity must be even numbered magnetic

$$M2, M4, M6, ...$$

or odd numbered electric

$$E1, E3, E5, ...$$

Conversely, transitions which do not change parity ($\pi_i = \pi_f$) must be odd numbered magnetic or even numbered electric.

2.4 Nuclear properties

2.4.1 Nuclear level density

The *nuclear level density* (NLD) is a property of the atomic nucleus which describes how many *nuclear energy levels* are found within an excitation energy bin ΔE. When a nucleus absorbs energy, for example in the form of electromagnetic radiation, we say that the nucleus is in an *excited state*[8]. The nucleus can only absorb energy in certain quanta, of which the magnitude is different for different nuclei, and these energy quanta are the nuclear energy levels. The NLD is defined as

$$\rho(E_x) = \frac{\Delta N}{\Delta E} \tag{2.37}$$

where ΔN is the number of levels within the excitation energy bin ΔE at excitation energy E_x. Each level is characterised not only by E_x, but also by its total angular momentum and parity, commonly denoted j^π. A useful tool is the *partial* level density which takes into account the density as a function of E_x, j, and π. It relates to the *total* level density by

$$\rho(E_x) = \sum_{j,\pi} \rho(E_x, j, \pi). \tag{2.38}$$

[8]The word *state*, as in *condition*, is used a bit casually here. Strictly speaking, the terms *level* and *state* have different meanings. A quantum state is a precise choice of quantum numbers (eg. s, l, j, π), while several distinct quantum states may have the same energy level. We then call the energy level *degenerate*.

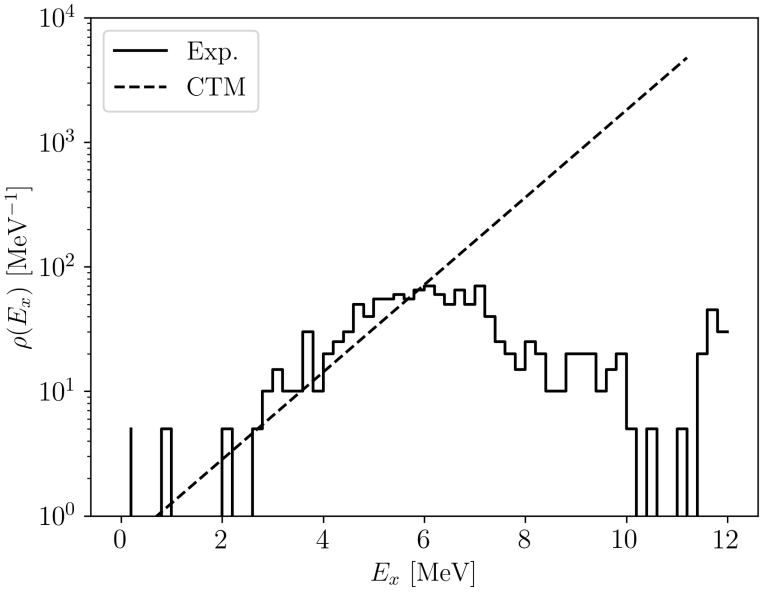

Figure 2.4: The experimental nuclear level density of ^{56}Fe in solid lines compared with the constant temperature model (CTM) in dashed lines. A bin size of $\Delta E_x = 0.2$ MeV has been used. Experimental data from [10].

Due to experimental limitations, measuring the number of levels is a difficult task, particularly at excitation energies above a few MeVs. This is because the number of levels quickly increases as a function of excitation energy and at a few MeVs there can be hundreds of levels within an energy interval. We might therefore use models to extrapolate beyond what is possible to measure. A commonly used model is the *constant temperature model* (CTM) [9]. An important detail is that we expect the NLD to rise exponentially like we see from the definition of the CTM

$$\rho_{\mathrm{CTM}}(E_x) = \frac{1}{T} \exp\left(\frac{E_x - E_0}{T}\right), \tag{2.39}$$

where T is the constant nuclear temperature and E_0 is the energy shift parameter, both free parameters which are decided by fits to experimental data. In fig. 2.4 we see the experimental NLD of ^{56}Fe compared to the CTM. The experimental data rises exponentially up to approximately 6 MeV from where it starts to fall. The decrease beyond 6 MeV is due to experimental limitations and in reality we expect the NLD to keep increasing exponentially like we see from the CTM.

The *lifetime* τ is another defining characteristic of nuclear energy levels. An excited nucleus wants to get rid of as much energy as possible, meaning that it will not stay excited indefinitely. Even if we had no experimental limitations on the time resolution, repeated measurements of how long an excited nucleus of a given energy level stays at that level will not yield exactly the same result every time. The measurements would yield a distribution

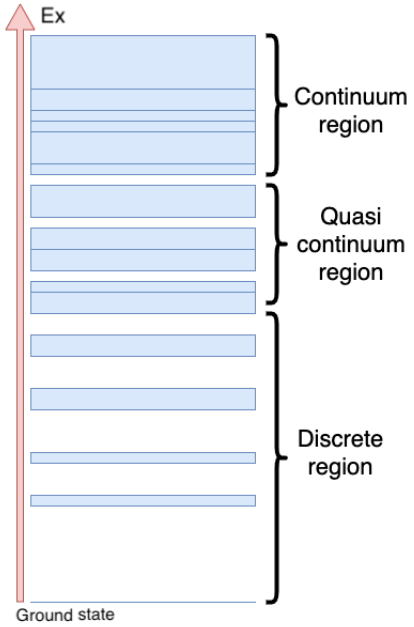

Figure 2.5: An arbitrary level scheme in order of increased excitation energy. Levels are depicted by blue lines, and the thickness of the lines illustrate the decay width Γ of the levels. Note that the thicknesses are exaggerated for illustrative purposes. The ground state is infinitely thin since $\tau_{\text{gs}} = \infty$ is assumed for the arbitrary level scheme in this figure, but unstable nuclei like ^{44}Sc, ^{50}V, and ^{64}Zn will have a finite ground state width. Figure modified and reprinted with permission from [11].

of times, and we define the lifetime of a level as the average of many such measurements.

Recall the time-energy uncertainty relation

$$\Delta E \Delta \tau \geq \frac{\hbar}{2} \tag{2.40}$$

which states that we cannot measure both the lifetime and the energy of a level to an arbitrary good precision at the same time. Naturally, this means that if we perform an experiment where we measure the energy of a level with great precision, then we are forced to have a loss of precision in a lifetime measurement of the same level. However, a rather interesting consequence of the time-energy uncertainty is that a level with a very short lifetime has to have a large uncertainty to its energy. This point is besides the precision of our measurements; the short lifetime forces a certain amount of uncertainty in the energy measurements regardless of the precision of our instruments. This inherent energy uncertainty, which we cannot get rid of, is used in the definition of the *decay width* Γ. It is defined by

$$\Gamma = 2\Delta E = \frac{\hbar}{\tau} \tag{2.41}$$

and is measured in units of energy. Every nuclear energy level has an associated decay width, and this width is a defining characteristic of the

three nuclear energy level regions. Note that an excited level might have several different *decay channels*, which means that the excited level might decay to one of several lower lying levels. We then assign a *partial decay width* Γ_i to the ith decay channel, and if we sum all of the partial decay widths we get the total decay width of the excited level, namely

$$\Gamma = \sum_i \Gamma_i. \tag{2.42}$$

In fig. 2.5 we see a scheme of levels (blue lines) arranged according to increasing excitation energy. The thickness of the lines illustrate the decay width of the levels. In the discrete region the energy separation of the levels is much greater than the width of the levels. However, in the quasi continuum region, the energy separation of the levels starts to approach the width of the levels. In the continuum region the levels completely overlap.

Recall from the definition of the NLD in eq. (2.37) that the NLD is calculated in an energy interval. A typical value of the energy interval is $\Delta E = 0.2$ MeV, and note that such an energy interval might not contain any levels in the discrete region. We actually see this experimentally in fig. 2.4, that the NLD is zero at several bins below 3 MeV. This fact has implications on the gamma strength function and the generalised Brink-Axel hypothesis which will be presented in the next sections.

2.4.2 The gamma strength function

The *gamma strength function*[9] (GSF) is an essential tool for studying decay properties of the atomic nucleus and it is the main focus of this thesis. The GSF describes average electromagnetic transition probabilities in excited nuclei; it is a measure of the probability that an excited nucleus will decay with a gamma of energy E_γ which has a total angular momentum of j_γ, from some initial energy level E_i of total angular momentum and parity j_i and π_i respectively. The GSF is given by [12]

$$\begin{aligned} f_{Xj_\gamma}(E_\gamma, E_i, j_i, \pi_i) &= \frac{\langle \Gamma^{Xj_\gamma} \rangle (E_\gamma, E_i, j_i, \pi_i)}{E_\gamma^{2j_\gamma+1}} \rho(E_i, j_i, \pi_i), \\ &= \frac{16\pi}{9\hbar^3 c^3} \langle B(Xj_\gamma) \rangle (E_\gamma, E_i, j_i, \pi_i) \rho(E_i, j_i, \pi_i), \end{aligned} \tag{2.43}$$

where Xj_γ is the multipolarity of the gamma radiation, as described in section 2.3, Γ^{Xj_γ} is the partial decay width of a level at E_i, j_i, π_i which decays by a gamma of E_γ with a multipolarity of Xj_γ, $\langle \Gamma^{Xj_\gamma} \rangle$ is the average partial decay width, B is the reduced transition probability, and ρ is the *partial* level density. The average is taken in an interval around excitation energy E_i for gamma energies in an interval around E_γ. The interval, also called bin or energy bin, typically has a value of 0.2 MeV.

[9] Also called the radiative strength function, the photon strength function, or just the strength function.

2.4.3 The generalised Brink-Axel hypothesis

By averaging the GSF over initial energies, total angular momenta, and both parities, we can look at the GSF solely as a function of E_γ making it an excellent tool to probe the preferred gamma energy decay channels of a nucleus. But is it correct to perform these averages? By doing so, we are effectively stating that

$$f(E_\gamma) \approx f(E_\gamma, E_i, j_i, \pi_i), \tag{2.44}$$

which is to say that the GSF calculated at some choice of E_i, j_i, π_i should be approximately equal to the GSF calculated at some other choice of E_i, j_i, π_i. In his doctoral thesis, David M. Brink proposed – in the context of $E1$ excitations of even-even nuclei – that the cross-section to excite the nucleus is independent of whether the excitation happens from the ground state or from an excited state [13]. Over the years, Brink's hypothesis has been expanded to include independence of electromagnetic character, multipolarity, angular momentum, and parity, to become the generalised Brink-Axel hypothesis (gBA) [14, 15, 16]. However, it is important to note that the gBA hypothesis does not hold for all nuclei under all circumstances. For example, Bracco et. al. found that the widths of the Giant Dipole Resonance (GDR) of ^{109,110}Sn increased by 2 MeV in the angular momentum interval $j = [40, 55]\hbar$ [17]; however, the GDR exists at rather higher energies than what will be considered in this work, and the changes in the GDR width were seen at much higher angular momenta than what will be used in this work. An example more relevant to this thesis is that the gBA hypothesis is not valid in the discrete level region, as shown by this example: In the gBA hypothesis one assumption is that

$$f(E_\gamma, j_i = j_1) \approx f(E_\gamma, j_i = j_2), \tag{2.45}$$

but there is no guarantee that levels of both j_1 and j_2 exist in all excitation energy bins in the discrete region, in this case making eq. (2.45) invalid. In fact, look at the level scheme for any nucleus and you will see that an excitation energy bin of size around 200 keV will only contain a few (if any!) levels if applied to the discrete region and will consequently only contain a few different j_i values. The same logic goes for π_i. This problem is mitigated by excluding discrete levels by setting a lower limit to E_i.

For this thesis I have performed a simplified check to test the validity of gBA on my calculations and I have added a proposal in appendix C on how to extend this check more thoroughly. The extension has not been implemented in this work due to time limitations. In the simplified check I test the GSF's approximate independence of j_i by calculating the GSF separately for all available values j_i with

$$f(E_\gamma, j_i) = \frac{1}{N_{E_i} N_{\pi_i}} \sum_{N_{E_i}, N_{\pi_i}} f(E_\gamma, E_i, j_i, \pi_i), \tag{2.46}$$

for then to compare them to each other and to $f(E_\gamma)$. Due to the statistical nature of lifetimes, and hence Γ and B, I expect that eq. (2.46) will not

be identical for different choices of j_i. In other words, I expect that the differences in the GSFs for different choices of j_i will be affected by the number of B values used in the calculations. Since the GSF describes *average* transition probabilities I expect from the law of large numbers that the sample mean will approach the true expectation value of the underlying distribution as the number of samples increase [18].

Following the work of J. Midtbø (see sec. 3.2 in [12]) we can turn eq. (2.43) around to get

$$\langle B(Xj_\gamma)\rangle(E_\gamma, E_i, j_i, \pi_i) = \frac{9\hbar^3 c^3}{16\pi} \frac{f_{Xj_\gamma}(E_\gamma, E_i, j_i, \pi_i)}{\rho(E_i, j_i, \pi_i)}, \tag{2.47}$$

from where we see that f can be interpreted as providing the mean value of the probability distribution of reduced transition probabilities B. Every B value will have a relative difference to the mean B value given by

$$y = \frac{B}{\langle B\rangle}, \tag{2.48}$$

and this variation is often assumed to be given by the χ^2 distribution with one degree of freedom,

$$y \sim \chi^2_1, \tag{2.49}$$

a distribution which is also called the *Porter-Thomas distribution* [19]. Fluctuations in B values within the expected fluctuations from a Porter-Thomas distributed random variable are referred to as *Porter-Thomas fluctuations*. Hence, differences in eq. (2.46) between different j_i should be within the expected Porter-Thomas fluctuations. If they are not, something else is causing the difference and we can not assume the gBA hypothesis.

2.4.4 The low energy enhancement

The *low energy enhancement* (LEE) is a feature of the low energy part of the GSF. If the GSF of a nucleus increases as E_γ approaches zero, then the GSF is said to have a low energy enhancement. The LEE has several different names including *soft pole* [20], *upbend* [21], and *low energy magnetic radiation* [22], names which are useful to know for anyone who wishes to research the LEE.

The LEE was first seen in ^{56,57}Fe by Emel Tavukcu in her 2002 PhD dissertation [23]. Tavukcu found that the GSFs of the two nuclei had a distinct increase at the lowest gamma ray energies, something which was most unexpected at the time because it didn't fit with any of the current models. Tavukcu's discoveries are shown in fig. 2.6 where we see GSFs for both iron isotopes. Note the enhancements of the GSFs as E_γ approaches zero, and note that the models included in the figure (KMF, GMDR, GEDR) do not reproduce the LEE. Due to the uncertainty about the LEE, two years went by before a Letter by Voinov et. al. was published with the ^{56,57}Fe findings [24]. In the subsequent years, several publications claimed to support and to oppose the existence of the LEE, but after an independent experiment by Wiedeking et. al., where the LEE was seen in ^{95}Mo, the

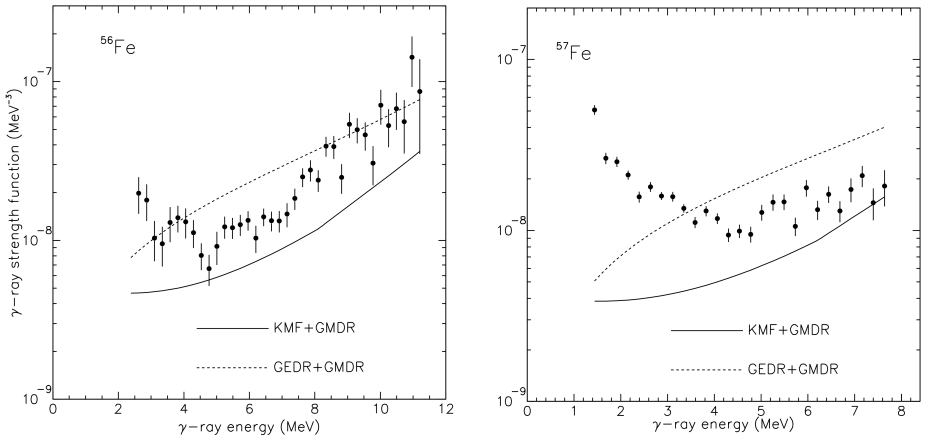

Figure 2.6: The GSFs of ^{56}Fe (left) and ^{57}Fe (right) from ^{57}Fe(^{3}He, ^{3}He$'\gamma$) and ^{57}Fe(^{3}He, $\alpha\gamma$) reactions at the Oslo Cyclotron Laboratory, calculated with the Oslo method. Low energy enhancements are seen as E_γ approaches zero. Kadmenskii-Markushev-Furman (KMF), Giant Magnetic Dipole Resonance (GMDR), and Giant Electric Dipole Resonance (GEDR) are different models of the GSF. Figures by E. Tavukcu [23].

wider community started to accept that the LEE is indeed a real physical phenomenon [25].

The origin of the LEE is still an unsolved mystery 20 years after its discovery. Angular distribution measurements of the gamma rays from a $(p, p'\gamma)^{56}$Fe experiment by Larsen et. al. show that the LEE is dominated by dipole transitions [26]. Measuring the electromagnetic character (E or M) of the gamma radiation has proved to be difficult experimentally with no clear conclusion today, however, an experiment by Jones et. al. shows a small bias towards magnetic character in the region of the enhancement [27].

While experimental findings are inconclusive, several studies using shell model calculations show that the LEE is caused by $M1$ transitions. Schwengner et. al. found that the LEEs in ^{90}Zr, ^{94,95,96}Mo are reproduced by their $M1$ shell model GSF, however, only $M1$ transitions were calculated with the shell model while the $E1$ GSF was estimated with the GLO expression [28]. In a study by K. Sieja, the $E1$ and $M1$ GSFs of ^{44}Sc were calculated with the shell model where Sieja found that the experimental LEE of ^{44}Sc was reproduced by $M1$ shell model calculations, and that $E1$ transitions had a very small contribution to the LEE [29]. In another study by Liddick et. al. both $E1$ and $M1$ transitions were calculated with KSHELL to study the LEE of ^{51}Ti [30].

To this day, few shell model calculations have been performed where $E1$ and $M1$ transitions are calculated in the same framework. If shell model calculations are to conclude that the LEE is indeed only caused by $M1$ transitions, then the calculations need to explicitly show that the $E1$ transitions are not contributing. Performing such calculations are computationally extremely heavy, and many such calculations were not possible just a few years ago but are feasible today. This is one of the main

motivations of this work, where I have performed very large calculations to study both $E1$ and $M1$ contributions of the LEE.

2.5 The nuclear shell model

2.5.1 Shells and orbitals

The *nuclear shell model* is a model of the atomic nucleus which inherits many key concepts from the successful *atomic* shell model (see for example sec. 2.5 in [12] and chap. 5.1 in [31]). The atomic shell model has been remarkable in explaining the behaviour and structure of the atom, thus tempting nuclear physicists to use a similar framework to explain how the nucleus works. In the nuclear shell model, protons and neutrons (collectively *nucleons*) are confined to a shell structure of orbitals which define the nucleons' angular momenta, their energies, and their parities. The orbitals are labelled nl_j where l denotes the orbital angular momentum of a nucleon in the given orbital and j denotes the total angular momentum of the same nucleon. In contrast to the atomic shell model, n is not the principal quantum number but simply a counter, counting the number of orbitals with a given l value. In the case of orbital splitting caused by spin-orbit coupling, n counts the number of orbitals with a given l and j value combination. We use spectroscopic notation to label the orbital angular momentum: $s, p, d, f, g, h, ...$ labels $l = 0, 1, 2, 3, 4, 5, ...$ respectively. In fig. 2.7 we see a diagram of the nuclear shell model structure for the lower laying orbitals. Note that the separations between the orbitals are only approximate and are for illustrative purposes. The ordering of the orbitals follows a Woods-Saxon potential [32], and the structure of the nucleus is assumed to be spherical. Note the cumulative occupation numbers at the large gaps between orbitals: $2, 8, 20, 28, 50$ (and $82, 126$). These numbers are the so called *magic numbers* and they indicate configurations of nucleons where the next free orbital is across a particularly large energy gap which is called a *major shell gap*. A nucleus with a magic proton or neutron number is referred to as a *magic nucleus* or simply just *magic*, while a nucleus with magic proton and neutron numbers are called *doubly magic*. Magic and doubly magic nuclei are often more stable than neighbouring nuclei. For example, ^{38}Ar is stable while ^{37}Ar and ^{39}Ar have half-lives of 35 days and 269 years, respectively. ^{51}V is stable while ^{52}V has a half-life of 3.7 minutes. On the contrary, ^{14}C has a half-life of 5700 years while ^{13}C and ^{12}C are stable. Magicity is a good rule of thumb, but it is not a hard rule[10]. A collection of orbitals between two major shell gaps is called a *major shell* and a particle excitation across one of these gaps is called an $\hbar\omega$ excitation. For example, the orbitals $1d_{5/2}, 2s_{1/2}, 1d_{3/2}$ constitute the sd major shell, while the orbitals $1f_{7/2}, 2p_{3/2}, 1f_{5/2}, 2p_{1/2}$ constitute the pf major shell. Excitation of a nucleon from one of the sd orbitals to one of the pf orbitals is an $\hbar\omega$ excitation.

The ordering and the separations of the orbitals in fig. 2.7 is not the same for all nuclei. Deformation of the nucleus changes the ordering of the

[10] One should always consult the sacred texts at nndc.bnl.gov/nudat3/

orbitals and introduces new orbital splittings, akin to the splitting introduced by the spin-orbit coupling which we see in the figure. In this thesis I assume no intrinsic deformation, thus assuming the shell structure of fig. 2.7. These assumptions certainly put constraints on which nuclei we are able to accurately perform shell model calculations on since most atomic nuclei are not perfectly spherical.

The shell structure itself emerges from the fact that both protons and neutrons are fermions; they must obey the Pauli exclusion principle, meaning that no two protons and no two neutrons are allowed to occupy the same quantum state. For example, a proton might be located in the $1s_{1/2}$ orbital. The proton has an orbital angular momentum of $l = 0$, a spin of $s = 1/2$, and these two angular momentum vectors can couple to produce a total angular momentum of $j = 1/2$. In this special case of $l = 0$ the spin and orbital angular momentum cannot "negatively couple" to $j = -1/2$ because the magnitude of any of the angular momentum vectors (or vectors in general) cannot be negative[11]. This is a special case only for the $1s$ orbital. Now comes along another proton which wants to conform to the same shell structure. Both protons are allowed to stay in the $1s_{1/2}$ orbital because they can have different j_z values and hence not occupy the same quantum state. Remember that $j_z = j, j-1, ..., -j$ meaning that the two protons may have $j_z = \pm 1/2$. A third proton however, is not allowed to stay in $1s_{1/2}$ because there are no more distinct quantum states. The third proton will have to take residence in $1p_{3/2}$ which has room for a total of four protons. The maximum amount of allowed protons (or neutrons) in an orbital is called the *maximum occupation number* or the *degeneracy* of the orbital. The $1p_{3/2}$ orbital has a degeneracy of four since there are four distinct states, identified by their j_z values, which correspond to the same energy level. In fig. 2.7 we see that spin-orbit coupling lifts the j degeneracy of the orbitals, as indicated by the transition from the left to the right column of lines. There are other situations where degeneracy is lifted further, as with deformed nuclei described by the *Nilsson model* and rotating nuclei described by the *Cranking model* [33]. As mentioned, in this work I assume a spherical nucleus.

Subsequent protons will occupy higher and higher laying orbitals as the maximum occupancy of each orbital is reached, and neutrons occupy an identical but separate shell structure following the same rules. Of particular interest is which j_z values the nucleons prefer to take. It is shown experimentally that in the ground state, two protons (or neutrons) prefer to pair together with opposite j_z values, meaning that a pair will have $j_z = \pm 1/2, \pm 3/2, \pm 5/2, ...$ depending on what orbital the pair occupies and the number of protons already present in that orbital. A profound consequence of this pairing is that the ground state of *any* nucleus with an even number of protons and an even number of neutrons – an even-even nucleus – is always $j^\pi = 0^+$. Every pair of nucleons will zero out each other's angular momentum and since they are pairwise located in the same orbital,

[11] Or more correctly, the total angular momentum descending ladder operator operating on $|j = 1/2\rangle$ gives the zero state: $\hat{a}_-|j = 1/2\rangle = |0\rangle$.

m_i						m		
5/2	3/2	1/2	-1/2	-3/2	-5/2			
•	•					4		
•		•				3		
•			•			2		
•				•		1		
•					•	0		
	•	•					2	
	•		•				1	
	•			•			0	
	•				•		-1	
		•	•					0
		•		•		-1		
		•			•	-2		
			•	•			-2	
			•		•	-3		
				•	•	-4		
					j	4	2	0

Table 2.1: m-scheme of two identical nucleons occupying a $j = 5/2$ orbital. $m = m_1 + m_2$ is the sum of the z components of $j_i, i = 1, 2$. The black dots indicate which m_i states are occupied by a nucleon, and the last column indicates the sum of each pair of occupied states. The bottom row tells us which total angular momentum j the different values m might belong to.

the parity will always be positive since $1^2 = (-1)^2 = 1$. Another equally important result of the pairing effect is the fact that the ground state of a nucleus where all nucleons are paired save for one, has its j^π decided by the unpaired nucleon alone. Take ${}^{51}_{23}\mathrm{V}_{28}$ as an example. It has 28 neutrons meaning that all of the neutrons are paired up, filling up to and including the $1f_{7/2}$ orbital and contributes to the total by 0^+. There are however 23 protons, filling all orbitals up to and including $1d_{3/2}$, with one pair and one non-paired proton in $1f_{7/2}$. We would therefore expect that the ground state of ${}^{51}\mathrm{V}$ is $j^\pi = 7/2^-$ and that is indeed the case [34]. Conversely, the case for odd-odd nuclei is not as straight forward. Odd-odd nuclei have a non-paired proton and a non-paired neutron whose angular momenta do not couple in such a predictable manner. Consider the case of ${}^{50}\mathrm{V}$ whose two non-paired nucleons are one proton and one neutron which both reside in the $1f_{7/2}$ orbital. If these nucleons were both protons or both neutrons they would couple to $j^\pi = 0^+$, but the ground state of ${}^{50}\mathrm{V}$ is experimentally verified to be $j^\pi = 6^+$ [35].

2.5.2 The m-scheme

In table 2.1 we see all the possible total angular momentum couplings for two identical nucleons occupying a $j = 5/2$ orbital (for example $1d_{5/2}$). Here m_i is the z component of j for the ith particle, while $m = m_1 + m_2$ is the sum of the z components of j for both nucleons. Since the two nucleons are identical

fermions, they are prohibited by Pauli's exclusion principle to have $m_1 = m_2$. This can be seen from the requirement that the wave function describing a system of fermions must be anti-symmetric with respect to exchange of two of the fermions in the system. This means that if the space and spin coordinates of two identical fermions are switched, the total wave function changes its sign, namely that

$$\psi(\mathbf{x}_1, \mathbf{x}_2) = -\psi(\mathbf{x}_2, \mathbf{x}_1), \tag{2.50}$$

which implies that

$$\psi(\mathbf{x}, \mathbf{x}) = 0. \tag{2.51}$$

Here, $\mathbf{x}_i$ contains the space and angular momentum coordinates for the ith nucleon. We can more specifically say that two identical nucleons with total angular momentum j_1 and j_2, as well as total angular momentum z components of m_1 and m_2 respectively, couple to total angular momentum j and z component m by

$$\psi(j_1,j_2,j,m) = \sum_{m_1 m_2} \langle j_1\, m_1\, j_2\, m_2 | j\, m\rangle \left(\phi_{j_1 m_1}(x_1)\phi_{j_2 m_2}(x_2) - \phi_{j_1 m_1}(x_2)\phi_{j_2 m_2}(x_1)\right). \tag{2.52}$$

Here, $\phi_{j_n m_n}$ represents a fermion particle state of total angular momentum j_n and projection m_n. We see that the wave function vanishes if $j_1 = j_2$ and $m_1 = m_2$, or if $x_1 = x_2$. We also see that interchanging x_1 and x_2 produces the same wave function, but with the sign swapped. This means that swapping the position and spin coordinates does not produce a new distinct entry in table 2.1, since a swapped sign in front of the wave function will disappear when calculating any expectation value, namely that

$$\langle\psi|\hat{O}|\psi\rangle = \langle -\psi|\hat{O}|-\psi\rangle \tag{2.53}$$

where $\hat{O}$ represents the operator of any observable. Take now $m = 0$ as an example. According to table 2.1 there are three different combinations which produce $m = 0$. We then say that the m-scheme dimensionality for $m = 0$ is 3. The m-scheme dimensionality is a measure of two important qualities of numerical shell model calculations; it reveals what results are possible to extract from the calculations and the computational requirements of the calculations. Both of these qualities will be explored in the subsequent sections.

2.5.3 Shell model calculations in the m-scheme basis

In shell model calculations using the m-scheme basis, a wave function is represented as a linear combination of m-scheme basis states, namely

$$|\psi\rangle = \sum_{i=1}^{D_m} v_i |m_i\rangle, \tag{2.54}$$

where D_m – the m-scheme dimension – is the number of m-scheme basis states $|m_i\rangle$. The m-scheme basis states are themselves Slater determinants, each representing a certain configuration of nucleons. The basis states are denoted in second quantisation formalism as

$$|m_i\rangle = \left(\prod_{j=1}^{A} c^{\dagger}_{a_{i,j}} \right) |0\rangle. \tag{2.55}$$

The creation operator $c^{\dagger}_{a_{i,j}}$ creates a single particle state $a_{i,j}$ for the jth nucleon of the ith m-scheme basis state. There are A nucleons in each basis state which together constitute some configuration of orbital occupation. The m in $|m_i\rangle$ indicates that the basis states have some total angular momentum z component m_i. For even-mass nuclei, the subspace of $m = 0$ basis states is sufficient to describe wave functions of any j while for odd-mass nuclei the subspace of $m = 1/2$ is sufficient [1].

2.5.4 Interactions and model spaces

In shell model calculations there are potentially an enormous amount of different configurations which all have the same m value making D_m very large and thus making eq. (2.54) computationally heavy. The size of D_m boils down to a combinatorics problem defined by the number of nucleons and the number of orbitals in which the nucleons may reside. By reducing the number of possible configurations, we can reduce the number of basis states thus making the calculations of the shell model wave functions easier. Such a reduction can be done either by reducing the number of nucleons or reducing the number of orbitals.

In eq. (2.55) we see A creation operators operating on the vacuum state $|0\rangle$. When an excitation occurs, all A nucleons can theoretically partake in the excitation, but in reality most of the "work" is performed by the outer laying nucleons due to the fact that they are closer to the Fermi surface than the inner nucleons. We can exploit this fact to reduce the computational complexity of the model by using an *inert core* of nucleons instead of the vacuum state. Instead of letting the nucleons all be free to roam, we lock some of them in place and model them by a stationary *mean field potential*. The inert core behaves to the outer *valence* nucleons as the entire nucleus behaves to the electrons in atomic physics. The size of D_m is reduced because we do not need to separately treat each of the nucleons in the inert core, thus reducing the number of possible configurations.

In fig. 2.7 we see a few of the lower laying orbitals of the shell model, while in reality there are many more. In shell model calculations we reduce the size of D_m by restricting the number of orbitals available for the valence nucleons. We might for example only allow valence nucleons to use the *sd* major shell, removing all higher laying orbitals. We then refer to *sd* as the *model space* of the shell model calculation.

A choice of inert core and model space are two of the ingredients in an *interaction*. On the left side of fig. 2.7 we see all the interactions used in

this work[12]. The coloured lines indicate which orbitals are included in the different interactions, while on the right side next to the magic numbers we see the inert cores used for the different interactions. USD, SDPF-MU, and SDPF-SDG use ^{16}O as an inert core, GXPF uses ^{40}Ca, while JUN45 uses ^{56}Ni. Using a doubly magic nucleus is the obvious choice for an inert core because they are particularly stable and thus less likely to have to be included in an excitation.

One important aspect of choosing a suitable interaction is the parity of the levels. As an example, we might model ^{50}V in the GXPF interaction which is a suitable choice when considering the computational cost, since GXPF has a relatively small model space compared to, for example, SDPF-MU. Since the pf major shell only has negative parity orbitals and ^{50}V has 10 valence nucleons in pf, we can only get positive parity levels from this model. This in turn means that we will not be able to extract odd numbered E transitions from the model ($E1$ might be of great interest!). Conversely, if we use the SDPF-MU interaction we have both pf and sd major shells, which are of both negative and positive parities. We will thus be able to extract all possible transitions from the model!

In table A.1 we see an overview over the interactions used in this work. The table includes the range of possible isotopes within the model space, which model space is used, the inert core, and the recommended g spin factors. Note that an interaction may not be well suited for every isotope within its range. For example, calculating ^{17}O with the USDA interaction will not yield good results because there is only one free valence neutron. In other words, the m-scheme dimensionality is too low to accurately represent the different nucleon configurations of ^{17}O. As for ^{39}Ca with the USDA interaction, there is only one free hole which greatly restricts the possible excitations and in turn yields a very small m-scheme dimensionality. Note that gs8 and GCLSTsdpfsdgix5pn use the same model space and have the same g_s value. The two-body matrix elements in the two interactions are identical, but the single-particle energies in gs8 are tuned to better reproduce experimental data around ^{58}Ni [36]. I will therefore use GCLSTsdpfsdgix5pn for the scandium calculations and gs8 for the zinc calculations. GXPF denotes the three interactions GXPF1, GXPF1A, and GXPF1B. GXPF1A is the revised version of GXPF1 by Honma et al. [37] and is the one of the two that I use in this work. USD denotes three interactions, namely USD, USDA and USDB. These three interactions will not be used in this work, but is included in the overview because they are among the most widely used interactions. SDPF-MU is a combination of USD and GXPF1B [38] which means that it spans two major shells. SDPF-MU can therefore deliver levels of both positive and negative parities for odd and even nuclei, which in turn means that we can get both $E1$ and $M1$ transitions from any nucleus in its model space.

[12] SDPF-SDG is not really an interaction but a model space. The interactions gs8 and GCLSTsdpfsdgix5pn are the two interactions in SDPF-SDG used in this work.

2.5.5 Truncation

The size of D_m is greatly reduced by lowering the number of valence nucleons and restricting the number of orbitals. Still, the size of D_m might be too large to be handled by even the most powerful computers today. To reduce the size of D_m even further we might perform particle-hole truncations and $\hbar\omega$ truncations. In particle-hole truncations we restrict the maximum and minimum number of nucleons allowed in any of the orbitals of the model space, thus reducing the number of possible configurations. For interactions whose model spaces span two or more major shells, like SDPF-MU and SDPF-SDG, we might limit the number of nucleons which are allowed to be excited across a major shell gap. Such a limitation is called an $\hbar\omega$ truncation and it often has a large impact on D_m.

Take ^{64}Zn in the SDPF-SDG model space as an example in which ^{16}O is the core and there are 22 and 26 valence protons and neutrons respectively. The $m = 0$ m-scheme dimension is so large that a regular computer isn't even able to count the number of configurations[13]; we have to truncate the model to be able to use it! By setting a $1\hbar\omega$ truncation, the dimension reduces to $D_m \approx 4.81 \times 10^{10}$ which is at the very upper limit of what is possible with today's computers[14]. We can reduce D_m further by performing a particle-hole truncation. If we set the minimum number of nucleons (protons and neutrons combined) in the $f_{7/2}$ orbitals to 14, the dimensionality is reduced to $D_m \approx 1.59 \times 10^8$ which is well within the reach of a modern supercomputer. Which orbitals to truncate depends entirely on the physics of the problem; some orbitals have a larger impact on the results than other orbitals and identifying which ones to truncate is a game of (educated) trial and error.

[13] Using the dimensionality calculator which comes with KSHELL.

[14] The D_m listed here is the m-scheme dimension of the negative parity states, while for the positive parity states $D_m \approx 5.01 \times 10^8$.

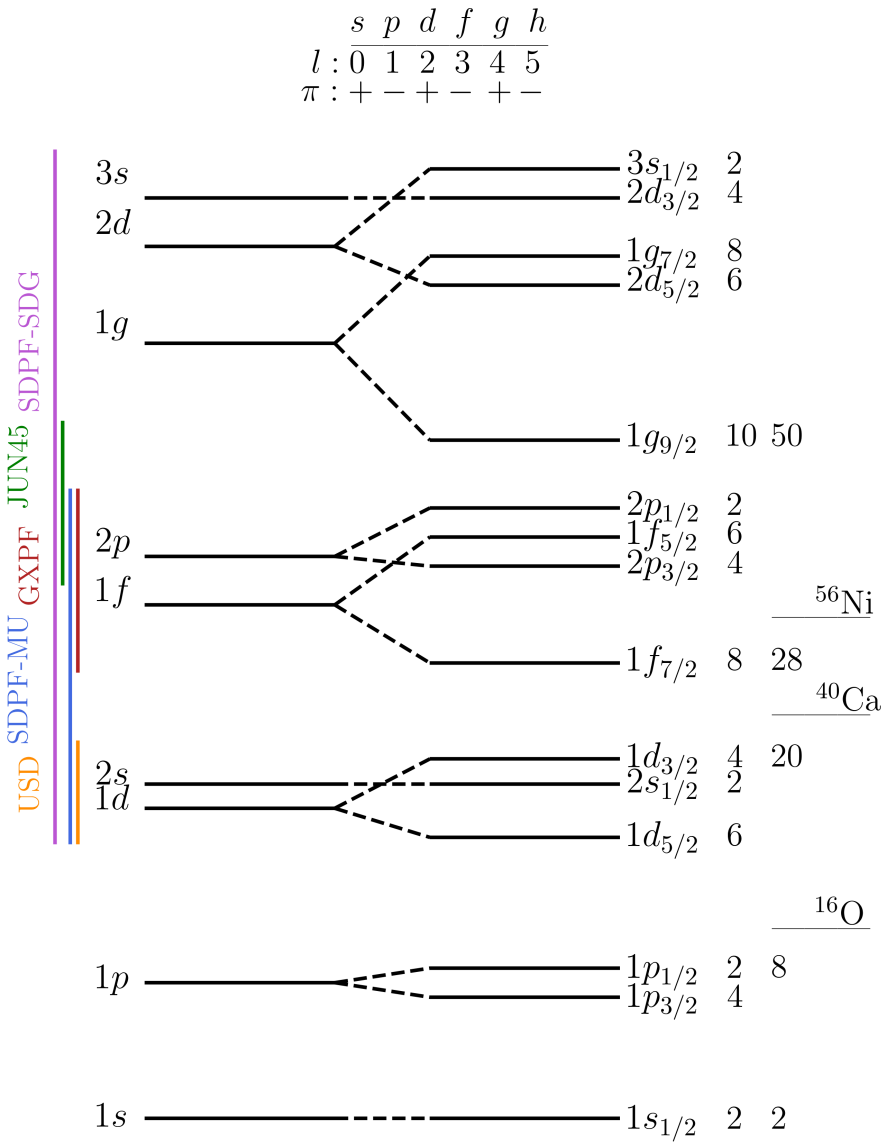

Figure 2.7: The shell structure of the nuclear shell model. The splitting of the orbitals due to spin-orbit coupling is shown in the right column of lines, connected to their un-split counterparts with dashed lines. The occupation number for each orbital is indicated to the right of each orbital, with the cumulative occupation number at the magic number gaps next to it. The model space of a selection of interactions are indicated on the left side, while the corresponding (inert) cores are indicated to the far right. A legend of the spectroscopic notation with the corresponding orbital angular momenta and parities is located at the top of the figure. Note that the separation between the orbitals is only approximate.

Chapter 3

Experimental

3.1 KSHELL

KSHELL is a numerical nuclear shell model solver developed by Shimizu et. al. [1]. It is a massively parallelisable program which uses the thick-restart block Lanczos method to extract energy eigenvalues of shell model hamiltonians. KSHELL supports extremely large m-scheme dimensions (see section 2.5.2) of up to tens of billions, given that the computer has enough processing power and enough memory. KSHELL can be run in j-projection mode which enables the user to request a desired amount of levels per j^π. m-projection mode is also available where the user can simply request N levels, and KSHELL will deliver the N lowest lying levels.

While KSHELL is coded in Fortran, a user interface `kshell_ui` programmed in Python is used to generate the correct input files for the Fortran code. `kshell_ui` is authored by Noritaka Shimizu and quite heavily modified by me to suit the needs of my masters thesis. Following are the most notable changes I have made.

The program is updated to Python 3.8[1] from 2.7, and I have added extensive type hinting and documentation strings to more or less all functions and variables. I did this mainly to get a better understanding on how KSHELL thinks, since `kshell_ui` produces the "food" for KSHELL. While some people prefer dense maths to understand a concept, and others well worded descriptions, I prefer looking at computer code to understand how something works. Of other notable changes to `kshell_ui`, I have added functionality for requesting ranges of j^π levels instead of having to manually input the number of levels for each j^π. I have added a check which tests if the model space can deliver the user requested amount of levels, alerts the user if too many levels have been requested and if so, adjusts the number of requested levels to the highest number of levels supported by that interaction. I have also changed the user interface to prompt the user for estimated time usage, number of MPI processes, number of OpenMP threads, and an option to force simultaneous multithreading which KSHELL benefits from. All of these parameters are commands to the supercomputer queue system (Slurm in the case of Betzy) and are added to the start of the KSHELL run script.

[1] Compatible with 3.9, 3.10 and probably many future releases.

Another quite important feature I have implemented is the possibility to split up the calculations into separate shell executables. By default, `kshell_ui` generates a single executable file with all the commands needed to generate the user requested data. While this is good for smaller calculations, it is impractical for large calculations which may take hours or days on large supercomputers. My implemented feature puts the calculation for each j^π in a separate executable with the correct supercomputer queue commands in each file. Transition calculations are also put in separate executables, one for each $j_i^{\pi_i} \rightarrow j_f^{\pi_f}$. Now each file may be queued separately which greatly reduces the problem of estimating computation time. Simply run one of the executables with a generous time estimate[2], see how long that takes and then extrapolate the time usage to the other executables. While the time is much easier to estimate, another problem has emerged. When splitting the calculations into separate executables, quite a few executables have been generated, probably a few tens or up to a hundred. Queuing all of these executables can be a hassle, and in addition, you might want to change the number of nodes or the estimated time usage for each of the executables. I have solved this problem too, and that code is a part of the `kshell-utilities` package I have developed which I will speak more about in section 3.2.

I have done some minor changes to how the Fortran code writes data to file. The reduced transition probabilities are written with greater decimal precision because some very weak transitions were not registered at all; the transitions were simply rounded to 0. Also, the structure of how data is written to file has been greatly improved to make the process of reading the files much easier.

The KSHELL code along with the user interface is available at github.com/GaffaSnobb/kshell.

3.2 kshell-utilities

For this masters thesis I have developed a Python package called `kshell-utilities` which contains many useful tools for handling data generated by KSHELL. Some of the tools are built upon code developed by Jørgen Midtbø [39] and Noritaka Shimizu [1] while most of the code is developed from scratch by me. `kshell-utilities` is built with Python, is open source, and is available to anyone with an internet connection. The package may be installed by `pip install kshell-utilities` for the latest stable version, or directly from the source code for the latest version [40]. Following are the main features of `kshell-utilities`. Note that the software is still in development, so please see the GitHub repositories for the very latest instructions. All code is available at github.com/GaffaSnobb/kshell-utilities.

[2] A generous time estimate is now much more approachable since the run time for each individual executable is much lower than the total time for all the executables.

3.2.1 Handling KSHELL executables

When splitting a calculation in several executables with `kshell_ui` you are stuck with several tens of executables. `edit_and_queue_executables` is a function which lets you edit the number of nodes, the time estimate, and the job name of all the executables without having to open each file separately in an editor. The script also has an option for queueing the executables on the fly after they have been edited[3]. Open an interactive Python session in the directory where all the executables are located and run the function. Choose the parameters you want to edit:

```
>>> import kshell_utilities as ksutil
>>> ksutil.edit_and_queue_executables()
Please choose parameters you want to alter (y/n) (default n):
nodes: y
seconds: y
minutes: y
hours: y
days: y
job_name: y
queue: y

```

The script will then loop over all executables in the directory and prompt you for new parameter values. After the values have been entered, the script will queue the executable:

```
Edit 000_1p.sh? (y/n) (default y):
Loading 000_1p.sh
Job name: 1p
Number of nodes: 8
Number of seconds: 0
Number of minutes: 10
Number of hours: 0
Number of days: 0
Submitted batch job

Edit 001_3p.sh? (y/n) (default y):
...

```

The script will continue to prompt for all the executables in the directory. This process is much less time consuming than having to individually open each executable, edit it, and then put it in the queue.

3.2.2 Reading data from KSHELL

KSHELL typically produces a summary text file containing all level and transit information. This summary file can easily be read by the `loadtxt` function:

```
>>> import kshell_utilities as ksutil
>>> res = ksutil.loadtxt("<path-to-summary-file>")[0]

```

[3] Currently hard-coded for Slurm, the queue system on Betzy.

`res` is now an object containing a magnitude of useful data, most notably level information (columns of $E, 2j, \pi, N$):

```
>>> res.levels
array([[-40.467,   0.   ,   1.   ,   1.   ],
       [-38.771,   4.   ,   1.   ,   1.   ],
       [-33.919,   0.   ,   1.   ,   2.   ],
       ...,
       [-22.904,   0.   ,   1.   ,   8.   ],
       [-22.468,   0.   ,   1.   ,   9.   ],
       [-21.905,   0.   ,   1.   ,  10.   ]])

```

and transition information (columns of $2j_i, \pi_i, N_i, E_i, 2j_f, \pi_f, N_f, E_f, E_\gamma, B(..., i \to f), B(..., f \to i)$):

```
>>> res.transitions_BM1
array([[4, 1, 2, ..., 5.889, 1.4183e-04, 1.4183e-04],
       [4, 1, 3, ..., 8.281, 4.8164604e-01, 4.8164604e-01],
       [4, 1, 3, ..., 2.392, 1.1044075e+00, 1.1044075e+00],
       ...,
       [0, 1, 10, ..., 3.037, 1.427484e-02, 4.75828e-03],
       [0, 1, 10, ..., 2.531, 9.08819e-03, 3.0294e-03],
       [0, 1, 10, ..., 1.355, 7.174e-04, 2.3913e-04]])

```

The desired data can easily be sliced to the users needs.

When a summary file is loaded with `loadtxt`, all the data is saved to `.npy` files and stored in `tmp/` located in the same directory as the script you are calling `loadtxt` from. Loading NumPy files is very fast, almost instant, regardless of the size of the file while loading data from the summary text file might take up to a couple of minutes for very large summary files. A SHA hash generated from the accompanying KSHELL executables is used for the filenames of the temporary NumPy files so that tmp files from different KSHELL calculations aren't mixed. Please be sure to keep the KSHELL executable(s) in the same directory as the summary file for this functionality to work properly.

When splitting the KSHELL calculations into separate executables, as explained in section 3.1 and section 3.2.1, the summary file is not generated automatically. Use `collect_logs` to gather information from all of the separate KSHELL log files and compile them into a summary file:

```
>>> ksutil.collect_logs("<path-to-dir-with-logs>")
Loading energy log files...
Reading file   1 of 9
Reading file   2 of 9
...

Loading transit log files...
Reading file   1 of 23, multipole: E1
Reading file   2 of 23, multipole: E1
...

```

After completion, a summary file will be located in the same directory as the log files. Read the summary with the aforementioned `loadtxt`.

3.2.3 Visualising data from KSHELL

Two notable pieces of nuclear properties are the level density (NLD) and the gamma strength function (GSF). Code for calculating these properties are embedded in `res` as methods. You can easily generate the NLD and GSF by

```
res.nld()
res.gsf()

```

which produces the following plots using default values

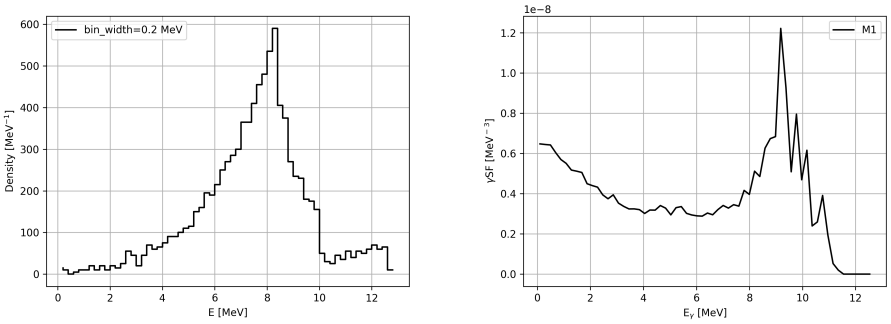

The GSF calculation supports a myriad of parameters, most notably

```
def gsf(self,
    bin_width,
    Ex_min,
    Ex_max,
    multipole_type,
    partial_or_total,
    include_n_states,
    filter_spins,
    filter_parities,
    return_n_transitions
):

```

`bin_width` is the width of the energy bins for the GSF, with the default value of 200 keV. `Ex_min` and `Ex_max` are the lower and upper limits for which initial energy levels to include in the calculations. The min value is typically 2 to 3 MeV to make sure that the GSF calculations are taken above the discrete region, while the max value is typically set to the neutron separation energy of the nucleus in question. `multipole_type` sets the multipolarity of the transitions so that the correct data set is chosen with the correct pre-factor to the GSF (see eq. (2.43)). Allowed values are `E1`, `M1`, `E2`. With `partial_or_total` you can choose whether to use the *partial* or *total* level density when calculating the GSF. Note that using the total level density is wrong and is included only for comparison with using the partial level density. `filter_spins` lets you choose a subset of the available j values in the data set, while `filter_parities` lets you choose what parity you want. Finally, `return_n_transitions = True` makes the GSF function return an additional array containing the number of transitions used to calculate the

GSF for each E_γ. This is used to study the Porter-Thomas fluctuation of the GSF.

`level_plot` is a useful function for visualising level spacing. It supports selection of a subset of levels and angular momenta:

```
>>> res.level_plot()
>>> res.level_plot(include_n_levels=10, filter_spins=[0, 2, 8])

```

produces:

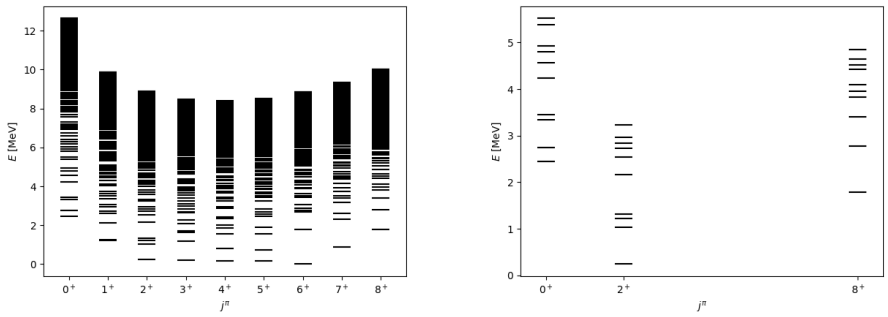

Analysing the distribution of B values is available, based on selections of both angular momentum and excitation energy. Such analyses are easily performed by the following code:

```
>>> res.porter_thomas_Ei_plot(
    Ei_range_min = 5,
    Ei_range_max = 9,
    Ei_values = np.linspace(5, 9, 3),
    Ei_bin_width = 0.2,
    BXL_bin_width = 0.1,
    multipole_type = "M1",
)
>>> res.porter_thomas_j_plot(
    Ex_min = 5,
    Ex_max = 9,
    j_lists = [[0, 1, 2], [3, 4, 5], [6, 7, 8]],
    BXL_bin_width = 0.1,
    multipole_type = "M1",
    include_relative_difference = True,
)

```

which produces the following figures:

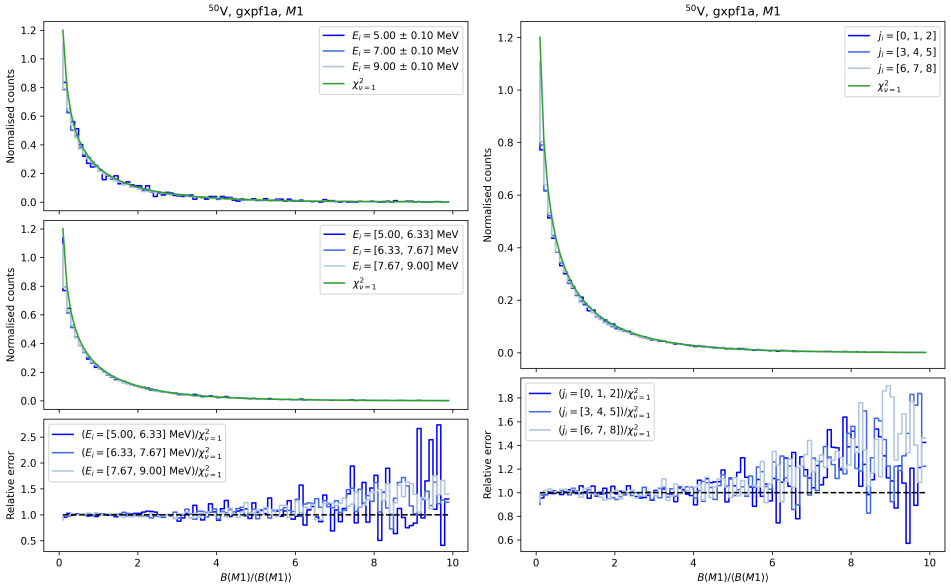

The listed function arguments are the default values, so no user input is actually needed to produce these figures. The E_i analysis plots the distributions of B values from three selections of excitation energies (within the specified E_i bin size) in addition to three larger ranges of excitation energies. All distributions are scaled to match the height of the Porter-Thomas distribution which is plotted along with the B distributions. The j_i analysis plots the distribution of B values from three selections of angular momentum, also scaled to match the height of the Porter-Thomas distribution. Relative differences between the B distributions and the Porter-Thomas distribution are also displayed to better discern the details.

The B distribution plots are supplemental tools for studying the validity of the generalised Brink-Axel hypothesis. `kshell-utilities` has built-in tools for studying the angular momentum dependence / independence of the GSF for the given KSHELL calculations. The commands

```
>>> res.brink_axel_j(
    bin_width = 0.2,
    Ex_min = 5,
    Ex_max = 10,
    multipole_type = "M1",
    j_list = range(8+1)
)
>>> res.brink_axel_j(
    bin_width = 0.2,
    Ex_min = 5,
    Ex_max = 10,
    multipole_type = "M1",
    j_list = [2]
)

```

produce figures where the GSF is calculated individually for every angular momentum in `j_list` (grey) and compared to the "total" GSF averaged over all angular momenta (black). If no `j_list` is given, then every available angular momentum will be used. Note that the total GSF is calculated using

all available angular momenta regardless of the choice of `j_list`, meaning that the single angular momentum GSF will not be equal to the total GSF if only a single angular momentum is chosen. This is illustrated in the figures below which are produced by the aforementioned commands:

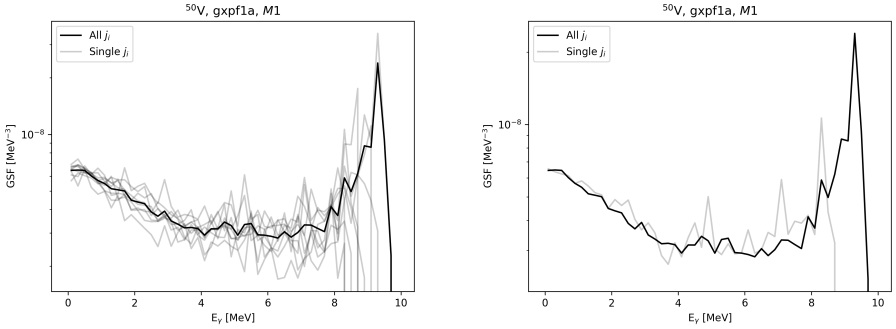

When studying the individual angular momentum GSFs, it is fruitful to consider the NLD as a function of both excitation energy and angular momentum. The commands

```
>>> res.angular_momentum_distribution_plot(
    bin_width = 0.4,
    E_min = 5,
    E_max = 10,
    j_list = range(8+1),
    filter_parity = "+",
)

```

produce the following heatmap of level densities for all the angular momenta in `j_list`:

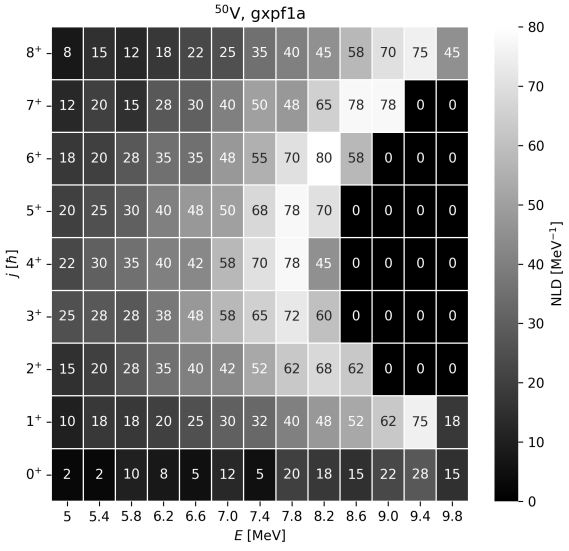

All available angular momenta are used if no `j_list` is given. If no parity

is given, both will be used.

A final note for the functionality demonstrated in this section. All functions have default values, so the user does not actually have to specify any function arguments. It is therefore very easy and quick to generate a rough sketch for the user's needs!

3.3 Betzy

Betzy is a supercomputer located at NTNU in Trondheim and hosted by Sigma2/NRIS, named after Elizabeth Stephansen, the first Norwegian woman to be awarded a doctorate degree[4]. Betzy is the most powerful supercomputer in Norway and consists of 1344 compute nodes, each equipped with two 64 core AMD Epyc 7742 CPUs giving 128 cores per node and a total of 172032 cores. The high core count makes Betzy particularly suitable for KSHELL with KSHELL being a massively parallel program. Most of the calculations in this work would not be possible with a supercomputer with a lower core count.

While Betzy does have 1344 compute nodes in total, it is not realistic to be able to use all of them at once. Betzy has many users and there are always some nodes in use. In addition, using more nodes (more CPU cores) does not always benefit KSHELL calculations. In particular, the m-scheme dimension sets an upper limit to how may CPU cores can be used. If the m-scheme dimension is too small compared to the amount of CPU cores, then the data will not be effectively distributed in parallel to the cores. In this work I have mostly used 64 nodes due to shorter queue times, but I also tested 128 and 256 nodes with good results.

With my implementation of the splitting of executables, as explained in section 3.1, up to 64 nodes per job has been sufficient for even the largest calculations. On Betzy, simultaneous multithreading (SMT)[5] is deactivated by default since most scientific applications do not benefit from it. I performed a few benchmarks to see if this is true for KSHELL, and it turns out that KSHELL does benefit from SMT. In fig. 3.1 we see the time usage of a KSHELL calculation on Betzy. The calculation was run for both 128 physical cores and 256 virtual cores (SMT) per node. We can see from the figure that using SMT yields a bit more than a 20% reduction in time when using a single node, and a bit less than 20% when using 4 nodes. It seems that KSHELL does benefit from using SMT, and I have therefore implemented an option in `kshell_ui.py` for activating SMT by inserting the correct parameters to Slurm – the queue system on Betzy – to bypass the SMT limitations on Betzy.

Even though each job might not be suitable for a very large number of nodes, each job can be run in parallel to each other. The maximum computational resources used at the same time for this work was 38 jobs each using 16 nodes, totalling 608 nodes or 77824 CPU cores (155648 virtual cores since SMT was used). That is almost half of all the nodes on Betzy –

[4] en.wikipedia.org/wiki/Elizabeth_Stephansen
[5] en.wikipedia.org/wiki/Simultaneous_multithreading

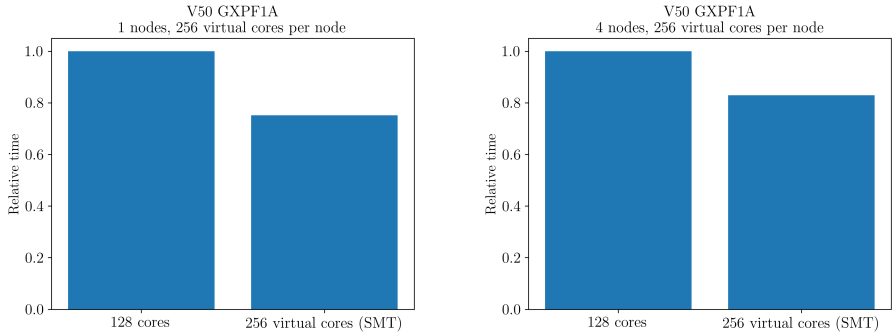

Figure 3.1: Time usage of a KSHELL calculation on Betzy when using 128 physical cores and 256 virtual cores (simultaneous multithreading). Left: 1 node. Right: 4 nodes.

the most powerful computer in Norway – used at the same time to perform calculations for this work! Marvellous!

Chapter 4

Results and discussion

4.1 Brink-Axel hypothesis and Porter-Thomas fluctuations

The central theme of this thesis is using the gamma strength function (GSF) as a tool to measure how certain scandium and vanadium isotopes prefer to gamma decay. Since the GSF is in principle a function of four variables, $E_\gamma, E_i, j_i, \pi_i$, it is tempting to simplify the interpretation and visualisation of the data by averaging over all parameters except E_γ, leaving the GSF solely as a function of gamma energy. By performing said average I assume that the generalised Brink-Axel (gBA) hypothesis holds, or in other words that

$$f(E_\gamma) \approx f(E_\gamma, E_i, j_i, \pi_i). \tag{4.1}$$

The gBA hypothesis does not hold for all nuclei under all circumstances (see section 2.4.3 for examples) which is why I start my analysis by testing that gBA hypothesis indeed holds for the calculations I have performed.

In fig. 4.1 we see the $M1$ (top) and $E1$ (bottom) GSFs of ^{44}Sc where $f(E_\gamma)$ is shown in black and $f(E_\gamma, j_i)$ for $j_i = 0, 1, ..., 8$ is shown in grey. All the individual j_i GSFs fluctuate neatly around their average in the gamma energy range $E_\gamma = [0, 6]$ MeV and they are, as expected, not perfectly identical[1]. At gamma energies above 6 MeV, larger fluctuations start to appear for both $M1$ and $E1$ transitions.

[1] Because lifetimes – and hence B values – are inherently statistical of nature, see section 2.4.3.

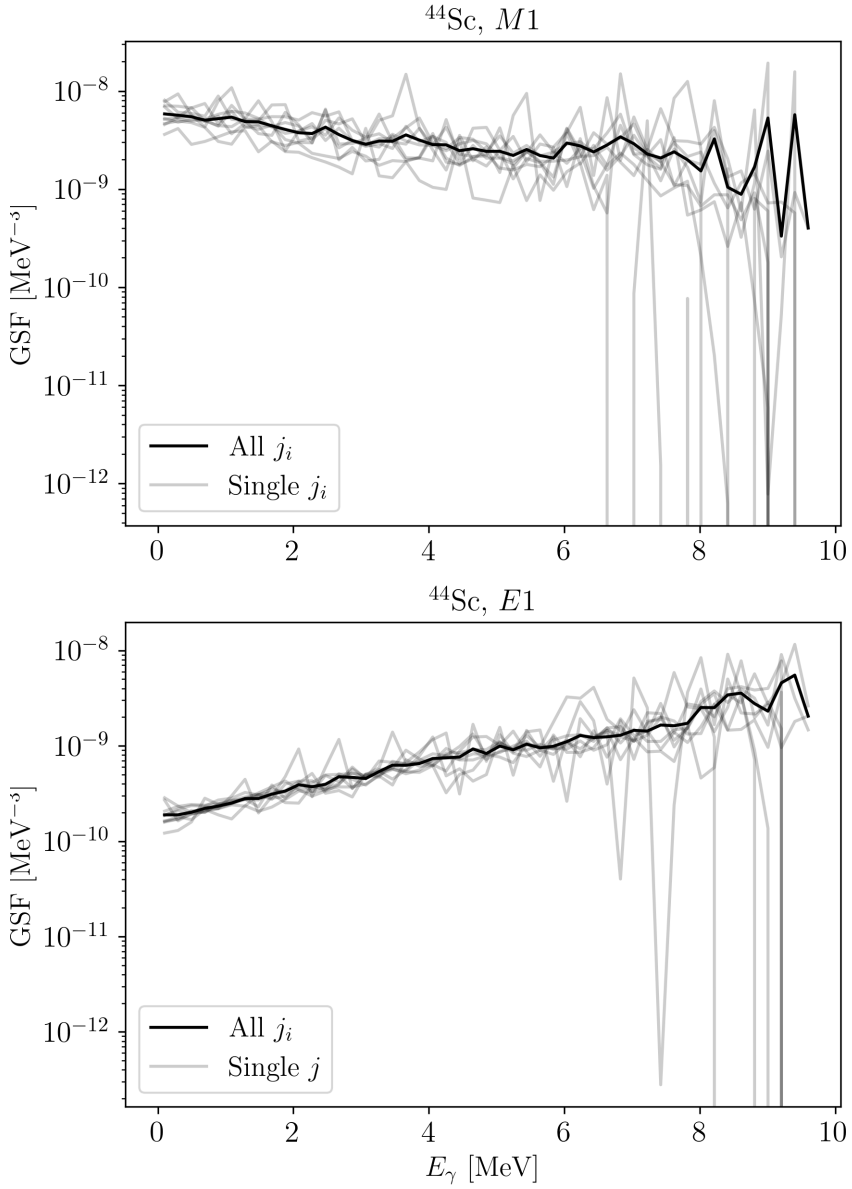

Figure 4.1: The GSF of ^{44}Sc using the GCLSTsdpfsdgix5pn interaction with a $3\hbar\omega$ truncation and 200 levels for each angular momentum $j_i = 0, 1, ..., 8$ for both parities. The GSF for each individual j_i is shown in grey and their average is shown in black. Top: the $M1$ GSFs. Bottom: the $E1$ GSFs.

While not a rigorous mathematical proof, the GSFs in fig. 4.1 all follow the same trend, pointing to that the gBA hypothesis is indeed applicable. Even the large fluctuations above $E_\gamma = 6$ MeV does not necessarily disprove gBA, because fluctuations of that size may be statistically expected if a low number of B values was used to generate the GSFs in that E_γ region. This is indeed true, and is explored thoroughly in section 4.2.

Recall that we expect the B values to have a statistical distribution, namely that

$$\frac{B(Xj_\gamma)}{\langle B(Xj_\gamma)\rangle} \sim \chi^2_1, \tag{4.2}$$

a distribution which is also called the Porter-Thomas distribution. In the two top plots of fig. 4.2 we see for ^{44}Sc the distribution of $B(E1)$ values on the left and $B(M1)$ on the right. All B values corresponding to $E_i < 5$ MeV have been removed to exclude levels in the discrete region and all B values corresponding to $E_i > 9.7$ MeV have been removed because they are above the neutron separation energy. Three selections of B values have been made which are $j_i = \{0, 1, 2\}$, $j_i = \{3, 4, 5\}$ and $j_i = \{6, 7, 8\}$, and the Porter-Thomas distribution is shown in green. Note that the B values are normalised to the average B value from each of their respective levels, not to the total average of all B values. Each distribution have been normalised to fit the height of the Porter-Thomas distribution.

There is little doubt that all three distributions for both $B(E1)$ and $B(M1)$ values closely match the Porter-Thomas distribution. In the bottom two plots of fig. 4.2 we see the relative difference to the Porter-Thomas distribution for all of the selected distributions. The $B(E1)$ values have relative differences which oscillate around 1 at approximately $B/\langle B\rangle = [0, 4]$ before the relative error starts to increase and keeps doing so for the rest of the range. The $B(M1)$ values have lower relative errors than the $B(E1)$ values for the entirety of the range. Going from lowest to highest j_i interval, the number of $B(E1)$ values included in the distributions are 12857, 33135 and 11300 respectively, and the number of $B(M1)$ values are 23631, 90936 and 33854 respectively. This seems to coincide well with the fact that the middle j_i interval generally shows the smallest relative error for both multipolarities because of the larger number of B values. The fact that there are fewer $B(E1)$ values than $B(M1)$ values also matches well with the larger relative errors we see for the distribution of $B(E1)$ values.

Consider now $B(E1)/\langle B(E1)\rangle > 4$ in the bottom left plot. As mentioned earlier, fluctuations are statistically expected and the fluctuations should grow in size when the number of B values gets smaller. However, what we see here seems to be a systematic overshoot of the $B(E1)$ values relative to the Porter-Thomas distribution. Systematic errors are per definition not random errors, and if this overshoot is indeed systematic, then its source might be rooted in a number of places in the codes which generated these calculations.

The calculations shown in fig. 4.2 strongly point to that the B values are indeed Porter-Thomas distributed. This is a good supplement to the calculations in fig. 4.1 because the good match to the Porter-Thomas

distribution substantiate the possibility that the fluctuations between the GSFs are Porter-Thomas fluctuations and not a breaking of the gBA hypothesis.

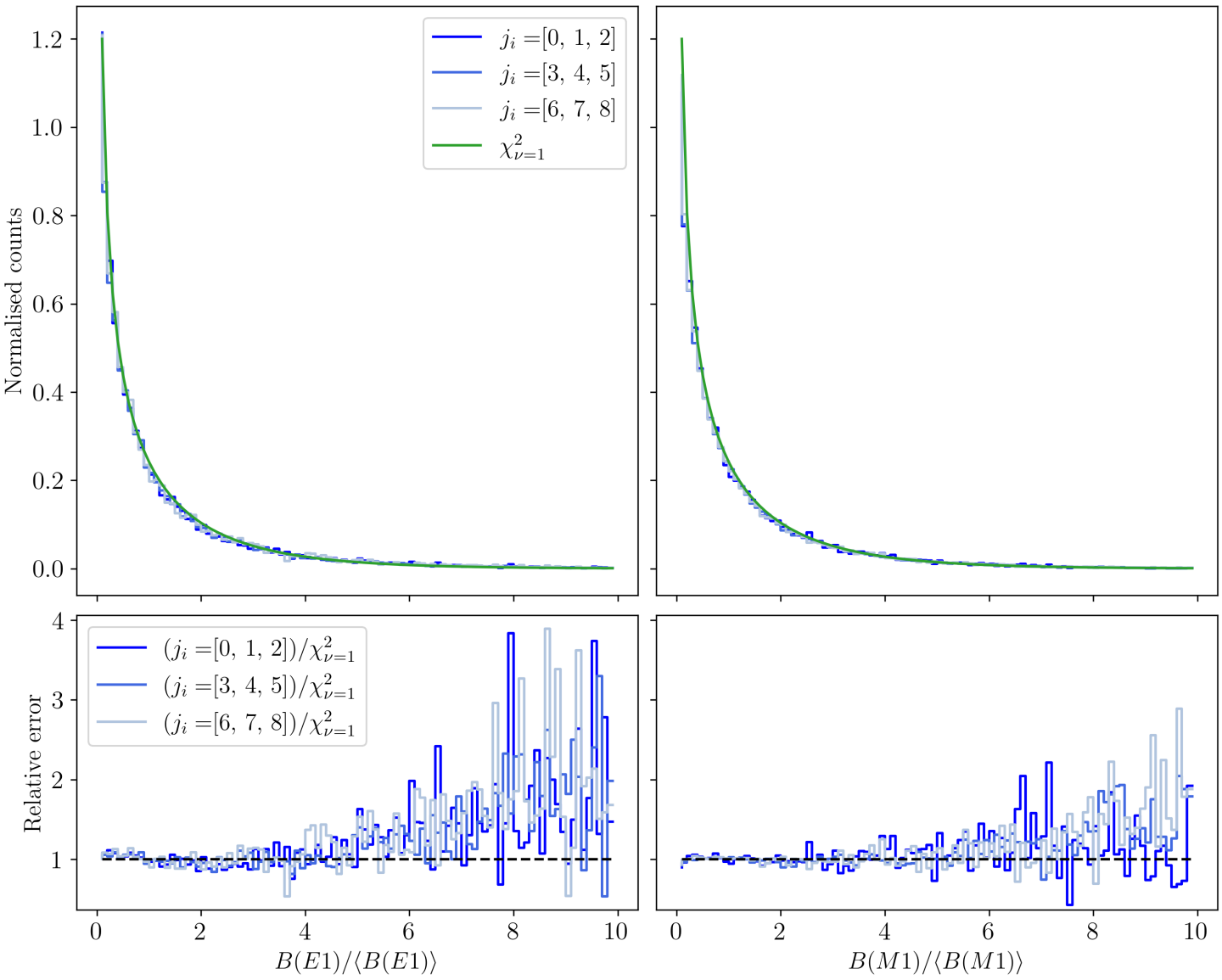

Figure 4.2: Distributions of B values of ^{44}Sc with the GCLSTsdpfsdgix5pn interaction using a $3\hbar\omega$ truncation and 200 levels for each angular momentum $j_i = 0, 1, ..., 8$ for both parities. The top two plots show the distributions of selections of B values selected from different j_i. The Porter-Thomas distribution is shown in green. The bottom two plots show the relative errors these distributions have from the Porter-Thomas distribution.

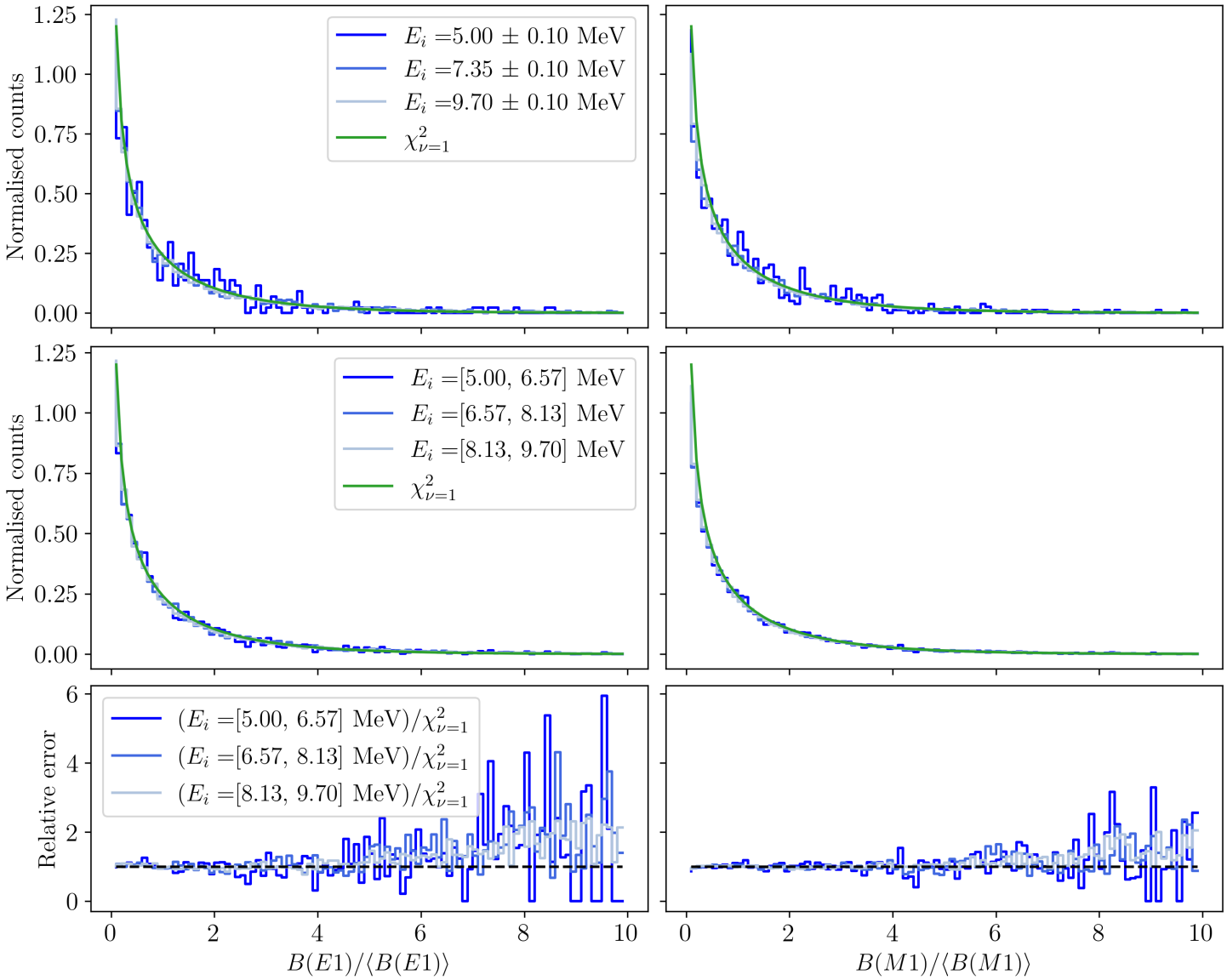

Figure 4.3: Distributions of B values of ^{44}Sc with the GCLSTsdpfsdgix5pn interaction using a $3\hbar\omega$ truncation and 200 levels for each angular momentum $j_i = 0, 1, ..., 8$ for both parities. The top two plots show the distributions of selections of B values selected from three different E_i values. The middle plots show distributions of B values selected from three different *ranges* of E_i values. The Porter-Thomas distribution is shown in green. The bottom two plots show the relative errors which the middle distributions have from the Porter-Thomas distribution. These plots are heavily inspired by fig. 3.3 in [12].

In fig. 4.3 we see a similar analysis but for selections of excitation energies instead of angular momenta. Again, $B(E1)$ values on the left and $B(M1)$ on the right. The top two plots show B distributions selected from excitation energies $E_i = 5, 7.35, 9.7$ MeV within a bin of size 0.2 MeV. For both $E1$ and $M1$ the $E_i = 5$ MeV distributions show the largest deviations from the Porter-Thomas distribution, while with increasing E_i the difference gets smaller. Again, this is because the number of B values in the distributions are – in order of increasing E_i – 374, 3089, 15610 for the $E1$ distributions and 674, 7766, 44072 for the $M1$ distributions. A larger number of B values will even out fluctuations. Despite the fluctuations, all distributions in the top two plots closely match the shape of the Porter-Thomas distribution which supports the fact that the B values are Porter-Thomas distributed however the B values are selected.

In the middle plots of fig. 4.3 the B values have been selected from *ranges* of E_i values. The number of B values included in the selections are – in order of increasing E_i range values – 4013, 13561, 39718 for the $E1$ distributions and 7026, 30838, 110557 for the $M1$ distributions. The increased number of B values is clearly manifested by the decrease in fluctuations as compared to the distributions in the top plots. The relative errors of these distributions to the Porter-Thomas distribution are shown in the bottom plots. We see that the errors are smallest in the lowest $B/\langle B\rangle$ range, and that the errors gradually increase as $B/\langle B\rangle$ increase. This behaviour is not surprising since we see from the middle plots that the amount of small $B/\langle B\rangle$ values is greater than the amount of large $B/\langle B\rangle$ values, which is somewhat of a redundant statement since that is literally what the shape of the distributions tells us.

As with the j_i analysis, there seems to be a systematic overshoot as $B/\langle B\rangle$ increases. The overshoot is seen clearly for the $E1$ for $B/\langle B\rangle > 4$. The origin of this systematic error is unknown, and might be rooted in KSHELL or in the data analysis. The overshoot is seen less clearly for the $M1$ values, though it does seem to be present there as well.

In fig. 4.4 we see for ^{50}V the $B(E1)$ and $B(M1)$ distributions for some angular momentum selections. Note in particular that there is something wrong with the $B(E1)$ distributions, shown in the left plots in the figure. `kshell-utilities` has not been able to scale the $B(E1)$ distributions to the Porter-Thomas distribution. See appendix B for details on how the scaling is performed. It turns out that the ^{50}V KSHELL calculations have very few non-zero $B(E1)$ values. There are simply too few $E1$ transitions of non-zero transition probabilities in the data set to produce a meaningful distribution. There is luckily no problem for the $M1$ transitions, whose B distributions we see in the right plots in fig. 4.4. From every selection of j_i the distributions have been successfully scaled and follow the shape of the Porter-Thomas distribution quite well. The accompanying relative errors in the bottom right plot reveals what might look like an oscillation around 1, where the relative errors start above 1, dips below 1, and seems to move above 1 towards the end of the $B(M1)/\langle B(M1)\rangle$ range.

In fig. 4.5 we see B distributions from selections of excitation energies. Not surprisingly, we see the same behaviour in the $B(E1)$ distributions here as with the j_i selections; there are not enough non-zero $B(E1)$ values to

produce (good) distributions that can be compared to the Porter-Thomas distribution. The $B(M1)$ distributions show a good match to the Porter-Thomas distribution.

The reason for the lack of $E1$ transitions is likely because of how KSHELL writes data to file. Some time ago, I found that KSHELL writes B values with 4 decimals of precision which I changed to 8 decimals because many values were rounded to zero with only 4 decimals of precision[2]. I performed all calculations except for ^{50}V after these changes were made, and this has resulted in bad $E1$ data for ^{50}V. This is supported by the $B(E1)$ distributions of ^{51}V – seen in fig. 4.6 – which follow the Porter-Thomas distribution much better than ^{50}V, however with some interesting relative errors which I will come back to.

The low number of non-zero $E1$ transitions of the ^{50}V might indeed affect the resulting $E1$ GSF. Note that zero values are not included in the calculations of the GSF[3] so they will not pull the average down, but a lack of transitions in the GSF calculations will give less correct results.

Luckily, the ^{51}V B distributions do not suffer from the same problem. The B distributions from selections of excitation energies in fig. 4.7 behave quite nicely for both $E1$ and $M1$ transitions. However, the distributions from selections of angular momenta in fig. 4.6 show some strange behaviour in the relative error of $B(E1)$. It seems that the scaling to the Porter-Thomas distribution has missed a bit, particularly seen just below $B(E1)/\langle B(E1)\rangle = 2$. Improving the scaling might reduce the overall relative error, but the clearly visible "banana" shape of the relative error is probably rooted somewhere else than the scaling. The scaling is simply multiplication of all the distribution bins with the same scaling factor, and changing the scaling factor will not change the overall shape of the distribution.

B distributions of ^{64}Zn from selections of angular momenta are displayed in fig. 4.8. Curiously, we see a "banana shape" in the relative errors of the $B(E1)$ distributions which looks similar to the "banana" we see for the same distributions of ^{51}V. Note also that the GSFs of ^{51}V (fig. 4.18) and of ^{64}Zn (fig. 4.19) look strikingly similar. The calculations for the two nuclei use different interactions and model spaces, and still we see such similar results. The $M1$ distributions more closely resembles the Porter-Thomas distribution. The same can be said for the $B(M1)$ distributions in fig. 4.9, where the selections are from various excitation energies. Here too, the $E1$ values are different from the Porter-Thomas distribution, and we can see a "banana shape" in the relative errors.

[2]The specific changes can be found here: https://github.com/GaffaSnobb/kshell/commit/b3083296c6e84f948011c987870c73c2ef148436.

[3]This specific part of the calculation can be seen here: https://github.com/GaffaSnobb/kshell-utilities/blob/2c4b9de7974e21fbc2975ff116ce5ebbe1fad57a/kshell_utilities/general_utilities.py#L573.

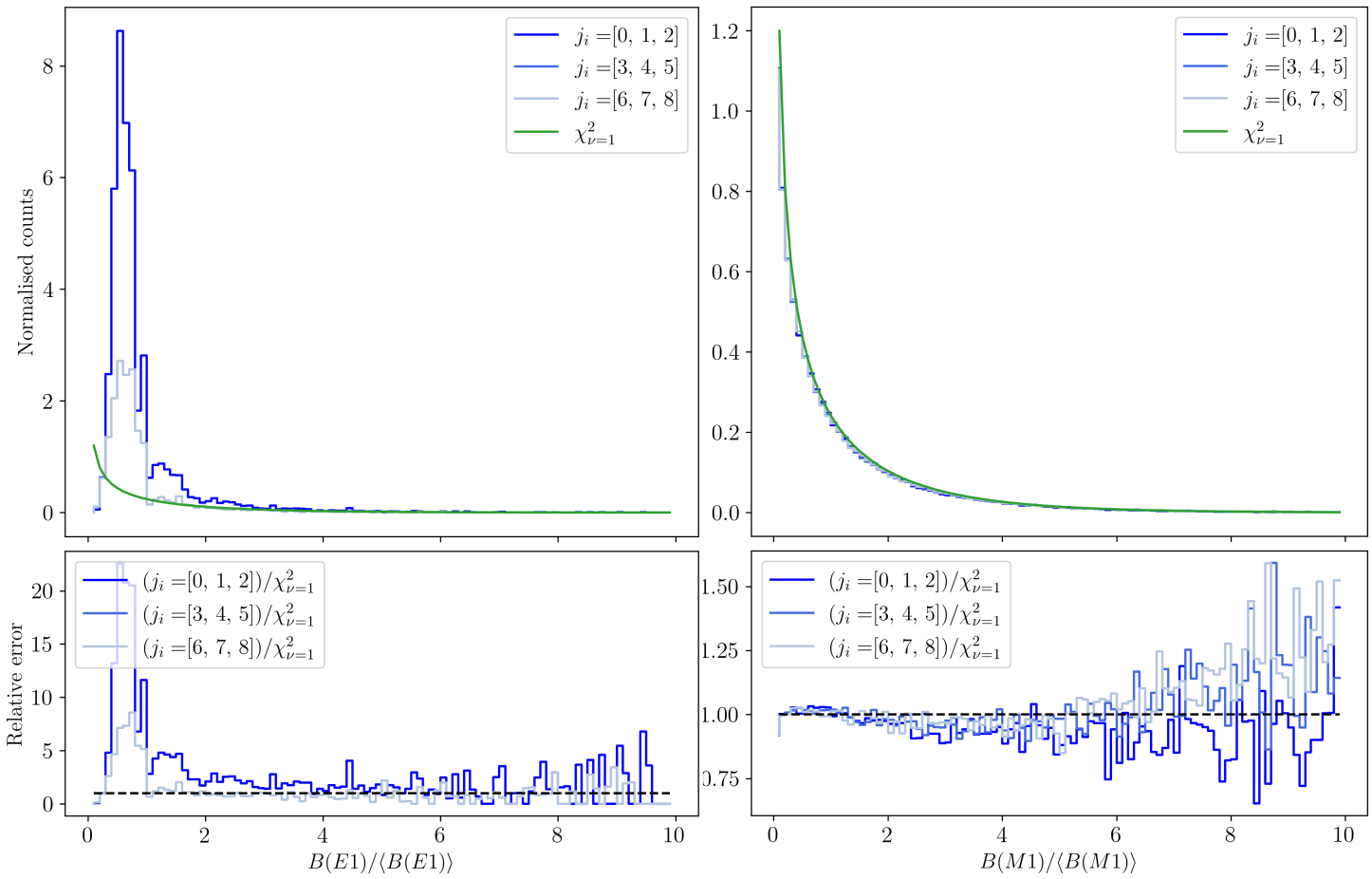

Figure 4.4: In blue, B distributions of ^{50}V from selections of angular momenta. The Porter-Thomas distribution is shown in green. Calculated with the SDPF-MU interaction with a $1\hbar\omega$ truncation. 200 levels were calculated for $j_i = 0, 1, ..., 8$ for both parities.

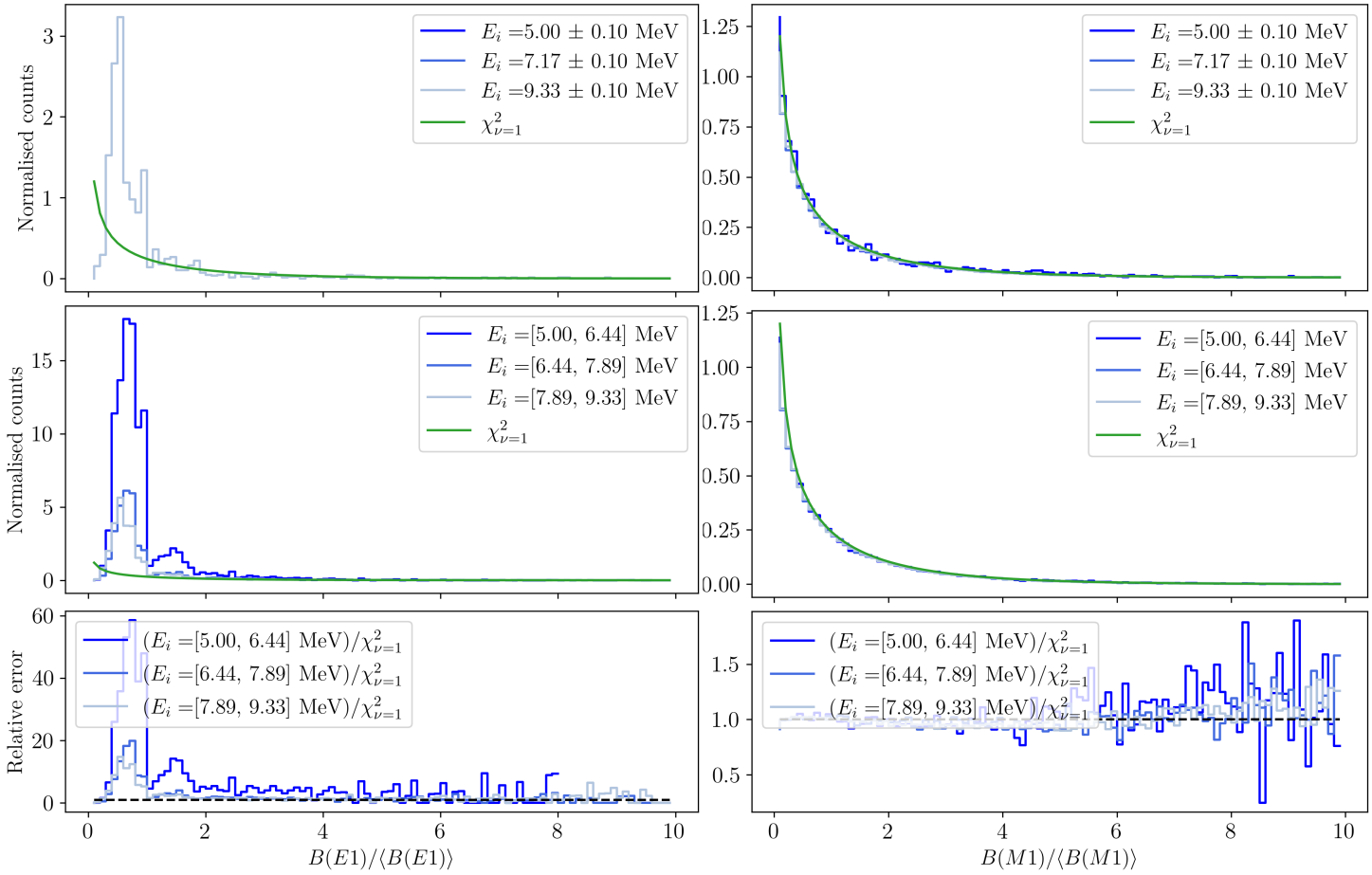

Figure 4.5: In blue, B distributions of ^{50}V from selections of excitation energies. The Porter-Thomas distribution is shown in green. Calculated with the SDPF-MU interaction with a $1\hbar\omega$ truncation. 200 levels were calculated for $j_i = 0, 1, ..., 8$ for both parities.

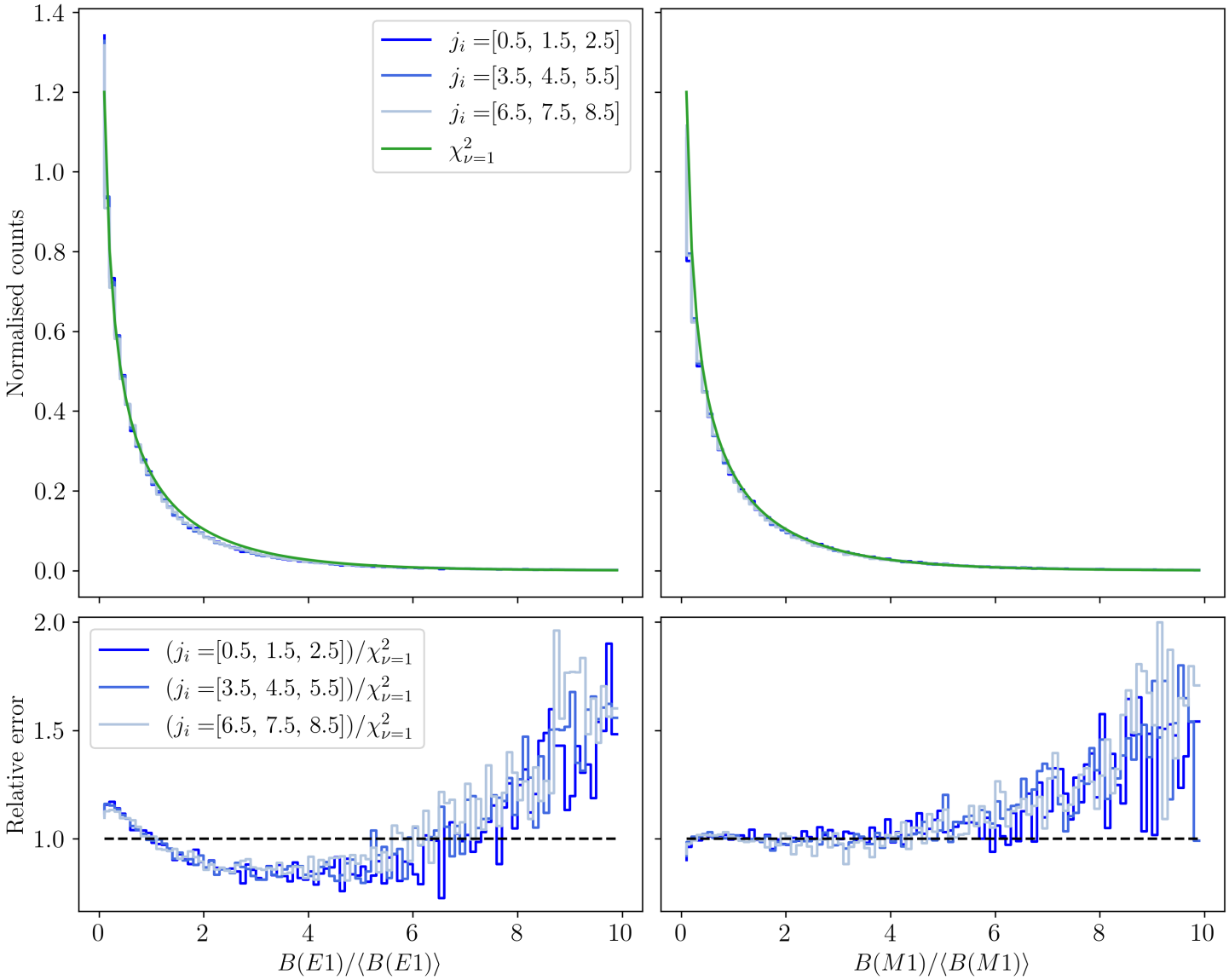

Figure 4.6: In blue, B distributions of ^{51}V from selections of angular momenta. The Porter-Thomas distribution is shown in green. Calculated with the SDPF-MU interaction with a $1\hbar\omega$ truncation. 200 levels were calculated for $j_i = 1/2, 3/2, ..., 17/2$ for both parities.

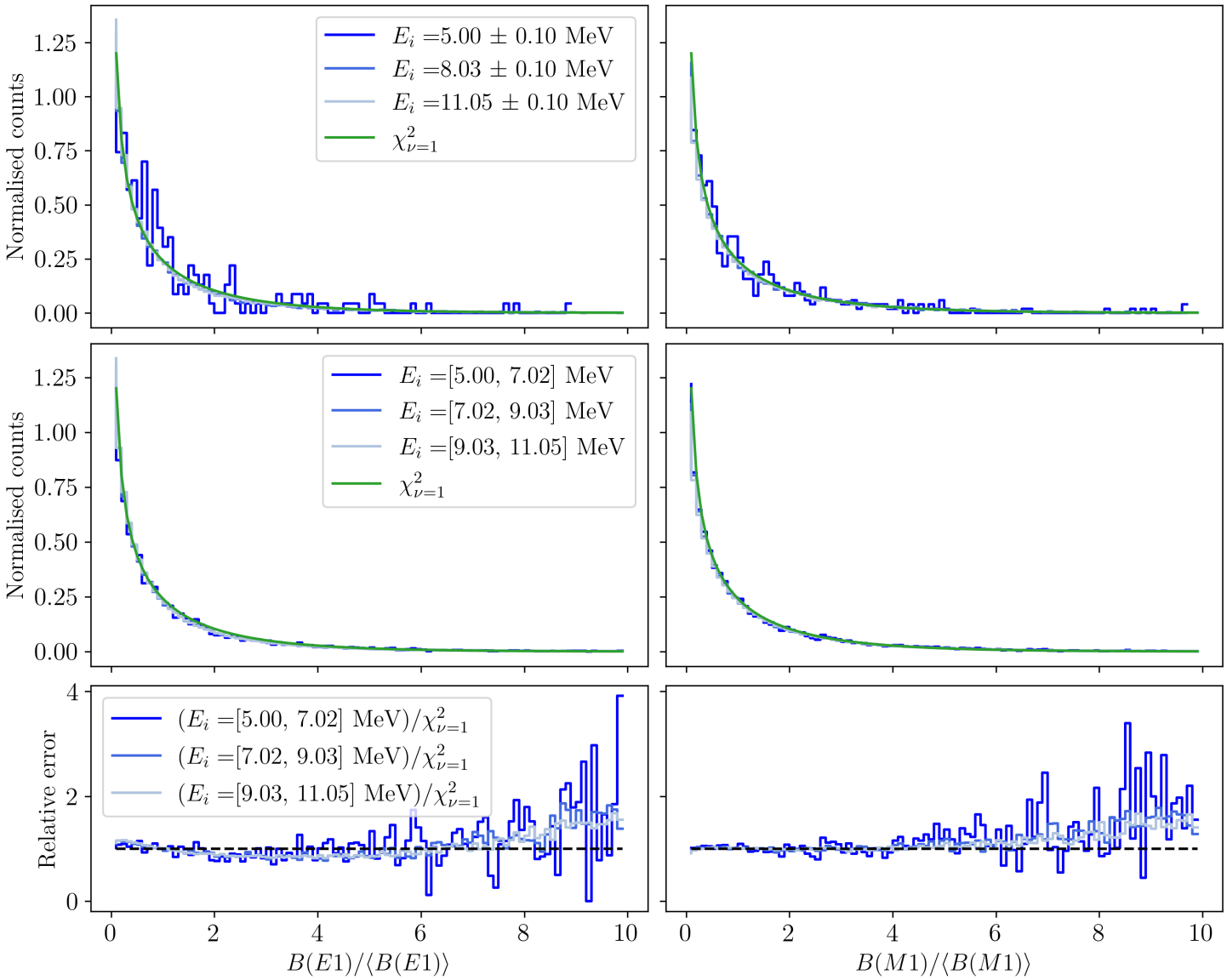

Figure 4.7: In blue, B distributions of ^{51}V from selections of excitation energies. The Porter-Thomas distribution is shown in green. Calculated with the SDPF-MU interaction with a $1\hbar\omega$ truncation. 200 levels were calculated for $j_i = 1/2, 3/2, ..., 17/2$ for both parities.

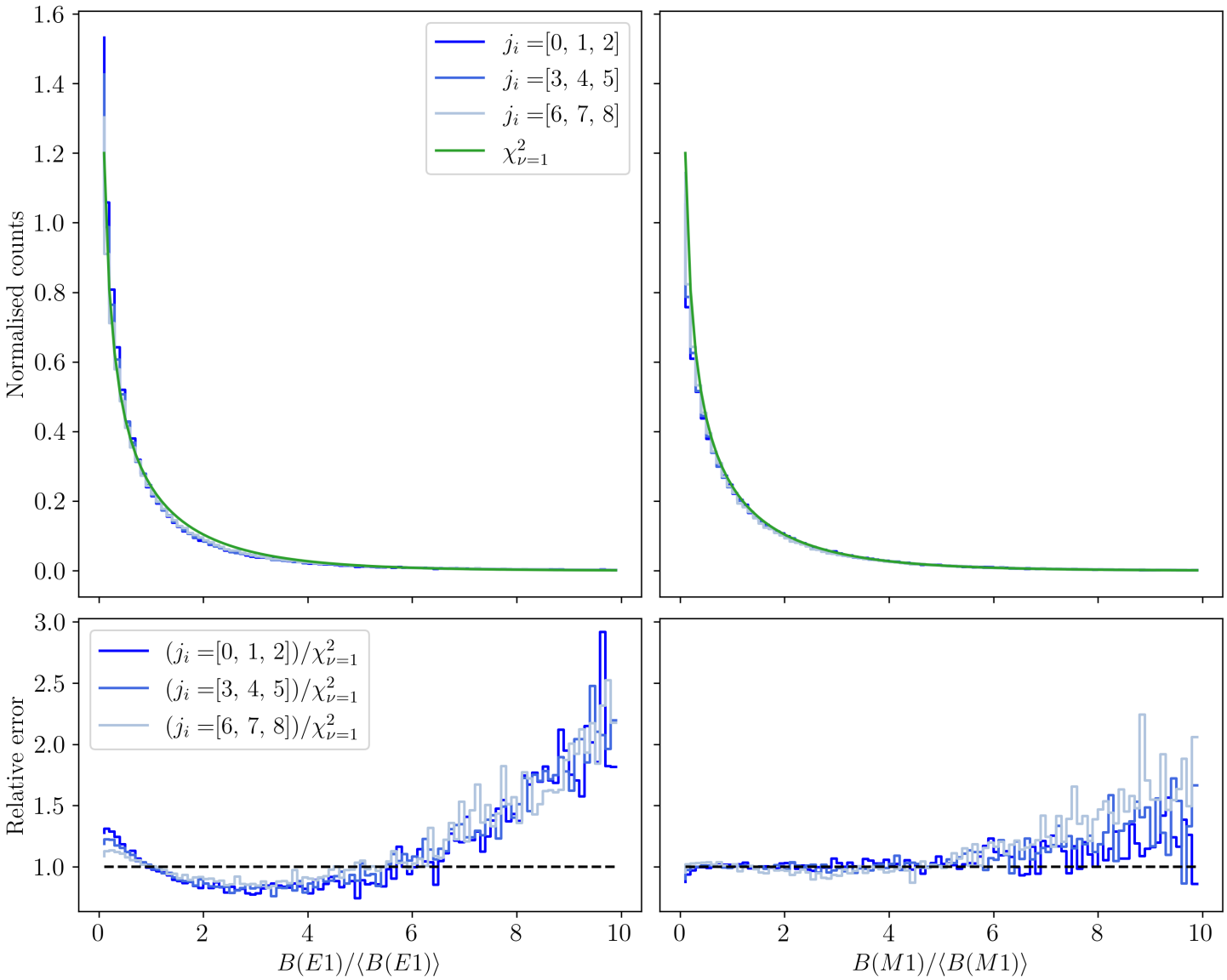

Figure 4.8: In blue, B distributions of ^{64}Zn from selections of angular momenta. The Porter-Thomas distribution is shown in green. Calculated with the gs8 interaction with a $1\hbar\omega$ truncation including a minimum occupation of 14 nucleons in the $1f_{7/2}$ orbitals (protons and neutrons combined). 200 levels were calculated for $j_i = 0, 1, ..., 8$ for both parities.

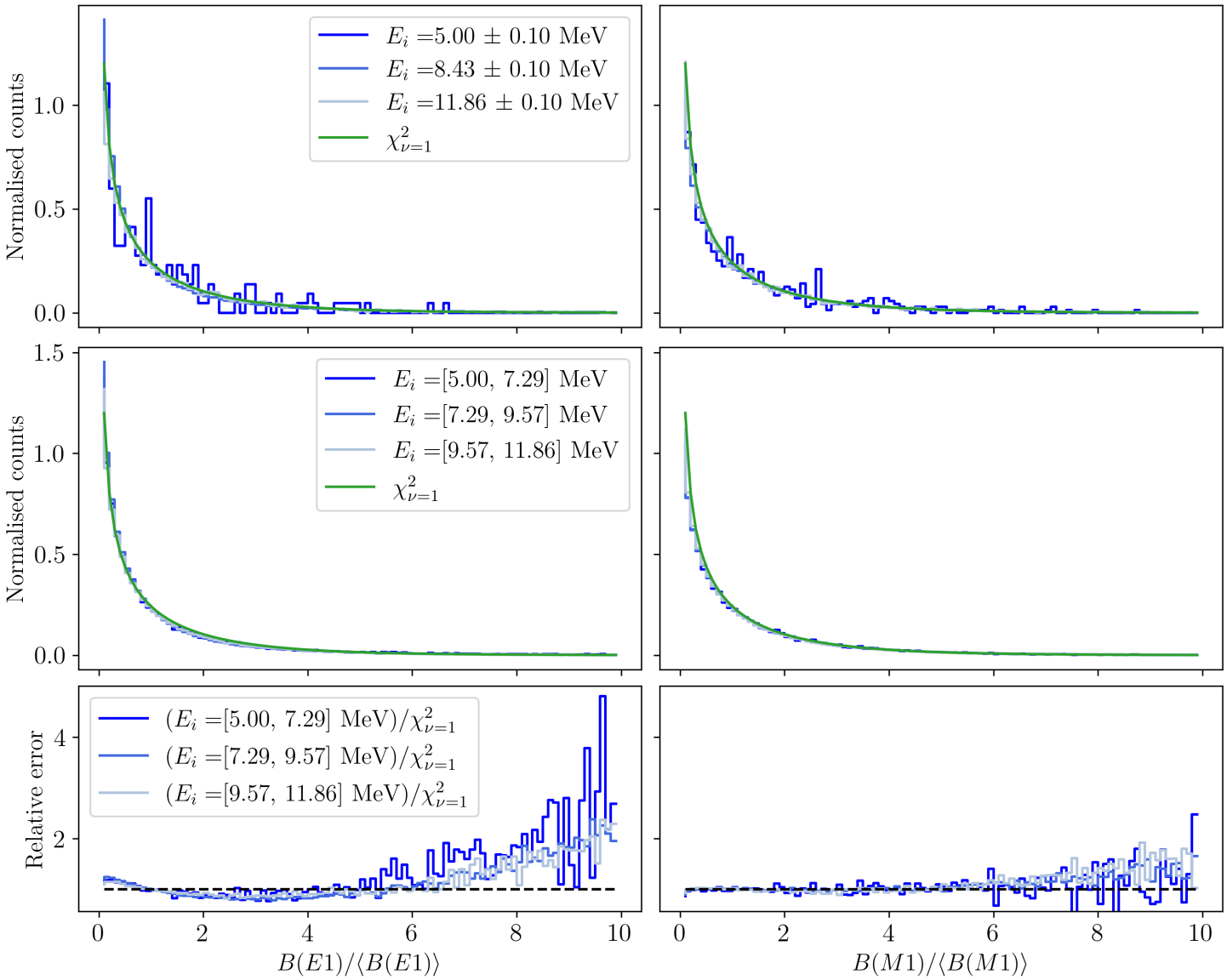

Figure 4.9: In blue, B distributions of ^{64}Zn from selections of excitation energies. The Porter-Thomas distribution is shown in green. Calculated with the gs8 interaction with a $1\hbar\omega$ truncation including a minimum occupation of 14 nucleons in the $1f_{7/2}$ orbitals (protons and neutrons combined). 200 levels were calculated for $j_i = 0, 1, ..., 8$ for both parities.

The point of the B distribution plots is to try to use the statistical nature of the B values to account for fluctuations we might find in the GSF. These fluctuations are shown for ^{50}V in fig. 4.10 where we see in grey the GSF calculated individually for all angular momenta (eq. (2.46)) while the GSF averaged over all j_i is shown in black (eq. (2.43)). We see that both the $E1$ and $M1$ GSFs tightly follow their average. We do see large fluctuations at the very highest gamma energies for both $E1$ and $M1$, but this is probably due to a reduced number of B values included in the calculations as the gamma energy increases. This is explained in section 4.2. We also see that the $E1$ GSFs have a larger spread than the $M1$ GSFs, which might be due to the low number of non-zero $B(E1)$ values as discussed earlier in this section. Recall that the GSF describes *average* electromagnetic transition probabilities, and that this average will better reflect reality if we have a large number of B values to use in the average. All in all, the spread of the GSFs is not very large which supports the idea that the GSF is approximately independent of angular momentum. If we take fig. 4.4 and fig. 4.5 into consideration as well, where we see that the $B(M1)$ values closely follow the Porter-Thomas distribution, the small fluctuations we see in the GSFs might be within the statistical expectations.

The story for ^{51}V in fig. 4.11 is similar to ^{50}V, however, with somewhat larger fluctuations in the $M1$ GSFs and smaller fluctuations in the $E1$ GSFs. The latter is likely due to more non-zero $B(E1)$ values for ^{51}V. The $M1$ calculations should be "of the same quality" for both ^{50}V and ^{51}V since the two calculations are identical, save for one extra neutron in ^{51}V. Still, we see larger fluctuations in the $M1$ GSFs for ^{51}V than for ^{50}V which might be related to the complete filling of the $1f_{7/2}$ neutron orbital for ^{51}V (see fig. 2.7). The spread of the GSFs is not very large, and the calculations point to an independence of angular momentum in the GSF of ^{51}V. However, the "banana behaviour" of the relative difference in fig. 4.6 warrants further investigation in the distribution of these B values before any safe conclusions may be made.

The same analysis for ^{64}Zn is shown in fig. 4.12. We see a rather interesting behaviour in the $E1$ GSF where several of the individual j_i GSFs starts to rapidly decrease at 6 to 7 MeV, something which happens to the other nuclei at above 8 MeV. The explanation is possibly due to computational limitations. In general, heavier nuclei have larger NLDs than lighter nuclei when compared at the same excitation energy. Since ^{64}Zn is significantly heavier than ^{50,51}V, the former should have a larger NLD than the two latter. Recall that calculations for all nuclei in this work include 200 levels per $j_i^{\pi_i}$ which means that the 200th level for one of the vanadium isotopes will have a higher excitation energy than the 200th level of the zinc isotope. Thus, the shell model calculations of the lighter vanadium nuclei go faster into a higher energy regime compared to the heavier zinc nucleus. This is backed up by fig. 4.13 where we see the NLD as a function of both energy and angular momentum for ^{51}V and ^{64}Zn. The figures show that ^{51}V in general has more levels at higher energies than ^{64}Zn despite the fact that the shell model calculations gave 200 levels for each $j_i^{\pi_i}$ for both of the isotopes. We might therefore need even bigger shell model calculations for

^{64}Zn to get the same quality as for ^{50,51}V above 6 MeV.

We see a similar behaviour for the $M1$ GSF where some of the individual GSFs start to fall at just over 6 MeV. Since the GSFs of both $E1$ and $M1$ transitions have a low spread at energies below 4 MeV, I find it likely that the deviations above 4 MeV (6 MeV for $M1$) are due to the aforementioned computational limitations.

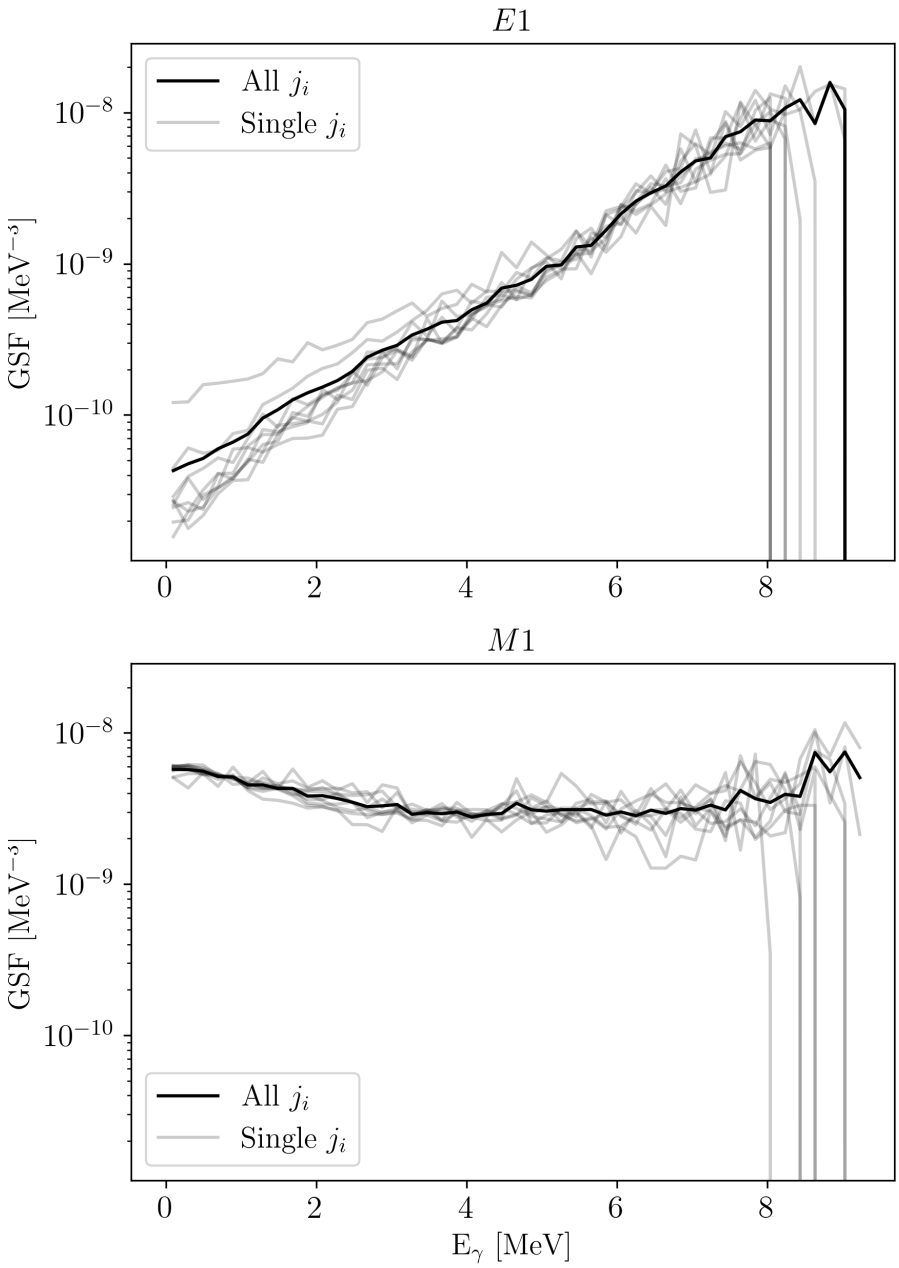

Figure 4.10: The GSF of ^{50}V using the SDPF-MU interaction with a $1\hbar\omega$ truncation and 200 levels for each angular momentum $j_i = 0, 1, ..., 8$ for both parities. The GSF for each individual j_i is shown in grey and their average is shown in black. Top: the $E1$ GSFs. Bottom: the $M1$ GSFs.

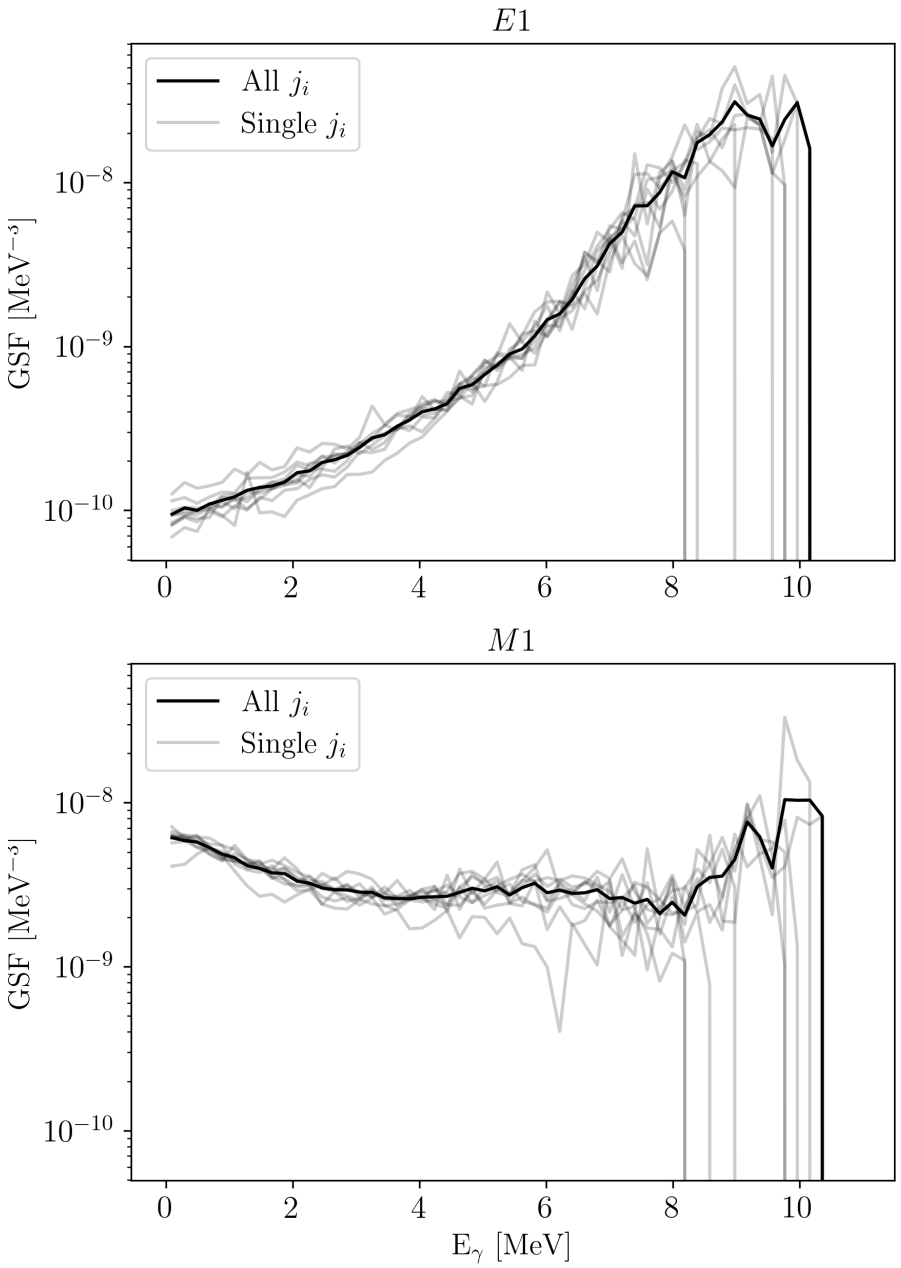

Figure 4.11: The GSF of ^{51}V using the SDPF-MU interaction with a $1\hbar\omega$ truncation and 200 levels for each angular momentum $j_i = 1/2, 3/2, ..., 17/2$ for both parities. The GSF for each individual j_i is shown in grey and their average is shown in black. Top: the $E1$ GSFs. Bottom: the $M1$ GSFs.

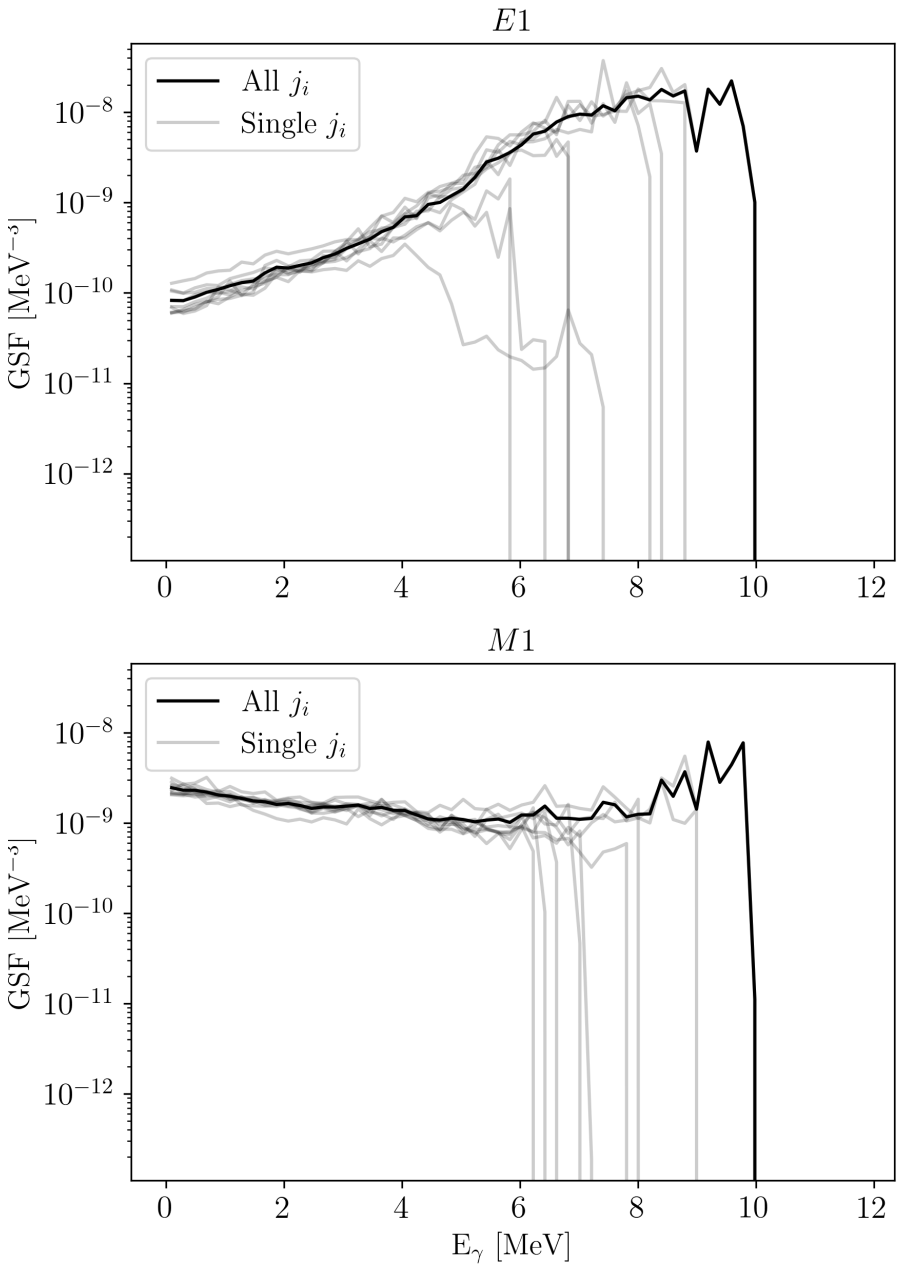

Figure 4.12: The GSF of ^{64}Zn using the gs8 interaction with a $1\hbar\omega$ truncation, including a minimum occupation of 14 nucleons in the $1f_{7/2}$ orbitals (protons and neutrons combined). 200 levels for each angular momentum $j_i = 0, 1, ..., 8$ for both parities were used. The GSF for each individual j_i is shown in grey and their average is shown in black. Top: the $E1$ GSFs. Bottom: the $M1$ GSFs.

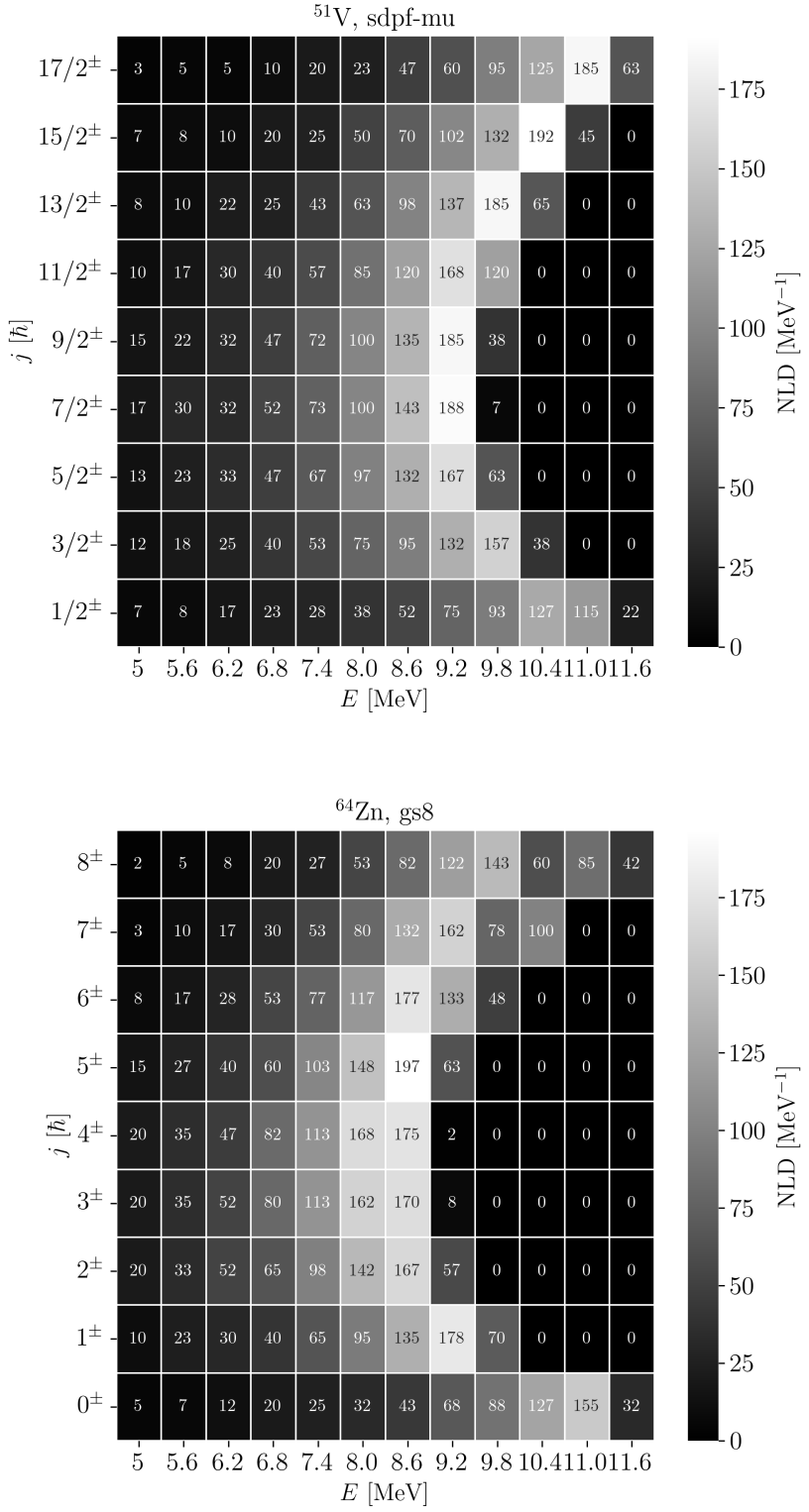

Figure 4.13: NLD as a function of energy (abscissa) and angular momentum (ordinate). A bin size of 0.6 MeV has been used. Note that each energy bin is labelled with its lowest energy, meaning that the 5 MeV bin spans $[5, 5.6)$ MeV. Top: ^{51}V. Bottom: ^{64}Zn.

4.2 The GSF's dependence on the number of levels

In fig. 4.14 we see the $E1$ GSF and NLD of ^{44}Sc in the GCLSTsdpfsdgix5pn interaction with a $3\hbar\omega$ truncation. I have used 60, 100, and 200 energy levels for each total angular momentum and each parity to highlight the implications of changing the number of levels. Note in particular the GSF for 60 levels which shows large fluctuations at approximately $E_\gamma = 7$ MeV and higher. The GSF for 100 levels starts to show large fluctuations at about 8 MeV, and with 200 levels at about 9 MeV. These points of interest, 7 MeV, 8 MeV, and 9 MeV, also show up in the accompanying NLD where they indicate where the NLD stops rising exponentially.

The correspondence between the GSF and NLD for these points of interest is no coincidence. Remember that we expect the NLD to increase approximately exponentially as a function of energy, as seen from for example the constant temperature model, eq. (2.39). Since KSHELL calculates levels in order of increasing energy and since I have requested a finite number of levels N, an excitation energy will be reached where N levels is not sufficient to fill up the exponential curve. Those are the critical points (of interest) which we see clearly in the NLD in fig. 4.14 where the three graphs starts to deviate from the exponential trend. At these points the shell model calculations start to lack levels, which comes to light in the GSF as large fluctuations. The fluctuations are caused by the GSFs dependence on the partial width averaged in an excitation energy interval $\langle\Gamma\rangle$, and the NLD ρ, which we see in eq. (2.43). Recall that the partial width depends on the reduced transition probability B by $\Gamma \propto B$, or rather, the *average* of many B values. With too few levels there are too few transitions in the average of B, which in turn might give an artificial over or under representation of strong or weak transition probabilities. We therefore see large fluctuations due to the lack of transitions to smooth out the GSF.

Note also that the NLD does not go to zero instantly when the number of requested levels has been reached. If I request 200 levels for each j^π pair, then KSHELL might be done with calculating all 200 0^+ levels while there are still 1^+ levels left to calculate; some or all of the remaining 1^+ levels might be of higher energy than the 201st, 202nd, etc 0^+ levels which were not calculated. This gives a tail in the NLD which takes some time to go to zero. In other words, there is no guarantee that the 3200 lowest lying levels are exactly divided as 200 levels per j^π pair. In fact, it is probable that there are more low than high angular momentum levels in the low level regime since high (low) angular momentum in general corresponds to high (low) excitation energy. The consequence of evenly dividing the levels by total angular momentum is that the NLD does not instantly fall to zero towards higher excitation energies, but rather leaves a tail from where the exponential trend cannot be kept, thus causing the GSF to largely fluctuate at high transition energies. In a sense, all levels located in the NLD tail might be considered wasted since the computational resources would be better served calculating lower energy levels, giving a stable GSF across the entire gamma energy range. A way to achieve this is to have an uneven distribution of levels over angular momenta.

The reason why we see large fluctuations only in the high energy part of the GSF is that only high energy levels can be responsible for high energy gamma decays. For example, a gamma decay of $E_\gamma = 8$ MeV must come from a level of 8 MeV or higher. When the NLD starts to deviate from the exponential trend, it is due to a lack of levels in the upper energy regime of the shell model calculation. Low energy gamma decays are thus not affected in the same way, since low energy levels also account for low energy gamma decays. However, since high energy levels also decay by low energy gammas, we do expect to see the entire GSF being affected by changing the number of levels included in the shell model calculation. This is exactly what we see in fig. 4.14. The entire GSF is generally lower for 60 and 100 levels as compared to 200 levels. We can think of this intuitively by imagining that with zero levels there would be no transitions and hence no GSF. If I then increase the number of levels there will be an increase in number of transitions and an increase in the GSF. However, there seems to be a limit to how much the GSF will increase just by including more levels. The difference between the GSF for 100 and 200 levels is generally smaller than the difference between the GSF for 60 and 100 levels. The increase in the GSF seems to be smaller when increasing an already (relatively) large number of levels. There seems to be an asymptotic behaviour towards what I can only hope to be the true GSF. I have included a figure in the appendix, fig. A.1, which shows the same GSF but without the logarithmic y axis. There it is easier to see that the difference between 100 and 200 levels is indeed generally smaller than the difference between 60 and 100 levels.

This analysis shows the importance of using a large enough number of levels when calculating the GSF. The number of levels affects the GSF over the entire energy range though in particular the high energy part. The accompanying NLD should be studied to see where it starts to deviate from the expected exponential growth. The GSF data at energies higher than this deviation will exhibit fluctuations and cannot entirely be trusted. Consider again fig. 4.13, and take ^{51}V in the upper heat map as an example. Recall that 200 levels were calculated per j^π pair making each row in the plot contain 400 levels (both parities are summed). We see that the peak of each row is not located at the same excitation energy, for example that the peak of $j^\pi = 7/2^\pm$ is in the 9.2 MeV bin while the peak of $j^\pi = 17/2^\pm$ is in the 11 MeV bin. It might therefore be better to increase the numbers of levels calculated for $j^\pi = 7/2^\pm$ and decrease the number of levels calculated for $j^\pi = 17/2^\pm$.

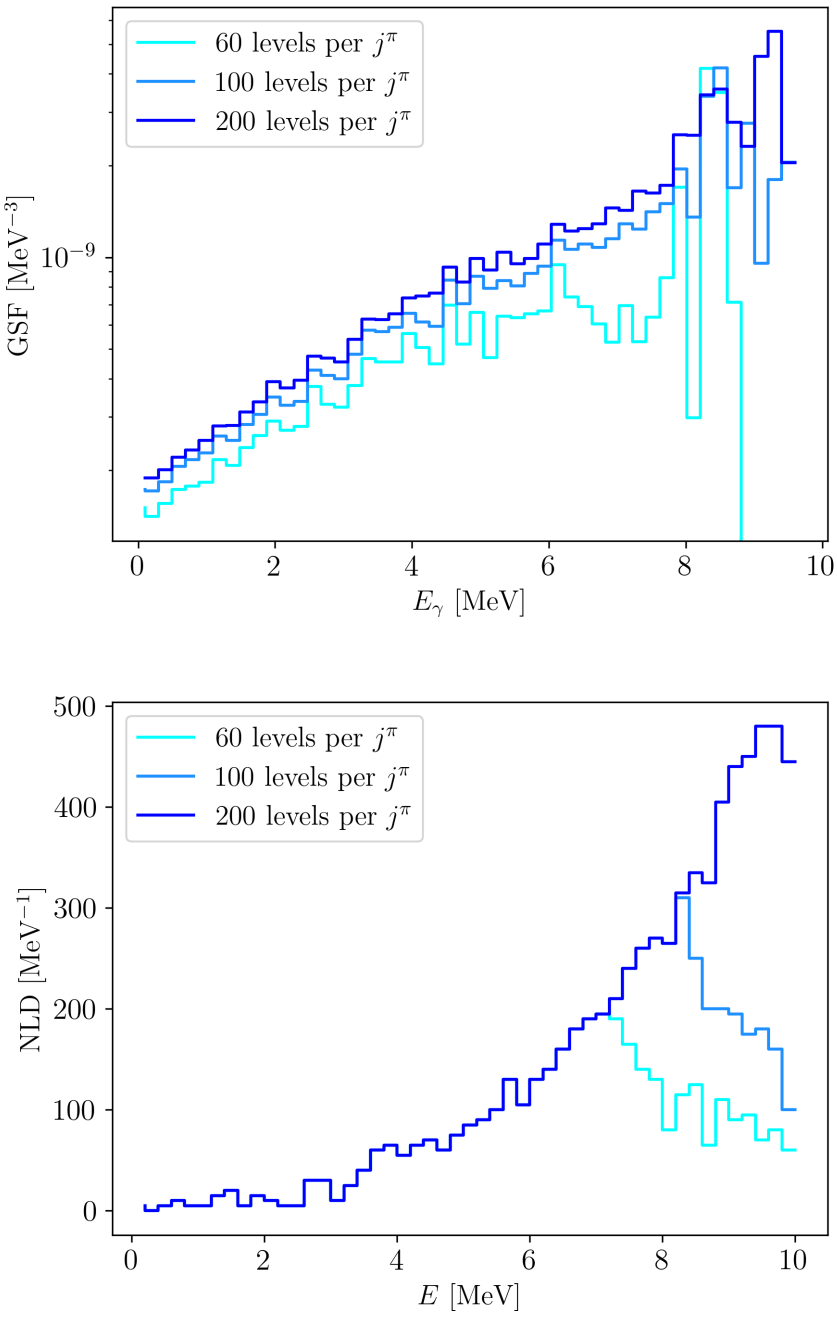

Figure 4.14: Top: The $E1$ GSF of ^{44}Sc in the GCLSTsdpfsdgix5pn interaction with $3\hbar\omega$ truncation for 60, 100, and 200 levels per j^π. Total angular momenta $j_i = 0, 1, ..., 8$ are used for both parities. Bottom: The nuclear level density for the same calculations. Both figures depict the consequences of changing the number of levels per j^π for the NLD and GSF.

4.3 Partial level density versus total level density

In earlier work, K. Sieja [29] compared shell model calculations with experimental Oslo method GSF and NLD data of ^{44}Sc from A. C. Larsen et al [2]. Sieja's data seems to coincide well with the experimental data. However, we have a strong reason to believe that both Sieja's data and the experimental data is incorrect. Experiments on ^{50,51}V by A. C. Larsen et al [3] show that the GSFs of ^{50,51}V (bottom two plots in fig. 4.18) are almost an order of magnitude lower than that of ^{44}Sc. In addition, we have greater confidence in the ^{51}V GSF because it is normalised to relatively good neutron resonance data. According to the Thomas-Reiche-Kuhn (TRK) sum rule [8],

$$\sigma_{\text{total}} = \frac{2\pi^2 e^2 \hbar}{mc}\frac{NZ}{A} \approx 0.06\frac{NZ}{A}\text{MeV}\cdot\text{b}, \tag{4.3}$$

the integrated dipole cross section of the three isotopes are

$$\begin{aligned}\sigma_{\text{total}}(^{44}\text{Sc}) &= 0.66\text{MeV}\cdot\text{b},\\ \sigma_{\text{total}}(^{50}\text{V}) &= 0.75\text{MeV}\cdot\text{b},\\ \sigma_{\text{total}}(^{51}\text{V}) &= 0.76\text{MeV}\cdot\text{b}.\end{aligned} \tag{4.4}$$

From the values in eq. (4.4) it seems implausible that the GSF of ^{44}Sc should be almost an order of magnitude larger than the GSFs of ^{50,51}V. The experimental GSF of ^{44}Sc in [2] was extracted using the Oslo method [41]. The Oslo method is dependent on normalisation factors external to the method itself to scale the GSF correctly. To scale the ^{44}Sc GSF they used data of two resonances from the reaction $^{45}\text{Sc}(n,\gamma)$ and the observation of 13 $E1$ and 9 $M1$ transitions at average energy 7.0 and 7.2 MeV respectively. The GSF at these two energies were calculated from the average of the 13 $E1$ and 9 $M1$ transitions, and was used as a normalisation factor for the Oslo method GSF. An apparent problem with this normalisation procedure is that very few transitions were used to calculate the normalisation factor, which means that large or small transition probabilities could easily be over or under represented. We have seen in fig. 4.14 that few levels – and subsequently few transitions – leads to large fluctuations in the GSF. An over representation of strong transitions in the normalisation factors is a plausible explanation to why the experimental GSF of ^{44}Sc is so large compared to its neighbours ^{50,51}V. For comparison, in fig. 4.14 I used 3369 and 8515 $E1$ transitions in the 200 levels shell model calculations of the GSF at 7.0 and 7.2 MeV respectively.

By using the total level density,

$$\rho_{\text{total}}(E_i) = \sum_{j_i,\pi_i} \rho(E_i, j_i, \pi_i), \tag{4.5}$$

we introduce an artificial scaling which depends on how many j_i, π_i combinations, and consequently how many levels, were included in the calculations. By including more or fewer levels, the total level density will increase or decrease and thus in turn increase or decrease the GSF. This

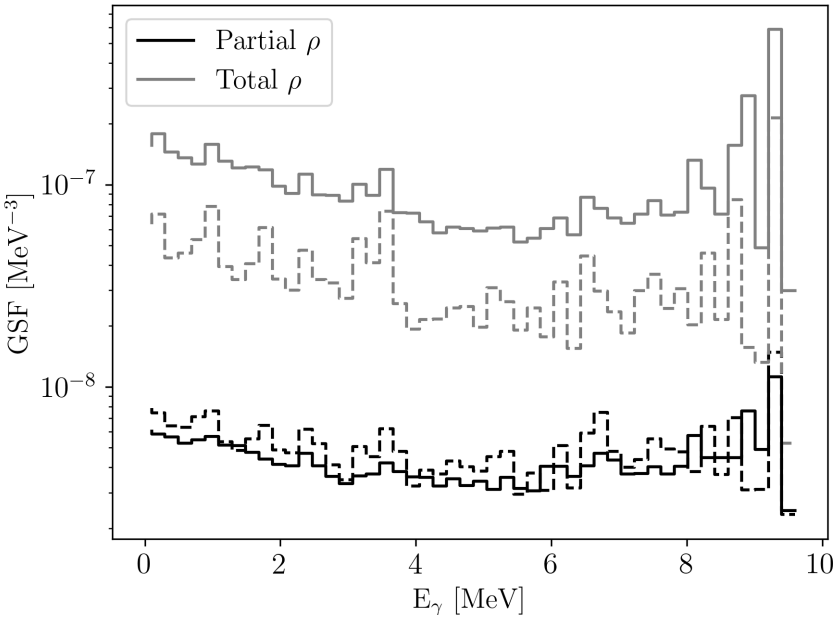

Figure 4.15: The GSF of ^{44}Sc with the GCLSTsdpfsdgix5pn interaction and a $3\hbar\omega$ truncation with 200 levels per j_i for both parities. The black lines show the GSF calculated with the partial level density, while the grey lines show the GSF using the total level density. Solid lines indicate that $j_i = 0, 1, ..., 8$ have been used in the calculations, while dashed lines indicate that only $j_i = 0, 1, 2$ have been used.

artificial scaling is not of any physical meaning, and we must use the partial level density to get the correct answer. Figure 4.15 shows the effect of the artificial scaling. Not only do we see that using the total level density (grey) gives an overall scaling as compared to using the partial level density (black), we also see that by including fewer (dashed) or more (solid) levels in the calculation, the partial level density GSF has little to no change while the total level density GSF shows a noticeable scaling. I have aimed at reproducing the shell model calculations from the work of K. Sieja [29] with as similar input parameters as possible. Sieja used the coupled scheme code `NATHAN` [42] and calculated ^{44}Sc in the sd, pf, sdg model space with a g_s quenching factor of 0.75 and a truncation of $1\hbar\omega$. Sieja calculated up to 60 levels of each parity in the angular momentum range $j = 0, 1, ..., 12$, and included only levels below 10 MeV due to the neutron separation energy of ^{44}Sc being 9.7 MeV. This amounts to a total of 1078 levels for both parities.

The interaction used by Sieja is not available for KSHELL, so I have chosen to use the GCLSTsdpfsdgix5pn interaction since it also uses the sd, pf, sdg model space. I have applied a quenching factor of 0.75[4], used $1\hbar\omega$ truncation, and calculated 60 levels for each parity in the angular momentum range $j = 0, 1, ..., 12$, except for $j^\pi = 9^+, 10^+, 11^+, 12^+$ which have 51, 21,

[4] 0.75 is also the recommended quenching factor for GCLSTsdpfsdgix5pn, see table A.1

7, and 1 level respectively. The reason for the reduced amount of levels is because the GCLSTsdpfsdgix5pn interaction with a $1\hbar\omega$ truncation supports a maximum of 51, 21, 7, and 1 level for the mentioned angular momentum-parity pairs. After slicing away initial excitation energies above 10 MeV and below 5 MeV, 949 levels remained for the NLD calculation, while 43446 and 62211 transitions remained for the $E1$ and $M1$ GSF calculation, respectively.

The results of the GSF calculations with parameters matching K. Sieja's work are displayed in fig. 4.16. The top figure shows experimental data in black dots compared with shell model calculations using the *total* level density in the GSF calculation, while the bottom figure shows the same comparison but with the *partial* level density. The partial level density is the correct choice, as we see from the definition of the GSF in eq. (2.43). It seems that the reason why the shell model calculations matches the incorrectly normalised experimental data is because the total level density gives an artificial scaling based on how many levels are included in the shell model calculation. The scaling so happens to match the experimental data well. I have demonstrated this effect in fig. 4.15, where we see that including more levels gives an increase in the entire GSF. Note that Sieja's shell model calculations matches the experimental data even better than what I have achieved here, as can be seen in fig. 6 in her paper. The differences between my reproduction and Sieja's calculations are probably due to us using different codes and different interactions.

In the bottom figure of fig. 4.16 I have used the partial level density. The $E1 + M1$ shell model GSF is shown in grey and is approximately an order of magnitude below the experimental data. A preliminary renormalisation of the experimental data is included as grey dots. The renormalised data matches the partial level density SM GSF very well, which is in good agreement with my earlier suspicion that the original experimental data is incorrectly normalised to about a factor of 10.

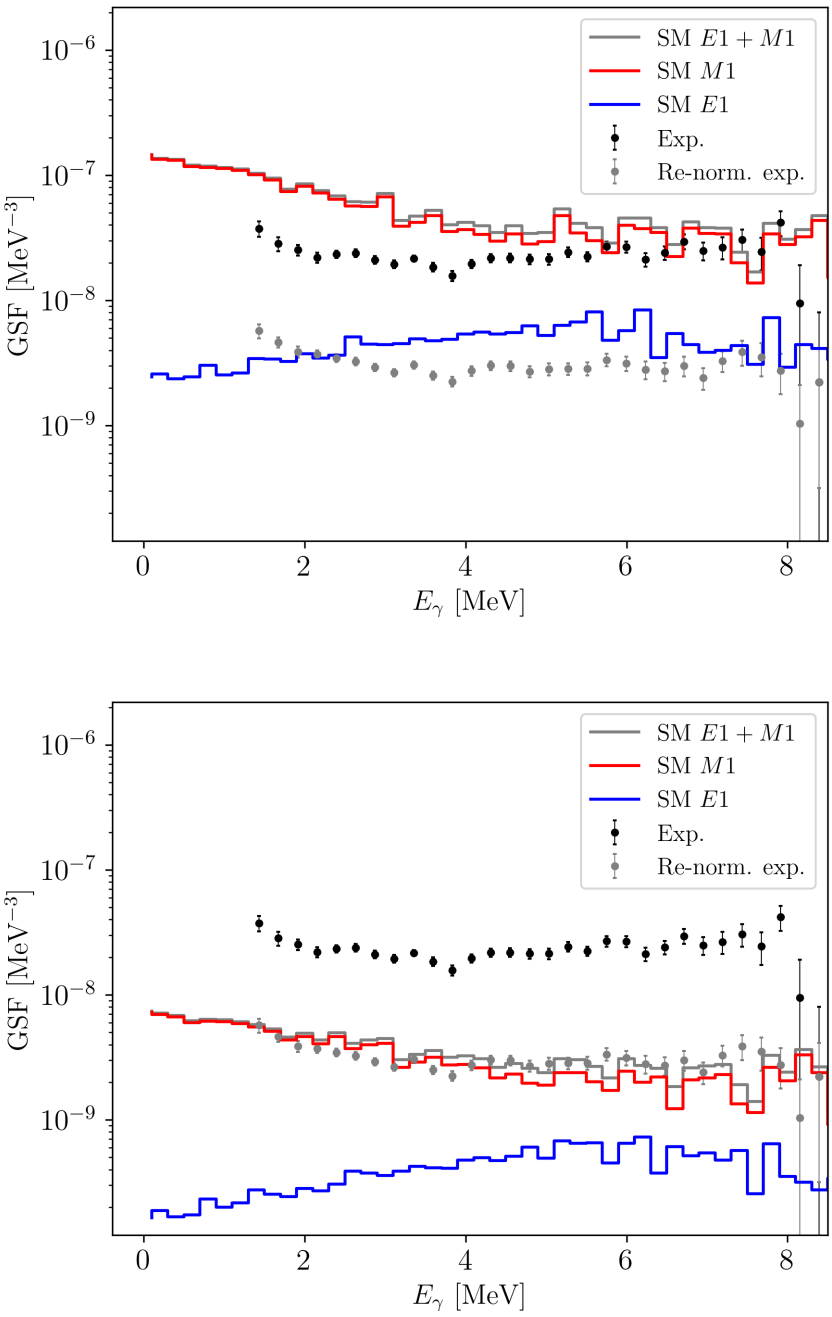

Figure 4.16: The GSF for ^{44}Sc in the GCLSTsdpfsdgix5pn interaction with $1\hbar\omega$ truncation. The input parameters are chosen specifically to match the ^{44}Sc calculations from K. Sieja [29]. The experimental data in black dots are from A. C. Larsen et al [2], while the (preliminary) experimental data in grey dots are re-normalised data from the same experiment. Top: The *total* level density is used for the shell model calculations. Bottom: The *partial* level density is used.

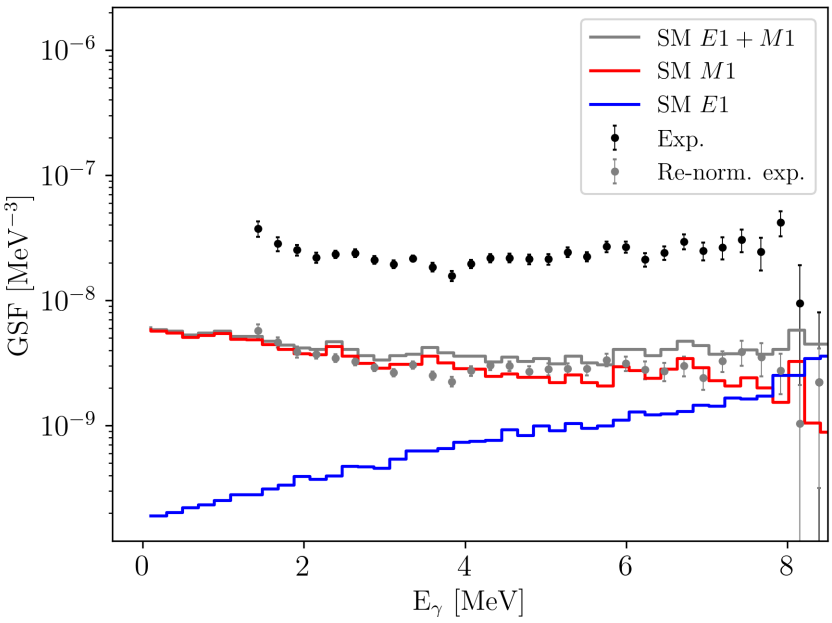

Figure 4.17: The GSF for ^{44}Sc in the GCLSTsdpfsdgix5pn interaction with a $3\hbar\omega$ truncation and 200 levels for each angular momentum $j_i = 0, 1, ..., 8$ for both parities. The experimental data in black dots are from A. C. Larsen et al [2], while the (preliminary) experimental data in grey dots are re-normalised data from the same experiment.

4.4 ^{44}Sc

In fig. 4.17 we see the GSF of ^{44}Sc calculated with a $3\hbar\omega$ truncation and 200 levels for each angular momentum $j_i = 0, 1, ..., 8$ for both parities. Less truncation and more levels have been used here than in the ^{44}Sc analysis in section 4.3, making the calculations considerably larger. Comparing fig. 4.17 and fig. 4.16, we see that there is a noticeable difference in the $E1$ GSF at approximately $E_\gamma > 6$ MeV. In the larger calculation, the $E1$ GSF steadily increases across the entire gamma energy range and it seems to surpass the $M1$ GSF at approximately 8 MeV, while for the smaller calculation, the $E1$ GSF decreases from $E_\gamma = 6$ MeV and above.

Recall the different truncations of the two calculations which are $1\hbar\omega$ and $3\hbar\omega$ for the smallest and the largest calculation respectively. Recall also that the $E1$ GSF is caused by transitions where $\pi_i \neq \pi_f$. Parity changing transitions are caused by $\hbar\omega$ excitations (also called major shell excitations), and increasing the number of nucleons which are allowed to be excited across a major shell from 1 to 3 thus has an impact on the $E1$ GSF. This is exactly what we see in the two figures. The larger calculation allows for 79227 $E1$ and 199890 $M1$ transitions, compared to the smaller calculation with 43446 $E1$ and 62221 $M1$ transitions. Note that many levels (and hence transitions) are excluded from the GSF calculations because levels in the

discrete region and levels above the neutron separation energy are removed. The aforementioned numbers of transitions are however the actual number of transitions included in the calculations, and we see that the significant increase in the number of $E1$ transitions has a large impact on the calculated $E1$ GSF. Curiously, the $M1$ GSF is not largely impacted except for a slight decrease in its fluctuations for the larger calculation; the overall shape and amplitude is unchanged despite there being over three times as many $M1$ transitions in the larger calculation.

The LEE of ^{44}Sc is unaffected by the increase in transitions since the only noticeable change happens at gamma energies much greater than the LEE. However, the larger calculations are still valuable to our understanding of the LEE because we see that the $E1$ GSF is affected by the increased number of transitions but the LEE is not a part of the affected area. This is a good indication that it is indeed only the $M1$ transitions which cause the LEE.

4.5 ^{50,51}V

It is important to choose an interaction which is suitable to the problem at hand. The nucleus ^{50}V has 3 protons and 7 neutrons filling the $1f_{7/2}$ orbitals. We see from fig. 2.7 that the GXPF1A interaction might be a suitable choice, locking all the orbitals below $1f_{7/2}$ in a ^{40}Ca core. The SDPF-MU interaction is also a suitable choice with its much larger $sdpf$ model space with an ^{16}O core.

We see in table 4.1 that both interactions have a very manageable $m = 0$ scheme dimension of 7.02×10^6 for the positive parity levels, which is well within the capability of a supercomputer like Betzy. SDPF-MU has to be heavily truncated to be manageable, and I have given it a $1\hbar\omega$ truncation which means that only a single nucleon is allowed to be excited across the major shell gap. Due to the parity of the pf orbitals, a single nucleon excited from sd to pf will only contribute to the negative parity levels and hence GXPF1A and SDPF-MU has the exact same positive parity dimensionality. If I were to perform a $2\hbar\omega$ truncation instead, two nucleons would be allowed to cross the major shell gap and would contribute to the positive parity levels. The positive parity $m = 0$ scheme dimensionality would then be 1.26×10^{10} which is at the very limit of what is possible with today's supercomputers[5]. From table 4.1 we see that the number of levels per j (the j scheme dimension) is in the order of 10^5 for $j = 0, 1, ..., 8$ which means that these interactions are able to supply much more than the few hundreds of levels which is required to calculate the GSF for transition energies $E_\gamma < 10$ MeV. GXPF1A has a large disadvantage in that it cannot provide $E1$ transitions[6]. SDPF-MU on the other hand spans two major shells making $E1$ transitions possible within its model space.

[5] See for example [43] where ^{32}Mg was calculated in the $sdpf$ model space with an $8\hbar\omega$ truncation, yielding an m-scheme dimension of $\approx 10^{11}$.

[6] The p and f orbitals are both of negative parity which means that GXPF1A can only supply either positive or negative parity levels for even and odd nuclei respectively, which in turn means that no $E1$ transitions will be possible within GXPF1A.

m or j	m dim	j dim
8	1.99×10^6	5.87×10^5
7	2.69×10^6	7.04×10^5
6	3.49×10^6	7.95×10^5
5	4.33×10^6	8.42×10^5
4	5.16×10^6	8.29×10^5
3	5.91×10^6	7.47×10^5
2	6.50×10^6	5.95×10^5
1	6.89×10^6	3.84×10^5
0	7.02×10^6	1.33×10^5

Table 4.1: The few lowest m and j scheme dimensions of ^{50}V in the GXPF1A and SDPF-MU interactions. Note that this is the positive dimensionality of SDPF-MU and that it has a $1\hbar\omega$ truncation. GXPF1A is not truncated.

Let us now see how GXPF1A fares against SDPF-MU. In the top left plot of fig. 4.18 we see the $M1$ GSF of ^{50}V with both interactions. Both interactions are used to calculate 200 levels for each $j^\pi = 0^+, 1^+, ..., 8^+$. GXPF1A has no truncation while SDPF-MU has a truncation of $1\hbar\omega$. The GSF of both interactions clearly follow the same trend; there is a downward slope at $E_\gamma = [0, 3]$ MeV, a minimum spanning $E_\gamma = [3, 7]$ MeV, and an increase beyond 7 MeV. While both interactions perform similarly to each other, they follow the trend of the experimental data only for the low and high energy regimes. The experimental data reaches a minimum at $E_\gamma \approx 4$ MeV and quickly starts to increase, while the shell model calculations of both interactions stay low for several MeVs before they display an increase.

The same analysis for ^{51}V is displayed in the top right plot. Both interactions follow each other closely, starting with a downward slope, a minimum spanning the middle energy range, a small dip just before 8 MeV, and ending with an increase in the high energy range. The $M1$ GSF seems to follow the trend of the experimental data a bit better for ^{51}V than for ^{50}V, though the distance between the experimental and shell model GSF is greater for ^{51}V. In particular, the small dip in the experimental data at just under 8 MeV does register in the shell model GSF for both interactions. With only the experimental data to judge I would be very careful to attribute this small dip any physical meaning of the GSF, but rather to a statistical variation in the data. However, since we see the dip clearly in the shell model calculations as well, the small dip might actually have physical significance.

Note that each row of plots in fig. 4.18 share y axis for easy comparison. The experimental GSFs of ^{50}V and ^{51}V, though somewhat differing in shape, are of very similar magnitude. Note also that the shell model GSFs are strikingly similar, save for the small drop just below 8 MeV for ^{51}V.

In the middle plots of fig. 4.18 we see the relative difference in the GSF between the two interactions for both ^{50}V and ^{51}V. The difference is relatively stable for both isotopes, hovering around 10% for most of the energy range. It is of no surprise that GXPF1A and SDPF-MU when matched to the same positive parity dimensionality performs similarly, since SDPF-MU

was created by a combination of USD and GXPF1B. GXPF1B is a tuning of GXPF1A where five two-body matrix elements and the single particle energies of $2p_{1/2}$ are changed. These differences should lead to no notable changes in the results [38], and we indeed see from fig. 4.18 that the difference between the two interactions is small for both isotopes.

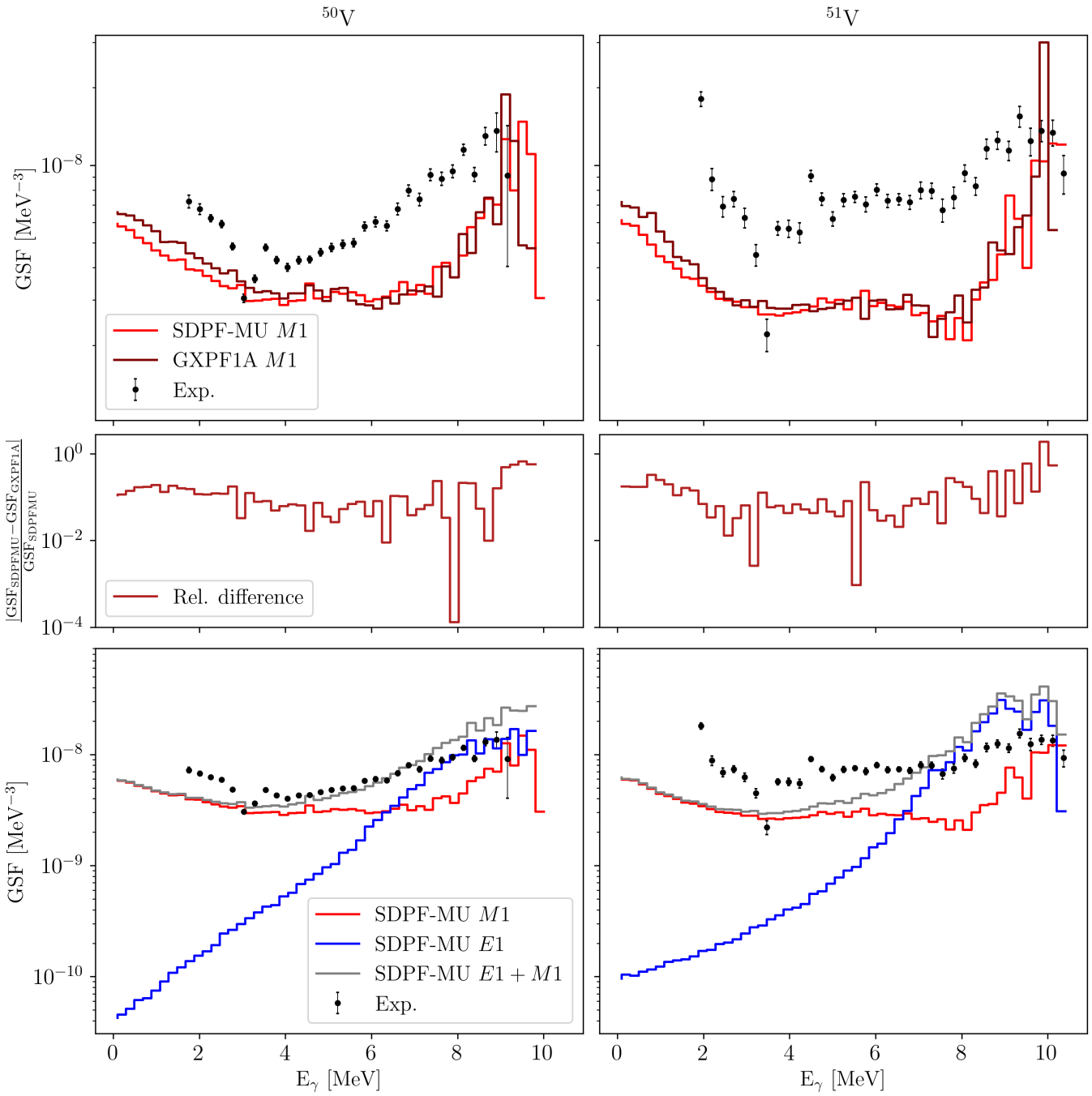

Figure 4.18: Top: The $M1$ GSF calculated with GXPF1A and SDPF-MU. GXPF1A is not truncated. Middle: The absolute difference between the $M1$ GSFs of GXPF1A and SDPF-MU normalised to the SDPF-MU GSF. Bottom: The dipole GSF calculated with the SDPF-MU interaction truncated to $1\hbar\omega$, for both ^{50}V and ^{51}V. Note that each row of plots share y axis for easy comparison. Calculations for both interactions include 200 levels (of both parities for SDPF-MU) for angular momenta $j = 0, 1, ..., 8$. Experimental data from A. C. Larsen et al. [3].

Let us now consider the total dipole GSF for ^{50}V which is shown in the lower left plot in fig. 4.18. The $E1$ GSF is included (blue) to create the total dipole GSF (grey). The inclusion of $E1$ transitions has a negligible impact on the total GSF at approximately $E_\gamma = [0, 2]$ MeV, where we see that the $E1$ GSF is more than two orders of magnitude lower than its $M1$ partner. The $E1$ GSF rises exponentially across the entire gamma energy range and for $E_\gamma > 2$ MeV its contribution to the total GSF is noticeable. At $E_\gamma > 6.5$ MeV the $E1$ GSF starts to dominate the $M1$ GSF and keeps doing so for the rest of the energy range. This domination might be changing at the end of the energy range, but we recall that the shell model GSF at the highest energies is prone to large fluctuations due to a lack of levels, as discussed in section 4.2. We must therefore be careful when interpreting the GSF at the highest energies. It is of particular interest that the $E1$ transitions have a negligible contribution to the low energy enhancement which consequently is only caused by the $M1$ transitions.

The inclusion of $E1$ transitions helps bridging the gap to the experimental data. We see that $E_\gamma \approx 4$ MeV is a turning point in the experimental GSF which the shell model $M1$ GSF is not able to reproduce. While still not perfect, the $E1$ GSF does contribute to the total GSF to reproduce this behaviour. The inclusion of $E1$ does however make the total shell model GSF overshoot the experimental values beyond $E_\gamma = 6.2$ MeV, but note that the data normalisation of the experimental data in the Oslo method has a large uncertainty.

The total dipole GSF of ^{51}V is displayed in the lower right plot of fig. 4.18. The $E1$ GSF starts at a bit less than two orders of magnitude below the $M1$ and like for ^{50}V has a negligible impact on the total GSF at approximately $E_\gamma = [0, 2]$ MeV. The $E1$ GSF seems to grow "doubly exponential" (exponential growth in a log plot) and has a noticeable contribution to the total beyond 2 MeV. From 6 MeV and above, $E1$ grows larger than $M1$ and stays so for the rest of the energy range. As for ^{50}V, we see here that $E1$ might start to dip below $M1$ at energies beyond 10 MeV, but again, the shell model GSF at the highest energies must be taken with a grain of salt. The $E1$ transitions help reproduce the experimental data but do overshoot at the highest energies. Also for ^{51}V we see that the low energy enhancement is almost entirely caused by the $M1$ transitions.

Note that the $E1$ GSF of ^{51}V starts at a factor of 5 to 6 higher than the $E1$ GSF of ^{50}V. This discrepancy might not be of a physical nature, but rather because of too few $E1$ values in the ^{50}V calculations as mentioned in section 4.1. I am currently running new ^{50}V calculations to investigate this issue.

4.6 ^{64}Zn

In fig. 4.19 we see the GSF of ^{64}Zn in the gs8 interaction with a $1\hbar\omega$ truncation, which is one of the heaviest nuclei to ever be calculated with the shell model. 200 levels have been used for both parities for each $j = 0, 1, ..., 8$. The total dipole GSF (grey) starts with a low energy enhancement in the

interval $E_\gamma = [0, 2]$ MeV. From 2 MeV there is a slight rise in the GSF up to 4.5 MeV where there is a sharp increase which gradually flattens out up to 10 MeV. The low energy enhancement is dominated by the $M1$ GSF (red) with a negligible contribution by its $E1$ partner (blue). At 4.5 MeV, where the total dipole GSF starts to rapidly increase, we see that the $E1$ contribution starts to dominate $M1$. $E1$ stays higher than $M1$ for the rest of the energy range, except for a few points at the highest energies, though this is likely caused by too few transitions to smooth out the GSF in the high energy range and not actually that $E1$ dips below $M1$. This behaviour is discussed in section 4.2. However, we do see that the slope of the $E1$ GSF decreases and almost flattens out at 10 MeV, while $M1$ is increasing in the same interval. If these trends continue, $E1$ and $M1$ will intersect above 10 MeV.

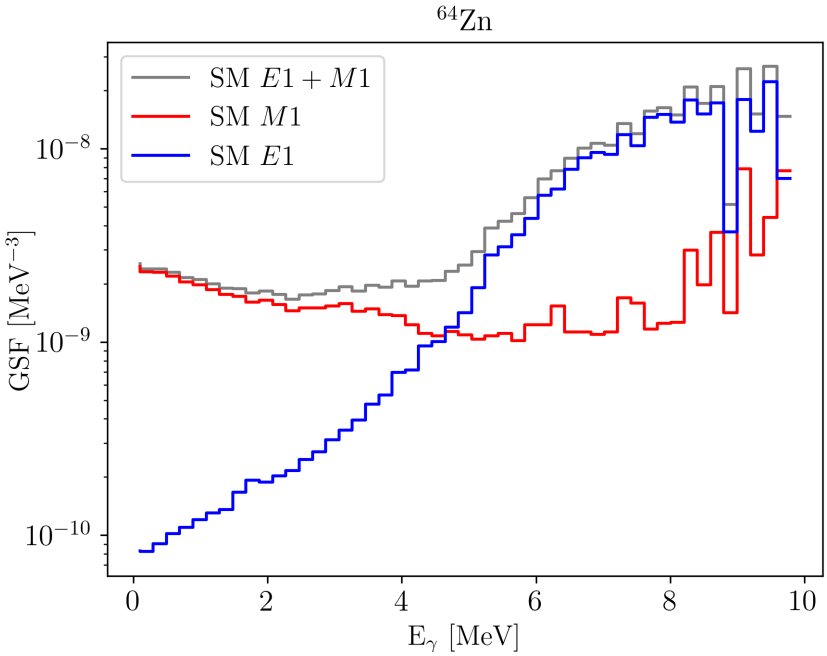

Figure 4.19: The GSF of ^{64}Zn calculated with the gs8 interaction with $1\hbar\omega$ truncation and a minimum occupation of 14 nucleons in the $1f_{7/2}$ orbitals (protons and neutrons combined). 200 levels for both parities for each $j = 0, 1, ..., 8$ have been used.

Chapter 5

Conclusions and outlook

5.1 Conclusions and outlook

In this thesis, large-scale shell model calculations were performed to calculate the gamma strength function (GSF) of ^{44}Sc, ^{50,51}V, and ^{64}Zn. Because of the supercomputer Betzy, and because of the highly parallelisable nuclear shell model solver KSHELL, these nuclei have been calculated with larger model spaces and larger numbers of energy levels and transitions probabilities than ever before. The large number of transition probabilities is several hundred thousands for each of the nuclei and it has opened the possibility for statistical analyses of the calculations. The shell model calculations of this work have proven to be a valuable supplement to existing experimental GSF data for ^{44}Sc, ^{50,51}V, particularly in helping us understand the low energy enhancement (LEE) which has been seen experimentally in all three nuclei. In addition, $E1$ and $M1$ GSFs for ^{64}Zn are calculated for the fist time within the shell model framework. These are to be compared to experimental data from the Oslo Cyclotron Laboratory which are currently being analysed. In all cases, the shell model calculations of this work show that the LEE is is due to $M1$ transitions, not $E1$ transitions, which confirms K. Sieja's results [29].

The large number of (reduced) transition probabilities (B values) from the shell model calculations of this work has made it possible to study the applicability of the generalised Brink-Axel hypothesis (gBA). There have been enough B values to calculate GSFs and B value distributions for individual angular momenta (j_i) and excitation energy (E_i) selections. From these calculations we have seen that the individual j_i GSFs generally show relatively small fluctuations for all nuclei, except at the highest gamma energies. The small fluctuations support the GSF's independence on angular momentum, since we can clearly see that all the individual j_i GSFs closely follow the same trend. The cause of the large fluctuations at high gamma energies can be traced to where the calculated nuclear level density (NLD) stops rising exponentially and starts to decrease; this consequently leads to a decrease in the number of high gamma energy transition probabilities which are needed for the averaging in the GSF calculations, thus making the GSF fluctuate more and more as the number of B values decrease. However,

these large fluctuations do not necessarily disprove the validity of the gBA hypothesis, because large fluctuations might be statistically expected with a low number of B values.

Most of the B distributions clearly resemble the Porter-Thomas distribution, particularly from the selections of E_i values. However, there are some curious deviations from the Porter-Thomas distribution most prominent in the j_i selections and clearest for the $B(E1)$ values. When looking at the relative difference between the B distributions and the Porter-Thomas distribution, there are distinct banana shapes visible for the $B(E1)$ values for most of the isotopes. It looks like a systematic error which might originate from the data analysis and / or the KSHELL software, or it might be of physical nature. Since the banana shapes are most prominent in the $B(E1)$ values, there is reason to believe that the choice of $\hbar\omega$ truncation might be a key factor, since $\hbar\omega$ excitations produce the $E1$ transitions. Comparing calculations of different $\hbar\omega$ truncations might reveal the origin of the banana shapes, however, changing the $\hbar\omega$ truncation generally has a huge impact on the dimensionality of the calculations and might demand more computer resources than what is available today, or be too low to yield good results. Changing the truncation of the vanadium calculations from $1\hbar\omega$ to $2\hbar\omega$ produces an m scheme dimensionality of over 10^{10} which might be impossible with the current computational power. Particle-hole truncations must be applied to make $2\hbar\omega$ calculations feasible. Another option is to perform $2\hbar\omega$ calculations on ^{44}Sc which I know is possible since the calculations of this work uses $3\hbar\omega$ for the ^{44}Sc calculations. Yet another option is to perform shell model calculations of an intermediate nucleus, for example ^{48}Ti, and look at different $\hbar\omega$ truncations. An intermediate nucleus might be in a sweet spot with a good m scheme dimension for several choices of $\hbar\omega$ truncation.

As for the other B distributions, the ones from the E_i selections show very good matches to the Porter-Thomas distribution. This substantiates the claim that the fluctuations in the GSFs are so-called Porter-Thomas fluctuations i.e. fluctuations statistically expected from Porter-Thomas distributed values. If this is so, then the gBA is indeed applicable to the shell model calculations of this work.

The GSFs of this work have been compared to experimental Oslo method GSFs for the nuclei ^{44}Sc, ^{50,51}V. Extra attention was given to ^{44}Sc because of a suspected error in the normalisation of the Oslo method data which made the experimental GSF of ^{44}Sc much larger than the experimental GSFs of ^{50,51}V. The calculations of this work gave a ^{44}Sc GSF of 5 to 10 times lower amplitude than the experimental GSF, supporting the suspicion that the experimental GSF was incorrectly normalised. In addition, shell model calculations performed by K. Sieja show a good fit to the experimental GSF of ^{44}Sc [29]; by replicating Sieja's shell model parameters, this work showed it is likely that Sieja used the *total* NLD instead of the *partial* NLD in her GSF calculations which gives an artificial scaling of the GSF.

The calculated GSFs of ^{50,51}V show good fits to experimental data. In particular, the calculations reproduced the LEE which was seen in both nuclei experimentally [3], and the calculations show without a doubt that

the LEE is caused by $M1$ transitions. The E or M nature of the LEE has no clear experimental conclusion, though an experiment by Jones et. al. has a small bias towards $M1$ transitions [27]. Uncovering the origin of the LEE is of relevance to astrophysical applications, since the LEE tells us that some nuclei have an enhanced probability of decaying by low energy gamma rays which indeed might affect astrophysical reaction rates. To our knowledge, the shell model calculations of this work are to date the largest calculations ever performed on ^{50,51}V.

This work has shown that choosing a large number of levels per $j_i^{\pi_i}$ in the shell model calculations is important for the resulting GSF, particularly at the highest gamma energies. A correspondence between fluctuations in the GSF and where the accompanying NLD stops rising exponentially and starts to decrease is clearly seen. It might be a good idea to non-evenly distribute the number of levels calculated across angular momenta instead of calculating 200 levels per $j_i^{\pi_i}$ to get rid of the "wasted" levels.

If there is one certain conclusion from this work, it is the fact that further investigation is needed to make a thorough statistical analysis of the GSF. A more thorough statistical analysis will be of great help in the study of the gBA hypothesis, something which is of great interest to anyone who uses the GSF, and in particular to those who use the Oslo method. I have added some additional thoughts and proposal for future work on gBA testing in appendix C.

Appendix A

Additional tables and figures

Interaction	Range	Model space	Core	$g_{s,p}, g_{s,n}$	g_s quench	
USDA	[^{17}O, ^{39}Ca]	sd	^{16}O	(5.585, -3.826)	1	[44]
GXPF1A	[^{41}Ca, ^{79}Zr]	pf	^{40}Ca	(5.027, -3.443)	0.9	[37]
JUN45	[^{57}Ni, ^{99}Sn]	$2p_{3/2}, 1f_{5/2}, 2p_{1/2}, 1g_{9/2}$	^{56}Ni	(3.909, -2.678)	0.7	[45]
SDPF-MU	[^{17}O, ^{79}Zr]	sd, pf	^{16}O	(5.027, -3.443)	0.9	[38]
gs8	[^{17}O, ^{139}Yb]	sd, pf, sdg	^{16}O	(4.189, -2.869)	0.75	[36]
GCLSTsdpfsdgix5pn	[^{17}O, ^{139}Yb]	sd, pf, sdg	^{16}O	(4.189, -2.869)	0.75	

Table A.1: The interactions used in this work. The range column denotes the smallest and largest possible nucleus which the model space can support. Note that the interaction may not be suited for a nucleus even though the nucleus is within the range. $g_{s,p}, g_{s,n}$ are the recommended spin g factors for protons and neutrons respectively. g_s quench is the factor multiplied by $g_{s,\text{free}} = (5.585, -3.826)$ to get the recommended values.

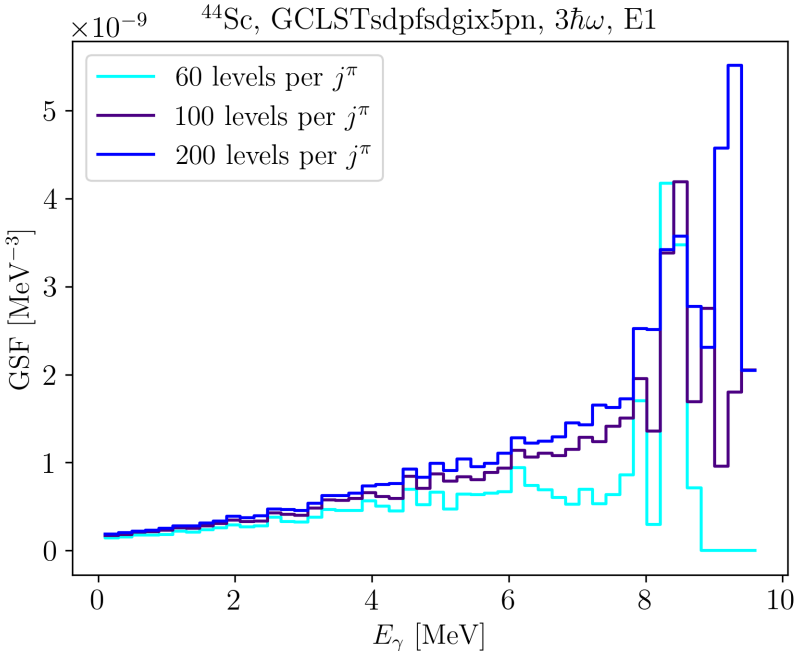

Figure A.1: Same as fig. 4.14 but without logarithmic y axis to better highlight the asymptotic behaviour of the GSF when more levels are included in the shell model calculation.

Appendix B

How kshell-utilities scales B distributions to the Porter-Thomas distribution

Let b_0 be the value of the first non-normalised bin in a B distribution, and let p_0 be the value of the Porter-Thomas distribution at the same bin value. I want to scale b_0 so that it is equal to p_0, namely that

$$b_0 x = p_0, \tag{B.1}$$

where x is the scaling factor. I then want to scale all the B distribution values with the same scaling factor x. However, due to statistical fluctuations, I expect that the B distribution values do not perfectly match the Porter-Thomas distribution, and if that is indeed true then using just a single value b_0 from the B distribution might scale the distribution incorrectly. By trial and error I found that using an average scaling factor

$$x = \frac{1}{20} \sum_{i=1}^{20} \frac{p_i}{b_i} \tag{B.2}$$

produces a usable scaling factor across all KSHELL calculations in this work. Note that i starts at 1 and that the 0th value is excluded. This is because the Porter-Thomas distribution goes to infinity as $B/\langle B \rangle \to 0^+$ resulting in an unpredictable scaling factor for the first bin value. I chose 20 values because all KSHELL calculations in this work yield B distributions with non-zero values for at least the 21 first bins. This ad hoc way of scaling the distributions might result in systematic errors, and it might be fruitful to rethink how this scaling is performed. Maybe draw N random values from the distribution which is then used in the average scaling factor x? Further study is needed to draw any conclusions. The specific line of code where the scaling happens can be found here: https://github.com/GaffaSnobb/kshell-utilities/blob/2c4b9de7974e21fbc2975ff116ce5ebbe1fad57a/kshell_utilities/general_utilities.py#L1105.

Appendix C

Additional thoughts on testing the gBA hypothesis

When expressing the GSF solely as a function of gamma energy, we assume that

$$f(E_\gamma) \approx f(E_\gamma, E_i, j_i, \pi_i) \tag{C.1}$$

which is to say that the GSF is approximately independent on our choice of initial excitation energy, total angular momentum, and parity. This assumption is called the generalised Brink-Axel hypothesis (gBA) and does not hold for all nuclei under all circumstances (see section 2.4.3 for details). I propose an extension to this thesis where the goal is to create a tool in the `kshell-utilities` Python package which checks the validity of the gBA for any data generated by KSHELL. I have started the work already, but the task proved to demand more time than what I have for my masters thesis which is why I present the unfinished work here in the appendix, with suggestions on how to continue the work:

The decay widths in eq. (2.43) give information about the lifetime of the excited levels and consequently information about the probability that the excited levels will decay, through the relation

$$\Gamma \propto B. \tag{C.2}$$

Due to the statistical nature of lifetimes and decay we are motivated to study the distribution of the decay widths, from which we might get important insight to the characteristics of the decays. In their 1956 paper, Porter and Thomas found strong evidence that certain neutron *reduced* widths normalised to their average follow a χ^2 distribution of one degree of freedom [19]. We see from the relation in eq. (C.2) that B will follow the same distribution as Γ since the proportionality factor will be divided to 1 in the normalisation. Thus, if Porter and Thomas' theory is true, then

$$y = \frac{B(Xj_\gamma)}{\langle B(Xj_\gamma)\rangle} \sim \chi^2_1. \tag{C.3}$$

The χ^2 distribution with ν degrees of freedom (denoted χ^2_ν) is the distribution of a sum of the squares of ν independent standard normal random variables

$Z_1, ..., Z_\nu$, namely

$$Q = \sum_{i=1}^{\nu} Z_i^2, \tag{C.4}$$
$$Q \sim \chi^2_\nu.$$

The χ^2 distribution with one degree of freedom is also called the *Porter-Thomas distribution*. For eq. (C.3) to be true, $\sqrt{y}$ must be a standard normal random variable and all values $\sqrt{y}$ must be independent of each other, which is to say that all values B must be independent of each other. The former might be hard to show if we start with B values since all negative signs are lost in the squaring, but I have included an attempt at recreating the standard normal distribution of $\sqrt{y}$ from B values in appendix D.

I have already implemented checks of the distribution of B values in `kshell-utilities` – a result of this check for ^{44}Sc is seen in fig. C.1 – which can easily be generated for any KSHELL data set by `res.porter_thomas_Ei_plot()` (see section 3.2 for details). The top plot shows the distribution of calculated B values at certain initial excitation energies (within a bin), while the middle plot shows the distribution of calculated B values within the indicated initial excitation energy intervals. In both plots the χ^2_1 distribution is shown in green and we see that all the calculated distributions follow the theoretical χ^2_1 distribution very well. In the bottom plot of fig. C.1 we see relative differences from the distributions in the middle plot to the theoretical χ^2_1 distribution.

If we assume that eq. (C.3) is true, then we can also assume that $\sqrt{y}$ is standard normal distributed. This consequently means that if we add n values of y together, the sum will have a χ^2 distribution of $\nu = n$,

$$Y = \sum_{i=1}^{n} y_i, \tag{C.5}$$
$$Y \sim \chi^2_n.$$

I believe that the next step is to explore the fact that the GSF, from its definition in eq. (2.43), is a sum of B values, values whose square roots are standard normal distributed. From this I might be able to derive the underlying distribution of the GSF.

Lets for simplicity assume that calculating the GSF for some choice of $E_\gamma, E_i, j_i, \pi_i$ involves only one B value. Will then the distribution of $f(E_\gamma)$ follow the χ^2_1 distribution? We might have messed up the required randomness if we choose initial energy, angular momentum and parity first. We do however know that calculating $f(E_\gamma)$ involves more than a single B value since the GSF is evaluated in an initial excitation energy bin. This fact leads to yet another problem which is that a given bin size of ΔE certainly does not contain the same number of B values when evaluated at different excitation energies. From the definition of the χ^2 distribution we have that ν degrees of freedom means that ν squared standard normal random variables are added together. Is it possible to make any meaningful statistical analysis if ν varies slightly? What if ν varies wildly? One solution might be to select

only m B values where m is the number of B values in the initial excitation energy bin with fewest B values.

The point of the aforementioned statistical analysis is to assess whether the gBA holds or not. Several papers have already used Porter-Thomas to evaluate the validity of the gBA hypothesis, see for example [46, 47, 48], but it is not entirely clear to me why their calculations are valid and what approach they used to get their results. One equation used in the aforementioned papers – which has cost me many late evenings of thinking and pondering – is

$$r = \sqrt{2/\nu}, \tag{C.6}$$

which is a measurement of fluctuations of the χ^2_ν distribution. This expression is presented in Porter and Thomas' 1956 paper eq. (13b) [19] and was in fact derived by Subrahmanyan Chandrasekhar, see appendix IV in [49]. I have yet to figure out exactly how eq. (C.6) is applicable to the GSF and the aforementioned sources have not been able to convince me.

And now to the use case of the Porter-Thomas analysis which brings us to Brink and Axel. By averaging the GSF over initial energies, total angular momenta, and parities, we can look at the GSF as a function of only E_γ which makes the GSF much easier to visualise and to interpret. But is it correct to perform these averages? By doing so, we are effectively stating that

$$f(E_\gamma) \approx f(E_\gamma, E_i, j_i, \pi_i), \tag{C.7}$$

which is to say that the GSF calculated at some choice of E_i, j_i, π_i should be approximately equal to the GSF calculated at some other choice of E_i, j_i, π_i. This is exactly what the generalised Brink-Axel hypothesis states. See section 2.4.3 for references and examples.

The gBA hypothesis is not applicable to all nuclei under all circumstances. All calculations should therefore be tested before the assumptions of gBA are made. There are several ways to approach the problem of testing the gBA hypothesis, with the general idea of calculating the GSF for different values of E_i, j_i, π_i, for then to see how much they differ from each other. One approach is to average over E_i and π_i and calculate one GSF for each different angular momentum

$$f(E_\gamma, j_i) = \frac{1}{N_{E_i} N_{\pi_i}} \sum_{E_i, \pi_i} f(E_\gamma, E_i, j_i, \pi_i). \tag{C.8}$$

This is the approach I use for the calculations in this work. We then need a good way of comparing the different GSFs and we need a way to decide what is considered an acceptable amount of difference between them. In fig. 4.1 we see in grey eq. (C.8) for $j = 0, 1, ..., 8$. In black we see the GSF as only a function of E_γ which is the average over all the grey graphs. There is little doubt that the GSF for each individual j_i all hover around their average, but I want to do better than by-eye measurements. What is considered an acceptable amount of difference between the GSFs for different j_i? If I

figure out the underlying distribution of the GSF, then I can extract the statistically expected fluctuations and decide whether the grey graphs in fig. 4.1 fluctuate as expected or not. If they are expected, great! If not, something else is causing differences in the GSFs which consequently means that the gBA hypothesis is not applicable.

To make a thorough testing of the gBA hypothesis, I should also compare GSFs of different E_i and π_i, not just j_i. I have started the work of making the E_i analysis corresponding to the j_i analysis in figures 4.1 and 4.2, but it is not yet complete. So far I have fig. C.1 where we see distributions from different selections of initial excitation energy values for ^{44}Sc. Note that this figure is purposefully made to be as equal as possible to fig. 3.3 in J. Midtbø's PhD thesis [12]. In the top plot the selections are from specific E_i values, or more precisely, from bins around specific E_i values because the number of B values at an exact E_i is usually zero which will yield very boring distributions. The distribution for all E_i values seems to closely follow the χ^2_1 distribution (in green), though $E_i = 9.7 \pm 0.1$ MeV seems to match χ^2_1 best of the three. The number of B values included in the distributions of $E_i = 5, 7.35, 9.7$ MeV are 674, 7766 and 44072 respectively which is a likely explanation for why the $E_i = 9.7$ MeV distribution most closely follows the χ^2_1 distribution. The number of B values is expected to increase with increasing E_i since level density increases with increasing E_i. More levels means more possible transitions and consequently more B values. In the middle plot of fig. C.1 the selections are from ranges of E_i values, with the accompanying bottom plot which shows the relative difference between the distributions and the theoretical χ^2_1 distribution. The number of B values included in the distributions are 7026, 30838 and 110557 from the lowest to highest energy interval respectively. Here we also see that the distributions closely follows the χ^2_1 distribution and that a larger number of B values yields a closer match. The E_i analysis tells a story almost identical to the j_i analysis.

Given that I figure out an expression for the expected fluctuation in the GSF, I can easily implement the expression in the `kshell-utilities` package making it very simple for anyone who uses KSHELL to test their calculations. For all subsequent uses of KSHELL one will only need to execute a few lines of code to check the validity of the gBA hypothesis, and I believe this can be a very useful tool.

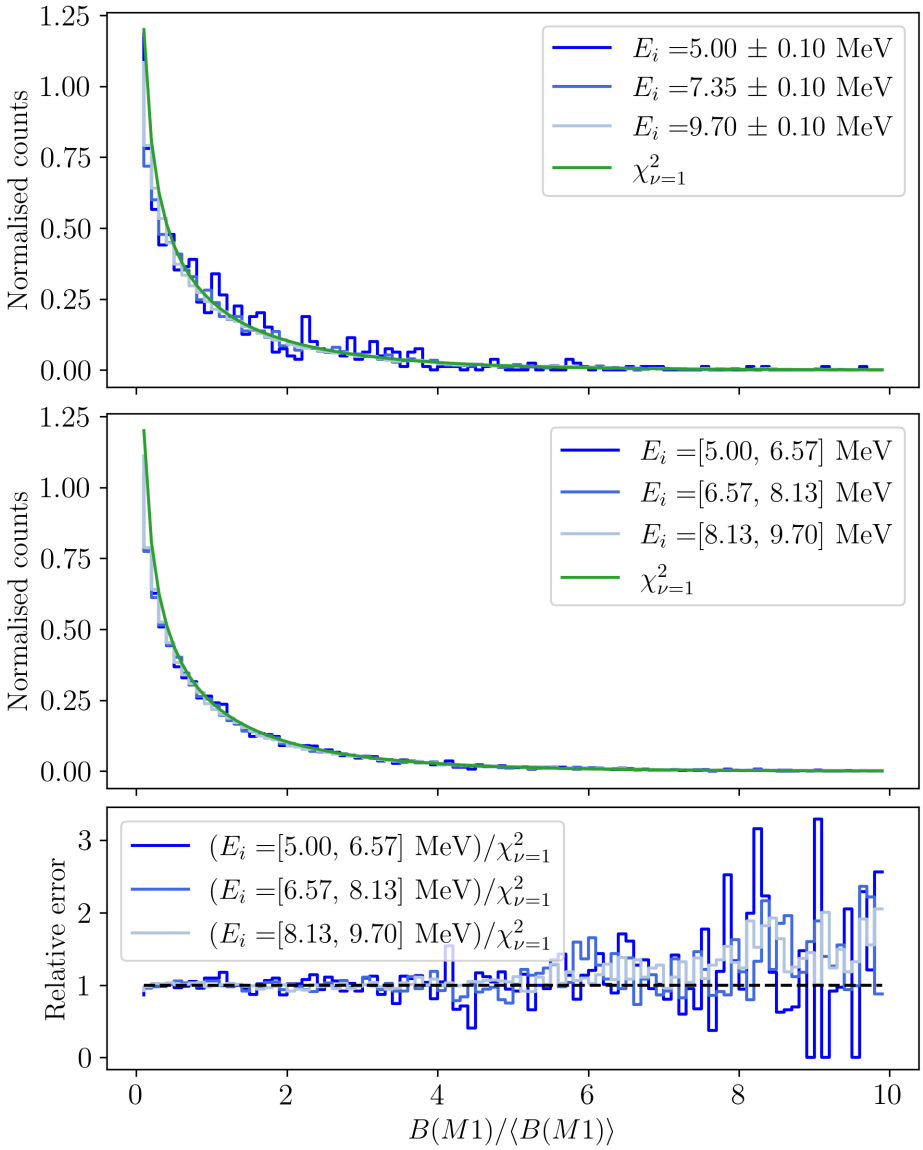

Figure C.1: The distribution of calculated $B(M1)$ values of ^{44}Sc in the GCLSTsdpfsdgix5pn interaction, both parities are included. The top plot shows the distribution of a selection of B values for specific initial excitation energies (within a bin), normalised to match the χ^2_1 distribution. The middle plot shows the distribution of a selection of B values for the indicated initial excitation ranges, also normalised to match the χ^2_1 distribution. The bottom plot shows the deviation of distributions from the middle plot from the χ^2_1 distribution. The procedure and visualisation is reverse engineered from fig. 3.3 in [12].

Appendix D

From χ^2_1 to $\mathcal{N}(0,1)$

In 1956, following the work of Hughes and Harvey [50], Porter and Thomas found strong evidence that the neutron reduced widths (and hence the reduced transition probabilities, see section 2.4.2 for details) of 20 different nuclides [51] normalised to their average, follow a χ^2 distribution of one degree of freedom [19]. Since the χ^2 distribution of ν degrees of freedom is the distribution of ν independent standard normal random variables, and $\nu = 1$ in this case, one could be tempted to check that

$$\begin{aligned} y &= \frac{B(Xj_\gamma)}{\langle B(Xj_\gamma)\rangle} \\ \sqrt{y} &\sim \mathcal{N}(0,1) \end{aligned} \tag{D.1}$$

is indeed true. The keen-eyed of you may have noticed a problem with the square root, that all negative signs are lost when squaring $\sqrt{y}$. Just for the sake of having a bit of fun, one could draw half of the values in y at random and flip their signs at an attempt to replicate the standard normal distribution.

In the code below I use `kshell-utilities`[40] to read the $B(M1)$ values of ^{44}Sc from a summary file generated by KSHELL[1]. I divide them by their mean and take the square root. I then draw half of the values at random and change their sign. And would you know, I get a standard deviation and mean value of

$$\begin{aligned} \sigma &= 0.9999986963963795, \\ \mu &= -0.001614684347519719, \end{aligned} \tag{D.2}$$

which are pretty close to 1 and 0, and a histogram of the values in fig. D.1 which looks very normal!

```
import numpy as np
import matplotlib.pyplot as plt
import kshell_utilities as ksutil
np.random.seed(1337)

res = ksutil.loadtxt(
    path = "Sc44/sdpf-sdg/200_levels/3hw/
    summary_Sc44_GCLSTsdpfsdgix5pn.txt",
```

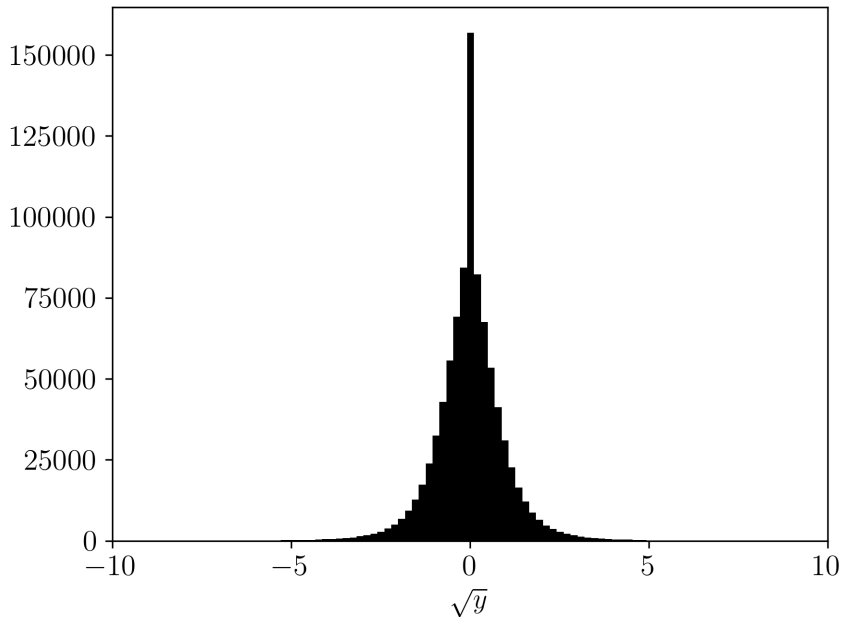

Figure D.1: A histogram of the root of the reduced transition probabilities normalised to their mean value, eq. (D.1), with half of the values drawn at random have had their sign flipped. $B(M1)$ values of ^{44}Sc in the GCLSTsdpfsdgix5pn interaction with a $1\hbar\omega$ truncation and 200 levels for both parities of each $j = 0, 1, ..., 8$.

```
)[0]

BM1 = res.transitions_BM1[:, 9]
y = BM1/np.mean(BM1)
y_root = np.sqrt(y)

n_transitions = len(BM1)
random_indices = np.random.choice(
    a = n_transitions,
    size = int(n_transitions/2),
    replace = False,
)
y_root[random_indices] = -1*y_root[random_indices]

print(f"{np.std(y_root) = }")
print(f"{np.mean(y_root) = }")

plt.hist(y_root, bins=200, color="black")
plt.xlabel(r"$\sqrt{y}$")
plt.xlim([-10, 10])
plt.show()

```

Bibliography

1. Shimizu N, Mizusaki T, Utsuno Y and Tsunoda Y. Thick-restart block Lanczos method for large-scale shell-model calculations. Computer Physics Communications 2019; 244:372–84. DOI: https://doi.org/10.1016/j.cpc.2019.06.011
2. Larsen AC, Guttormsen M, Chankova R, Ingebretsen F, Lönnroth T, Messelt S, Rekstad J, Schiller A, Siem S, Syed NUH and Voinov A. Nuclear level densities and γ-ray strength functions in ^{44,45}Sc. Phys. Rev. C 2007; 76(4):044303. DOI: 10.1103/PhysRevC.76.044303
3. Larsen AC, Chankova R, Guttormsen M, Ingebretsen F, Messelt S, Rekstad J, Siem S, Syed NUH, Ødegård SW, Lönnroth T, Schiller A and Voinov A. Microcanonical entropies and radiative strength functions of ^{50,51}V. Phys. Rev. C 2006; 73(6):064301. DOI: 10.1103/PhysRevC.73.064301
4. Giulini D. Electron spin or "classically non-describable two-valuedness". Studies in History and Philosophy of Science Part B: Studies in History and Philosophy of Modern Physics 2008; 39:557–78. DOI: https://doi.org/10.1016/j.shpsb.2008.03.005
5. Griffiths DJ and Schroeter DF. Introduction to Quantum Mechanics. 3rd ed. Cambridge University Press, 2018
6. Zettili N. Quantum Mechanics: Concepts and Applications. 2nd ed. Wiley, 2009
7. Griffiths DJ. Introduction to Electrodynamics. 4th ed. Cambridge University Press, 2017
8. Ring P and Schuck P. The Nuclear Many-Body Problem. 1st ed. Springer, 2004
9. Gilbert A and Cameron AGW. A composite nuclear-level density formula with shell corrections. Canadian Journal of Physics 1965; 43:1446–96. DOI: https://doi.org/10.1139/p65-139
10. Junde H, Su H and Dong Y. Nucl. Data Sheets 112, 1513. 2011. Available from: www.nndc.bnl.gov/nudat3/getdataset.jsp?nucleus=56Fe&unc=NDS
11. Storebakken T. Statistical properties of 233U - Investigating the Scissor Resonance of 233U, using GSF and NLD from the Oslo Method analysis with the new OMpy software. MA thesis. University of Oslo, 2021. Available from: http://urn.nb.no/URN:NBN:no-90395

12. Midtbø JE. The low-energy enhancement. An experimental and theoretical study of nuclear level densities and gamma ray strength functions. PhD thesis. University of Oslo, 2019. Available from: http://urn.nb.no/URN:NBN:no-79895

13. Brink DM. Some aspects of the interaction of light with matter. PhD thesis. University of Oxford, 1955. Available from: https://ora.ox.ac.uk/objects/uuid:334ec4a3-8a89-42aa-93f4-2e54d070ee09

14. Bečvář F, Cejnar P, Chrien RE and Kopecký J. Test of photon strength functions by a method of two-step cascades. Phys. Rev. C 1992; 46(4):1276–87. DOI: 10.1103/PhysRevC.46.1276

15. Krtička M, Bečvář F, Honzátko J, Tomandl I, Heil M, Käppeler F, Reifarth R, Voss F and Wisshak K. Evidence for $M1$ Scissors Resonances Built on the Levels in the Quasicontinuum of ^{163}Dy. Phys. Rev. Lett. 2004; 92(17):172501. DOI: 10.1103/PhysRevLett.92.172501

16. Guttormsen M, Larsen AC, Görgen A, Renstrøm T, Siem S, Tornyi TG and Tveten GM. Validity of the Generalized Brink-Axel Hypothesis in ^{238}Np. Phys. Rev. Lett. 2016; 116(1):012502. DOI: 10.1103/PhysRevLett.116.012502

17. Bracco A, Camera F, Mattiuzzi M, Million B, Pignanelli M, Gaardhøje JJ, Maj A, Ramsøy T, Tveter T and Źelazny Z. Increase in Width of the Giant Dipole Resonance in Hot Nuclei: Shape Change or Collisional Damping? Phys. Rev. Lett. 1995; 74(19):3748–51. DOI: 10.1103/PhysRevLett.74.3748

18. Devore J and Berk K. Modern Mathematical Statistics with Applications. 2nd ed. Springer International Publishing, 2018

19. Porter CE and Thomas RG. Fluctuations of Nuclear Reaction Widths. Phys. Rev. 1956; 104(2):483–91. DOI: 10.1103/PhysRev.104.483

20. Guttormsen M, Chankova R, Agvaanluvsan U, Algin E, Bernstein LA, Ingebretsen F, Lönnroth T, Messelt S, Mitchell GE, Rekstad J, Schiller A, Siem S, Sunde AC, Voinov A and Ødegård S. Radiative strength functions in $^{93-98}$Mo. Phys. Rev. C 2005; 71(4):044307. DOI: 10.1103/PhysRevC.71.044307

21. Simon A, Guttormsen M, Larsen AC, Beausang CW, Humby P, Harke JT, Casperson RJ, Hughes RO, Ross TJ, Allmond JM, Chyzh R, Dag M, Koglin J, McCleskey E, McCleskey M, Ota S and Saastamoinen A. First observation of low-energy γ-ray enhancement in the rare-earth region. Phys. Rev. C 2016; 93(3):034303. DOI: 10.1103/PhysRevC.93.034303

22. Schwengner R, Frauendorf S and Brown BA. Low-Energy Magnetic Dipole Radiation in Open-Shell Nuclei. Phys. Rev. Lett. 2017; 118(9):092502. DOI: 10.1103/PhysRevLett.118.092502

23. Tavukcu E. Level densities and radiative strength functions in 56Fe and 57Fe. PhD thesis. North Carolina State University, 2002

24. Voinov A, Algin E, Agvaanluvsan U, Belgya T, Chankova R, Guttormsen M, Mitchell GE, Rekstad J, Schiller A and Siem S. Large Enhancement of Radiative Strength for Soft Transitions in the Quasicontinuum. Phys. Rev. Lett. 2004; 93(14):142504. DOI: 10.1103/PhysRevLett.93.142504

25. Wiedeking M, Bernstein LA, Krtička M, Bleuel DL, Allmond JM, Basunia MS, Harke JT, Fallon P, Firestone RB, Goldblum BL, Hatarik R, Lake PT, Lee IY, Lesher SR, Paschalis S, Petri M, Phair L and Scielzo ND. Low-Energy Enhancement in the Photon Strength of ^{95}Mo. Phys. Rev. Lett. 2012; 108(16):162503. DOI: 10.1103/PhysRevLett.108.162503

26. Larsen AC, Blasi N, Bracco A, Camera F, Eriksen TK, Görgen A, Guttormsen M, Hagen TW, Leoni S, Million B, Nyhus HT, Renstrøm T, Rose SJ, Ruud IE, Siem S, Tornyi T, Tveten GM, Voinov AV and Wiedeking M. Evidence for the Dipole Nature of the Low-Energy γ Enhancement in ^{56}Fe. Phys. Rev. Lett. 2013; 111(24):242504. DOI: 10.1103/PhysRevLett.111.242504

27. Jones MD, Macchiavelli AO, Wiedeking M, Bernstein LA, Crawford HL, Campbell CM, Clark RM, Cromaz M, Fallon P, Lee IY, Salathe M, Wiens A, Ayangeakaa AD, Bleuel DL, Bottoni S, Carpenter MP, Davids HM, Elson J, Görgen A, Guttormsen M, Janssens RVF, Kinnison JE, Kirsch L, Larsen AC, Lauritsen T, Reviol W, Sarantites DG, Siem S, Voinov AV and Zhu S. Examination of the low-energy enhancement of the γ-ray strength function of ^{56}Fe. Phys. Rev. C 2018; 97(2):024327. DOI: 10.1103/PhysRevC.97.024327

28. Schwengner R, Frauendorf S and Larsen AC. Low-Energy Enhancement of Magnetic Dipole Radiation. Phys. Rev. Lett. 2013; 111(23):232504. DOI: 10.1103/PhysRevLett.111.232504

29. Sieja K. Electric and Magnetic Dipole Strength at Low Energy. Phys. Rev. Lett. 2017; 119(5):052502. DOI: 10.1103/PhysRevLett.119.052502

30. Liddick SN, Larsen AC, Guttormsen M, Spyrou A, Crider BP, Naqvi F, Midtbø JE, Bello Garrote FL, Bleuel DL, Crespo Campo L, Couture A, Dombos AC, Giacoppo F, Görgen A, Hadynska-Klek K, Hagen TW, Ingeberg VW, Kheswa BV, Lewis R, Mosby S, Perdikakis G, Prokop CJ, Quinn SJ, Renstrøm T, Rose SJ, Sahin E, Siem S, Tveten GM, Wiedeking M and Zeiser F. Benchmarking the extraction of statistical neutron capture cross sections on short-lived nuclei for applications using the β-Oslo method. Phys. Rev. C 2019; 100(2):024624. DOI: 10.1103/PhysRevC.100.024624

31. Krane KS. Introductory Nuclear Physics. 3rd ed. Wiley, 1991

32. Woods RD and Saxon DS. Diffuse Surface Optical Model for Nucleon-Nuclei Scattering. Phys. Rev. 1954; 95(2):577–8. DOI: 10.1103/PhysRev.95.577

33. Nilsson SG and Ragnarsson I. Shapes and Shells in Nuclear Structure. 1st ed. Cambridge University Press, 1995

34. Jimin W and Xiaolong H. Nucl. Data Sheets 144, 1. 2017. Available from: www.nndc.bnl.gov/nudat3/getdataset.jsp?nucleus=51V&unc=NDS

35. Chen J and Singh B. Nucl. Data Sheets 157, 1. 2019. Available from: www.nndc.bnl.gov/nudat3/getdataset.jsp?nucleus=50V&unc=NDS

36. Shimizu N, Utsuno Y, Futamura Y, Sakurai T, Mizusaki T and Otsuka T. Stochastic estimation of nuclear level density in the nuclear shell model: An application to parity-dependent level density in 58Ni. Physics Letters B 2016; 753:13–7. DOI: https://doi.org/10.1016/j.physletb.2015.12.005

37. Honma M, Otsuka T, Brown BA and Mizusaki T. Shell-model description of neutron-rich pf-shell nuclei with a new effective interaction GXPF 1. The European Physical Journal A - Hadrons and Nuclei 2005. DOI: 10.1140/epjad/i2005-06-032-2

38. Utsuno Y, Otsuka T, Brown BA, Honma M, Mizusaki T and Shimizu N. Shape transitions in exotic Si and S isotopes and tensor-force-driven Jahn-Teller effect. Phys. Rev. C 2012; 86(5):051301. DOI: 10.1103/PhysRevC.86.051301

39. Midtbø JE and Shimizu N. kshell_public. Available from: https://github.com/jorgenem/kshell_public

40. Dahl JK, Midtbø JE and Shimizu N. kshell-utilities. Available from: https://github.com/GaffaSnobb/kshell-utilities

41. Schiller A, Bergholt L, Guttormsen M, Melby E, Rekstad J and Siem S. Extraction of level density and γ strength function from primary γ spectra. Nuclear Instruments and Methods in Physics Research Section A: Accelerators, Spectrometers, Detectors and Associated Equipment 2000; 447:498–511. DOI: https://doi.org/10.1016/S0168-9002(99)01187-0

42. Caurier E, Martínez-Pinedo G, Nowacki F, Poves A and Zuker AP. The shell model as a unified view of nuclear structure. Rev. Mod. Phys. 2005; 77(2):427–88. DOI: 10.1103/RevModPhys.77.427

43. Tsunoda N, Otsuka T, Shimizu N, Hjorth-Jensen M, Takayanagi K and Suzuki T. Exotic neutron-rich medium-mass nuclei with realistic nuclear forces. Phys. Rev. C 2017; 95(2):021304. DOI: 10.1103/PhysRevC.95.021304

44. Brown BA and Richter WA. New "USD" Hamiltonians for the *sd* shell. Phys. Rev. C 2006; 74(3):034315. DOI: 10.1103/PhysRevC.74.034315

45. Honma M, Otsuka T, Mizusaki T and Hjorth-Jensen M. New effective interaction for f_5pg_9-shell nuclei. Phys. Rev. C 2009; 80(6):064323. DOI: 10.1103/PhysRevC.80.064323

46. Campo LC, Guttormsen M, Garrote FLB, Eriksen TK, Giacoppo F, Görgen A, Hadynska-Klek K, Klintefjord M, Larsen AC, Renstrøm T, Sahin E, Siem S, Springer A, Tornyi TG and Tveten GM. Test of the generalized Brink-Axel hypothesis in ^{64,65}Ni. Phys. Rev. C 2018; 98(5):054303. DOI: 10.1103/PhysRevC.98.054303

47. Guttormsen M, Larsen AC, Bürger A, Görgen A, Harissopulos S, Kmiecik M, Konstantinopoulos T, Krtička M, Lagoyannis A, Lönnroth T, Mazurek K, Norrby M, Nyhus HT, Perdikakis G, Schiller A, Siem S, Spyrou A, Syed NUH, Toft HK, Tveten GM and Voinov A. Fermi's golden rule applied to the γ decay in the quasicontinuum of ^{46}Ti. Phys. Rev. C 2011; 83(1):014312. DOI: 10.1103/PhysRevC.83.014312

48. Guttormsen M, Larsen AC, Görgen A, Renstrøm T, Siem S, Tornyi T and Tveten GM. Is The Generalized Brink-Axel Hypothesis Valid? PoS 2017; INPC2016:062. DOI: 10.22323/1.281.0062

49. Chandrasekhar S. Stochastic Problems in Physics and Astronomy. Rev. Mod. Phys. 1943; 15(1):1–89. DOI: 10.1103/RevModPhys.15.1

50. Hughes DJ and Harvey JA. Size Distribution of Neutron Widths. Phys. Rev. 1955; 99(3):1032–3. DOI: 10.1103/PhysRev.99.1032

51. Harvey JA, Hughes DJ, Carter RS and Pilcher VE. Spacings and Neutron Widths of Nuclear Energy Levels. Phys. Rev. 1955; 99(1):10–33. DOI: 10.1103/PhysRev.99.10